Current-perpendicular-to-plane Giant Magnetoresistance Devices Using Heusler Alloy Ferromagnetic Layers and New Materials as a Spacer Layer

Ye Du

Doctoral Program in Materials Science and Engineering

Submitted to the Graduate School of

Pure and Applied Sciences

in Partial Fulfillment of the Requirements

for the Degree of Doctor of Philosophy in Engineering

at the

University of Tsukuba

Table of Contents

Chapter 1   Introduction

1.1 Preface: The emergence of spintronics for data storage

Electrons possess a charge and a spin, but for long they have been considered separately until recent years in view of digital data storage and transport. In conventional electronics, electric fields have been used to move charges to convey information and capacitors have been the containers to store them. In traditional magnetic recording, the read-write process is controlled through the utilization of external magnetic field, which acts on the local spins in the ferromagnets. In 1988, with the discovery of giant magnetoresistance (GMR) effect,[1,2] a transcendent paradigm of charge control was proposed through the manipulation of magnetizations. Specifically, the electrical resistance of the ferromagnetic/non-magnetic (FM/NM) multilayer changes with respect to the magnetization configurations (e.g. parallel or antiparallel) of the neighboring FM layers. The magnetizations and the charge currents were demonstrated to interplay with each other through the electron spins, thereby boosting a new field which is called spintronics.[3,4]

Practically, the so-called spin valve sensor,[5] which consists mainly of a $FM_1/NM/FM_2$ tri-layer, was invented in 1991 that finds application in the hard disk drive (HDD) read head and overall brings about 2-3 orders of increase in the HDD recording density up to approximately 1 Gbit/in^2.[4] In modern data storage spintronics, another scientific advancement which is as important as the GMR effect would be the enhancement of the tunneling magnetoresistance (TMR) at room temperature. A TMR sensor has very similar structure as that of a spin valve, with the major difference that its NM layer is a thin insulating layer rather than a metallic layer as for the spin valve. For the present time, the TMR based magnetic tunnel junctions (MTJs) are being used as HDD read heads and the areal recording density is approaching 1 Tbit/in^2. However, for further enhancement of the HDD areal density, the MTJs will be having problems in high speed read out due to its unfavorable large junction resistance. An alternative way to tackle with it is to revisit the GMR effect with the current-perpendicular-to-plane (CPP) geometry.[6] Low device resistance as well as moderate MR output has made the CPP-GMR a promising choice for the next generation read head sensors.

This doctoral thesis will focus on the utilization of highly spin polarized Heusler alloy and various spacer materials to 1) obtain large MR output in the CPP-GMR sensors, 2) investigate the crystal orientation dependence of MR output in CPP-GMR sensor, 3) obtain large voltage output in CPP-MR sensors with high-resistive spacer materials by taking advantage of the current-confined-path geometry.

1.2   The discovery of GMR and its technological implication

In the year of 1988, the giant magnetoresistance (GMR) effect was discovered by Albert Fert and his co-workers, and independently by Peter Grünberg and his co-workers.[1,2] Both of them fabricated several sets of epitaxial Fe/Cr multilayer stacks and measured their electrical resistance with varying external magnetic fields. **Fig. 1-1** shows (a) the hysteresis loops and (b) the R-H curves of Fe/Cr multilayers with different Cr thickness. In the absence of external magnetic field,
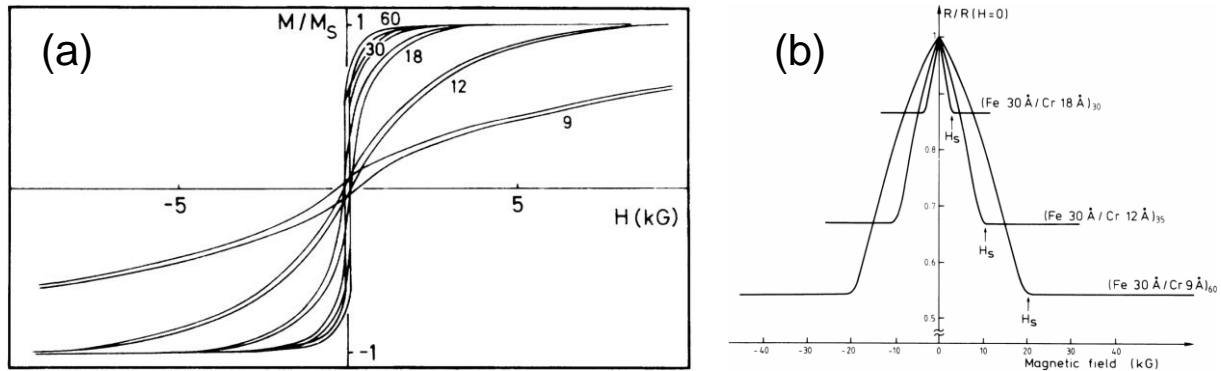
Fig. 1-1 The discovery of giant magnetoresistance with (a) In-plane hysteresis loop of Fe/Cr multilayers at 4.2 K and (b) In-plane multilayer resistance with varying magnetic field. Courtesy of Baibichi *et al.*[1]

the neighboring Fe layers exhibit antiparallel magnetizations because of the antiferromagnetic interlayer exchange coupling (IEC) that occurs through the Cr spacer. With the presence of external field, the magnetizations of Fe start to rotate towards the field direction and finally saturate at certain saturation magnetic field H_s. In the Fe magnetization rotation process, a change of the in-plane thin film resistance was observed that comes from different scattering rate of spin-up and spin-down electrons for the parallel and antiparallel magnetization configurations, respectively. The optimistic GMR ratio is defined as $(R_{ap} - R_p) / R_p \times 100\%$, where the R_{ap} and R_p represent the resistance of the film stack with antiparallel and parallel Fe magnetization configurations. In the report by A. Fert group, the GMR ratio is as large as 82% at 4.2 K with Cr thickness of 9 Å, and the value is lowered by about a factor of 2 at room temperature. Note that for the GMR effect mentioned here, the current direction is in the plane of the multilayer thin film, and we call it current-in-plane (CIP) GMR effect.
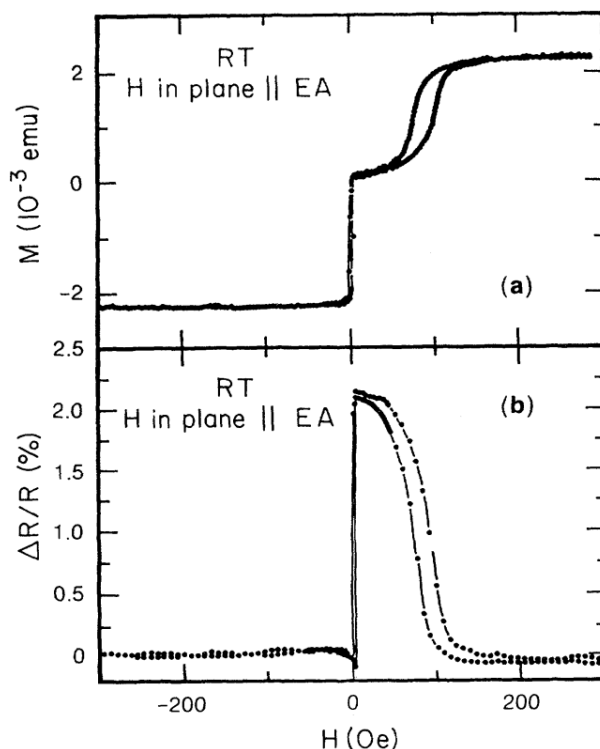
Fig. 1-2 (a) Magnetization curve and (b) R-H curve of an exchange biased spin-valve by Dieny *et al.*[6]

The discovery of GMR has triggered numerous researches such as the oscillatory interlayer exchange coupling[7] and the granular GMR effect *et al.*,[8] but the most pivital outcome that the GMR has sparked off is the invention of spin valve sensors[5] in 1991, which were later used as magnetoresistive hard disk drive (HDD) read heads and brought about a revolutional increase in the areal density for magnetic data storage.[4] **Fig. 1-2** shows the magnetization and and R-H curve of an exchange biased spin-valves reported by Dieny *et al.*[5] The principle of its manipulation of the charge current by altering the magnetization direction is very similar to the original GMR effect, one major difference is that the switching field required is much smaller (e.g. several tens oersted) for the nominal $FM_1/NM/FM_2$ tri-layer structure owing to the usage of relatively thick NM layer that substantially weakens the interlayer exchange coupling between the two FM layers. Also, one of the FM layers (e.g. FM_1) has its magnetization fixed (or pinned) by an adjacent antiferromagnetic layer through exchange magnetic anisotropy. In 1997, IBM first commercialized the GMR spin valve sensor in HDDs to replace the AMR sensor and the storage density grew by 100% each year for about 6 years. The huge impact that the GMR effect exerts on the magnetic data storage enables its discoverers to share the Nobel prize in physics two decades later.

Thereafter, the CIP-GMR read head was replaced by tunneling magnetoresistance (TMR) sensors using an insulating NM layer of Al-O or MgO yielding larger MR output. The recording density for the time being is approaching 1 Tbit/in^2. Recent years, the GMR effect started to draw

attention again. With the advancement of nano-pattern and film deposition technique, nano-scale GMR devices with current-perpendicular-to-plane (CPP) geometry have much larger MR output and smaller physical dimension compared to the CIP-GMR head. The low-resistive CPP-GMR read sensors are considered to be suitable for recording density over 1 Tbit/in^2.

1.3　GMR with current-perpendicular-to-plane geometry: the CPP-GMR

1.3.1　The advantage of CPP over CIP

Following the discovery of CIP-GMR in 1988, the current-perpendicular-to-plane giant magnetoresistance (CPP-GMR) effect, where the current flows perpendicularly to the thin film plane, was observed in 1991 by Pratt *et al.*[9] at low temperature. They found that at 4.2 K, the CPP-GMR can be 10 times larger than CIP-GMR for the same thin film samples. In 1993, by fabricating CPP-GMR nano-pillars using optical lithography and reactive ion etching techniques, Gijs *et al.*[10] reported similar tendency at temperatures ranging from 4.2 K to 300 K (shown in **Fig. 1-3**). The
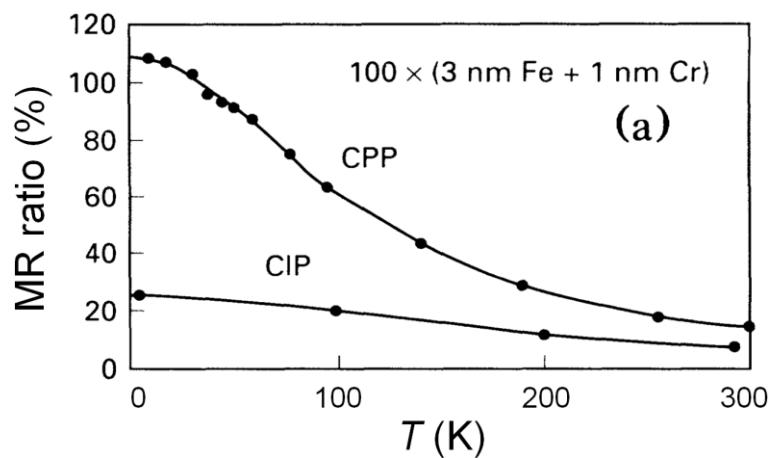
Fig. 1-3 Temperature dependence of CIP- and CPP- GM ratio for Fe/Cr multilayers by Gijs *et al.*[10]

CIP- and CPP- discrepancy can be explained as follows. The characteristic length for the transport in CIP multilayers is the mean free path λ, thus the CIP-GMR effect becomes marginal when the NM layer thickness is much longer than λ because the current then does not go through both FM/NM layers. Even if NM layer thickness is small, we have to consider the current distribution in the FM/NM multilayers. On the other hand for CPP-GMR case (especially when fabricated into micro- or nano- pillars), the current goes homogeneously and vertically through the multilayer and the characteristic length is the spin diffusion length l_s, which is much longer than λ. Thus the spin-dependent scattering can be more efficiently utilized for the CPP-GMR compared to the CIP-GMR, giving rise to a larger output for the former.

1.3.2 Pseudo spin-valves

With the development of nano-patterning techniques, the lateral dimension of CPP-GMR devices goes down to the range of submicron or nanoscale. To simplify the model for the investigation of spin-dependent scattering in multilayers, a pseudo spin-valve (PSV) structure, free from the antiferromagnetic pinning layer, was realized in modern CPP-GMR nano-pillars. A schematic demonstration of the PSV tri-layer structure in parallel and antiparallel states is shown in **Fig. 1-4**. Very similar to the exchange biased spin valve, a PSV has two thin ferromagnetic (FM)
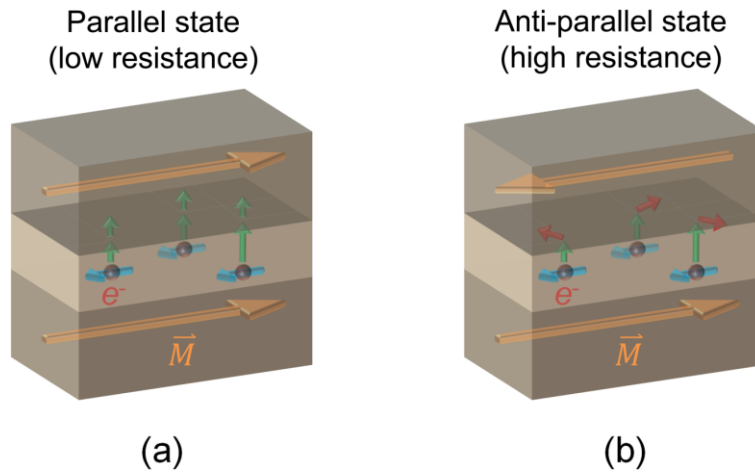
Fig. 1-4 Schematic demonstration of a nanoscale pseudo spin-valve structure with two thin ferromagnetic (FM) layers (dark grey) sandwiched by a metallic non-magnetic (NM) spacer layer (light grey). The electron flows vertically from bottom to top.

layers (dark grey) sandwiched by a metallic non-magnetic (NM) spacer layer (light grey), in which the electrical current flows perpendicularly to the film plane from upper FM layer to the lower one, thus the electrons transport vertically from bottom to top. We assume here that the FM layer thickness is much larger than its spin diffusion length while the NM layer thickness is much smaller than its spin diffusion length but thick enough (e.g. 5 nm) to eliminate strong interlayer exchange coupling between the two FM layers. With the presence of external magnetic field that saturates the tri-layer, the magnetizations of two FM layers are parallel as shown in **Fig. 1-4 (a)**. The electrons become spin-polarized after going through the bottom FM layer with majority spins pointing to the left, and will be hardly scattered when going through the upper FM layer because the spin direction of the transport electrons is the same as the local spins in the top FM layer. Thus, the parallel state shows low resistance (R_P). On the other hand, without an external magnetic field, the submicron-sized PSV pillar exhibits antiparallel configuration for the FM layer magnetizations due to the anti-ferromagnetic magneto-static coupling induced by side wall stray fields. For the antiparallel state in **Fig. 1-4 (b)**, the spin polarized electrons going through the upper layer will be strongly scattered

through the occurrence of spin diffusion induced spin accumulation effect because the spin direction of the transport electrons is opposite to the local spins in the top FM layer. In this case, the antiparallel state shows higher resistance (R_{AP}). With this simple device structure, spin-dependent scattering can be examined by theoretical mode such as the Valet-Fert fitting *et al.*[11]

1.4   Mechanism of GMR

1.4.1   Spin-dependent transport in 3d ferromagnetic materials

Before going further to explain the mechanism of GMR that exists in multilayer stacks, here we take a look at the spin-dependent transport in 3d ferromagnets based on Mott's two-current model.[12] For example, we show the density of states for nickel in **Fig. 1-5**. Both the s band (4s) and d band (3d) contribute to the density of states near the Fermi level (E_F). The s electrons, which have high mobility, carry most of the current by resembling free electrons. The d electrons, however, are
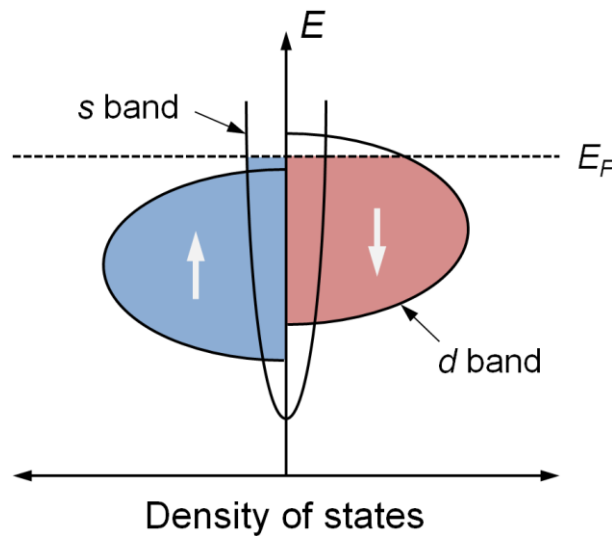
Fig. 1-5 Schematic density of states for 3d ferromagnet nickel.

weak current carriers because of their high effective mass and low mobility. Due to the exchange interaction that favors parallel configuration of electron spins (the Pauli principles), the 3d spin-up and spin-down states are shifted in energy. The majority spin channel (spin-up state) is primarily consisted of s electrons while the minority spin channel (spin-down state) is mainly consisted of d electrons. As a result, the spin-up states in nickel are s-like and weakly scattered, but the spin-down states are strongly scattered due to the presence of large density of d states at the Fermi level into which the free electron can scatter. In another word, the majority spin or the up spin channel in nickel has smaller resistivity compared to the minority spin or the down spin channel. The spin polarization of the electrical current can be defined as $\beta = (\rho_\downarrow - \rho_\uparrow)/(\rho_\downarrow + \rho_\uparrow)$, in which $\rho_\downarrow$ and $\rho_\uparrow$ are the resistivity of the up and down spin electrons. This value can also be interpreted as the local "bulk spin scattering asymmetry" in 3d metals or alloys.

1.4.2 Mechanism of CIP-GMR

The current-in-plane giant magnetoresistance effect (CIP-GMR) can be interpreted in terms of Mott's two-current theoretical model[12] for conduction (spin-flip scattering is neglected for simplicity). The spin-up and spin-down electron channels are in parallel connections and the scattering turns out to be different for the parallel and antiparallel configurations of FM layer magnetizations in the $(FM/NM)_n$ multilayers. Technically, the spin-dependent scattering occurs both in the bulk of the FM layer and at the FM/NM interfaces. If we consider the bulk only, when the multilayer is in parallel magnetization state, the resistivity for the two spin channels are $\rho_\uparrow$ and $\rho_\downarrow$, respectively. Therefore the overall multilayer resistivity is given by $\rho_P = (1/\rho_\uparrow + 1/\rho_\downarrow)^{-1} = \rho_\uparrow \rho_\downarrow / (\rho_\uparrow + \rho_\downarrow)$, where the $\rho_\uparrow$ and $\rho_\downarrow$ represent the resistivity of the spin-up and spin-down electrons. For the antiparallel case, however, for both spin channels the spin-up and spin-down electrons undergo strong scattering with their resistivity averaged as $(\rho_\uparrow + \rho_\downarrow)/2$, therefore the overall multilayer resistivity is given by $\rho_{AP} = (\rho_\uparrow + \rho_\downarrow)/4$, the optimistic GMR is defined as

$$\frac{\Delta\rho}{\rho_P} = \frac{\rho_{AP} - \rho_P}{\rho_P} = \frac{(\rho_\uparrow - \rho_\downarrow)^2}{4\rho_\uparrow\rho_\downarrow} \tag{1.1}$$

note that the GMR effect coming from the FM/NM interfaces can be derived similarly. As a matter of fact, the interfacial scattering is usually dominant in such artificial hetero-structures, as demonstrated by Parkin *et al.*[13]

1.4.3 Mechanism of CPP-GMR

Here we briefly review the mechanism of CPP-MR using the macroscopic model proposed by Valet and Fert,[11] in which the transport current is closely related to the electrochemical potentials involving transport coefficients of resistivity (conductivity) and spin diffusion length. To start, we define $\rho_\uparrow$ and $\rho_\downarrow$ as the resistivity of the spin-up and spin-down electrons, $R_{F/N}{}^\uparrow A$ and $R_{F/N}{}^\downarrow A$ as the interfacial resistance-area product of spin-up and spin-down electrons. According to the two-current model, the total resistivity coming from the bulk part of the CPP-MR multilayer is written as

$$\rho = \left(\frac{1}{\rho_\uparrow} + \frac{1}{\rho_\downarrow}\right)^{-1} = \frac{\rho_\uparrow \rho_\downarrow}{\rho_\uparrow + \rho_\downarrow} \tag{1.2}$$

similarly, the total interfacial resistance-area product is

$$R_{F/N}A = \frac{R_{F/N}{}^\downarrow A \cdot R_{F/N}{}^\uparrow A}{R_{F/N}{}^\downarrow A + R_{F/N}{}^\uparrow A} \tag{1.3}$$

From the definition of bulk and interfacial spin polarization (β and γ),

$$\beta = \frac{\rho_\downarrow - \rho_\uparrow}{\rho_\downarrow + \rho_\uparrow} \tag{1.4}$$

$$\gamma = \frac{R_{F/N}{}^\downarrow A - R_{F/N}{}^\uparrow A}{R_{F/N}{}^\downarrow A + R_{F/N}{}^\uparrow A} \tag{1.5}$$

For simplicity, we introduce expanded resistivity ρ^* and interfacial resistance-area product $R_{F/N}A^*$,

$$\rho^* = \rho/(1 - \beta^2) \tag{1.6}$$

$$R_{F/N}A^* = R_{F/N}A/(1 - \gamma^2) \tag{1.7}$$

From (1.2) (1.4) and (1.6), the $\rho_{\uparrow(\downarrow)}$ is derived as

$$\rho_{\uparrow(\downarrow)} = 2\rho^*[1 - (+)\beta] \tag{1.8}$$

From (1.3) (1.5) and (1.7), the $R_{F/N}{}^{\uparrow(\downarrow)}A$ is

$$R_{F/N}{}^{\uparrow(\downarrow)}A = 2R_{F/N}A^*[1 - (+)\gamma] \tag{1.9}$$

Using the two-current model, we obtain the general expression of resistance (RA) array of the spin-up and spin-down channels in parallel and antiparallel state shown in **Fig. 1-6**, in which the $t_{F(N)}$ represents the thickness of the FM (NM) layer and the $\rho_{F(N)}$ is their respective resistivity (note that $\rho_N{}^* = \rho_N$ because $\beta = 0$ for NM materials). The bulk and interfacial contribution to the total resistance have been separately obtained based on the relation of $R = (\rho \cdot l)/A$. As a result, the resistance-area product for the parallel and antiparallel state is expressed as:

$$RA_P = \frac{\begin{aligned}&\left[\left(2R_{F/N}A^* + 2\rho_F{}^*t_F + \rho_N{}^*t_N\right) - 2\left(R_{F/N}A^* \cdot \gamma + \rho_F{}^*t_F\beta\right)\right] \cdot\\&\left[\left(2R_{F/N}A^* + 2\rho_F{}^*t_F + \rho_N{}^*t_N\right) + 2\left(R_{F/N}A^* \cdot \gamma + \rho_F{}^*t_F\beta\right)\right]\end{aligned}}{2R_{F/N}A^* + 2\rho_F{}^*t_F + \rho_N{}^*t_N} \tag{1.10}$$

$$RA_{AP} = 2R_{F/N}A^* + 2\rho_F{}^*t_F + \rho_N{}^*t_N \tag{1.11}$$

Therefore

$$\Delta RA = RA_{AP} - RA_P = \frac{4\left(R_{F/N}A^* \cdot \gamma + \rho_F{}^*t_F\beta\right)^2}{2R_{F/N}A^* + 2\rho_F{}^*t_F + \rho_N{}^*t_N} \tag{1.12}$$

By assuming $\rho_N{}^*t_N \ll \rho_F{}^*t_F$, ΔRA is roughly given as

$$\Delta RA \sim 2\beta^2\rho_F{}^*t_F + 2\gamma^2 R_{F/N}A^*$$
$$= 2\frac{\beta^2}{1-\beta^2}\rho_F t_F + 2\frac{\gamma^2}{1-\gamma^2}R_{F/N}A \tag{1.13}$$

From (1.13) we notice that the enhancement of ΔRA can be achieved not only by increasing the bulk spin polarization in FM layer and interfacial spin polarization at FM/NM interface, but also by increasing the resistivity of FM layer and the FM/NM interfacial resistance. However, the above derivation is valid only on the assumption that the thickness of the FM and NM layers is much smaller than their respective spin diffusion length. For the most general case, Valet and Fert finally derived the total resistivity-area product for a multilayer consisted of M bilayers by introducing boundary conditions as well as true discontinuities of interfacial potentials,

$$RA^{P,AP} = M\left(RA_0 + 2RA_{SI}^{P,AP}\right)$$
$$\text{with } RA_0 = (1-\beta^2)\rho_F{}^*t_F + 2(1-\gamma^2)R_{F/N}A^* + \rho_N{}^*t_N \tag{1.14}$$

in which the spin-coupled interface RA ($RA_{SI}^{P,AP}$) is given by

RA_{SI}^P

$$= \frac{\frac{(\beta-\gamma)^2}{\rho_N{}^*l_{sf}^N}\coth\left(\frac{t_N}{2l_{sf}^N}\right) + \frac{\gamma^2}{\rho_F{}^*l_{sf}^F}\coth\left(\frac{t_F}{2l_{sf}^F}\right) + \frac{\beta^2}{R_{F/N}A^*}}{\frac{1}{\rho_N{}^*l_{sf}^N}\coth\left(\frac{t_N}{2l_{sf}^N}\right)\frac{1}{\rho_F{}^*l_{sf}^F}\coth\left(\frac{t_F}{2l_{sf}^F}\right) + \frac{1}{R_{F/N}A^*}\left[\frac{1}{\rho_N{}^*l_{sf}^N}\coth\left(\frac{t_N}{2l_{sf}^N}\right) + \frac{1}{\rho_F{}^*l_{sf}^F}\coth\left(\frac{t_F}{2l_{sf}^F}\right)\right]} \tag{1.15}$$

and

RA_{SI}^{AP}

$$= \frac{\frac{(\beta-\gamma)^2}{\rho_N{}^*l_{sf}^N}\tanh\left(\frac{t_N}{2l_{sf}^N}\right) + \frac{\gamma^2}{\rho_F{}^*l_{sf}^F}\coth\left(\frac{t_F}{2l_{sf}^F}\right) + \frac{\beta^2}{R_{F/N}A^*}}{\frac{1}{\rho_N{}^*l_{sf}^N}\tanh\left(\frac{t_N}{2l_{sf}^N}\right)\frac{1}{\rho_F{}^*l_{sf}^F}\coth\left(\frac{t_F}{2l_{sf}^F}\right) + \frac{1}{R_{F/N}A^*}\left[\frac{1}{\rho_N{}^*l_{sf}^N}\tanh\left(\frac{t_N}{2l_{sf}^N}\right) + \frac{1}{\rho_F{}^*l_{sf}^F}\coth\left(\frac{t_F}{2l_{sf}^F}\right)\right]} \tag{1.16}$$

with the very general term for the ΔRA of

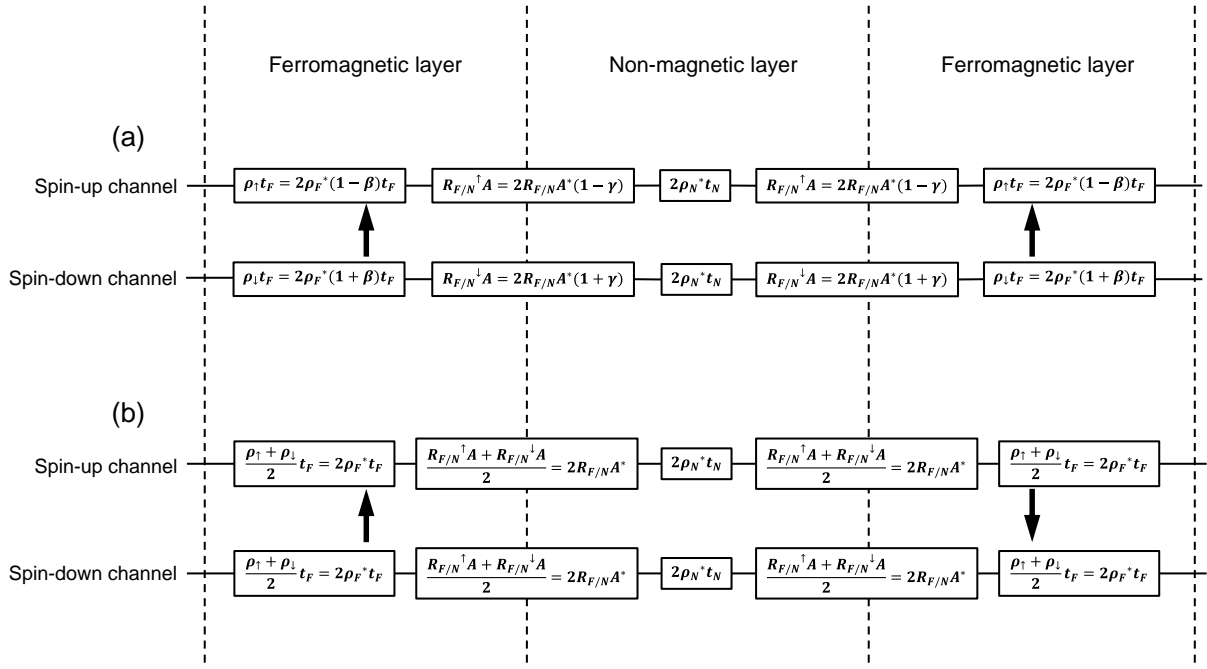$$\Delta RA = 2M(RA_{SI}^{AP} - RA_{SI}^P) \tag{1.17}$$

11

Fig. 1-6 General expression of resistance array of the spin-up and spin-down channels in (a) parallel and (b) antiparallel state.

1.5 Applications of CPP-GMR

1.5.1 Read sensor for magnetic recording

The digital information (0 or 1) in HDDs is recorded as magnetic domains on magnetic recording medium, which comprise of hard magnetic particles surrounded by NM materials as isolation matrix. The read head is nanometers above the recording medium, which rotates at a speed of normally thousands rpm. Thus the read head senses the stray fields coming from magnetic domains on the medium and outputs voltage. **Fig. 1-8** schematically describes the reading process. Generally, three main factors feature the performance of the read head: the resolution, the signal-to-noise ratio (SNR), and the high frequency response. Specifically, the resolution of the read head is limited by the physical size of the read head. The SNR is primarily determined by the MR output voltage $\Delta V = \Delta RA \times J_c = MR\ ratio \times V_{bias}$, in which ΔRA refers to the resistance change-area product of the MR device, J_c refers to the current density and V_{bias} refers to the bias voltage applied to the read sensor. As for the high frequency property, it is determined by the sensor resistance and capacitance which are closely related to its high speed readout. In summary, in order to realize ultrahigh density magnetic recording above 1 Tbit/in^2, a read sensor with nanoscale physical size (e.g. tens of nanometer), large room temperature MR output (e.g. tens of percent), and a moderately small devices RA (e.g. 0.1-0.2 Ω μm^2) is essentially required.

For quantitative estimation of the required sensor output, Takagishi *et al.*[14] carried out numerical simulations of MR ratio vs. *RA* for read head suitable for the recording density of 2 Tbit/in^2 as shown in **Fig. 1-9**. Generally a large MR ratio with a moderate *RA* is desirable. For the critical current density of 1×10^8 A/cm^2, the minimum required MR ratio is approximately 20% at the *RA* value of 0.1 Ω μm^2. Currently, as the MgO-based MTJs[15] are being utilized in read sensors of HDDs with the areal density close to 1 Tbit/in^2, there is an ever-increasing demand for the decrease of *RA* to achieve high-speed readout for higher density recording. Moderately decreasing the MgO barrier thickness reduced the *RA* to below 1 Ω μm^2,[16] and a state-of-the-art MTJ used in HDDs yields a *RA* of 0.5 Ω μm^2 with TMR ratio of around 100%.[17] However, further decreasing the MgO thickness causes problems such as the current leakage in MTJs that seriously degrades the MR ratio and junction reliability. Therefore, it becomes exceptionally difficult for MTJs to go near or beyond 2 Tbit/in^2. On the other hand, achieving low *RA* is readily easy for all-metallic CPP-GMR devices. For instance, Childress *et al.*[18] showed the potential of a polycrystalline CPP-GMR read head with the *RA* of 0.06 Ω μm^2 to be used for areal density of 300 Gbit/in^2. In spite of this, the low MR ratio of less than 10% in CPP-GMR becomes a problem when using conventional 3d materials as the FM electrodes, because large MR ratio (or intrinsically, large ΔRA) is one of the

most critical parameters to achieve desirable SNR and subsequently potential ultrahigh areal density. Based on Takagishi's result (**Fig. 1-9**), assuming a *RA* of 60 mΩ μm^2, one needs to obtain CPP-GMR ratio of (roughly) 25% or Δ*RA* of 15 Ω μm^2 to potentially realize the areal density of 2 Tbit/in^2.

Except for a large MR ratio, the reduction of the total CPP-GMR thin film thickness is also essential. The state-of-the-art read head uses an exchange biased spin-valve that has a synthetic antiferromagnetic structure as the pinning layer. The total thickness of those layers is ~10 nm, thus the active part of the CPP-GMR read head (FM/NM/FM tri-layer) needs to go below 10 nm for 2 Tbit/in^2 recording based on Takagishi's simulation result that the resolution of the read head is ~20 nm for such recording density.

Last but not least, the spin torque induced magnetization instability is another critical issue one has to tackle.[19] For a current density of 1×10^8 A/cm^2 that was used in Takagishi's paper,[14] the spin angular momentum of the spin polarized conduction electrons in the CPP-GMR junctions becomes so large that the torque it exerts on the magnetization of the reference FM layer is strong enough to alter or even reverse its direction. Such a phenomenon is called spin transfer torque (STT) magnetization switching. Practically, with the onset of the STT effect, the MR is decreased and the linear response of the read head is destroyed. The critical current density that describes the onset of the STT effect is determined by the so-called damping torque given in the Landau-Lifshitz-Gilbert equation. On one hand, FM layers with moderately increased damping constant would be preferable. On the other hand, the STT effect can be potentially suppressed by properly choosing the NM layer.
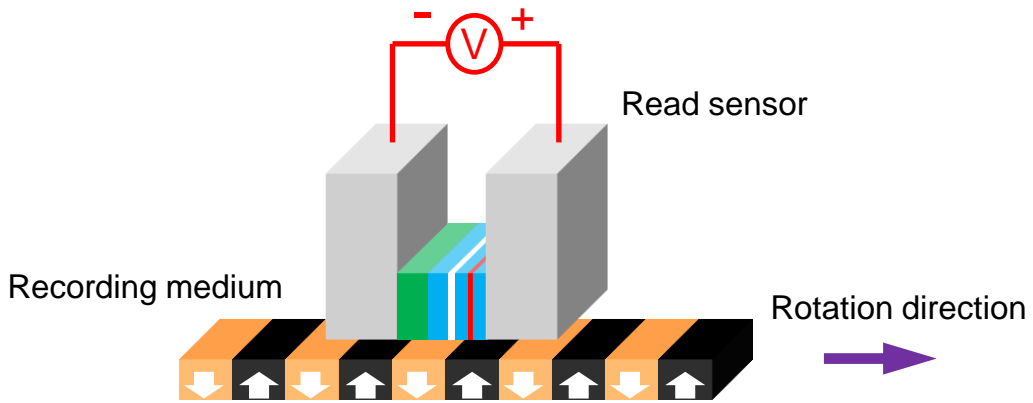
Fig. 1-8 HDD read head and recording medium.
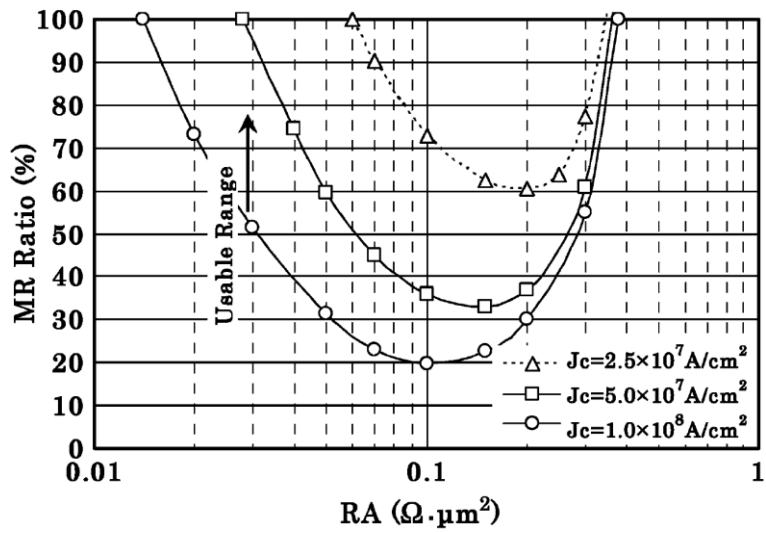

Fig. 1-9 Simulation of requirement of RA and MR ratio for 2 Tbit/in2 read head with different critical current densities. Courtesy of Takagishi *et al.*[14]

1.5.2 Spin torque oscillators for microwave assisted magnetic recording

The spin torque oscillator was first demonstrated by Kiselev *et al.*[20] in 2003 using a tri-layer Co/Cu/Co tri-layer. With the presence of d.c. current, the spin transfer torque coming from one FM layer produces several types of magnetic precession modes in the other FM layer. The precession frequency is given as $\frac{\gamma}{2\pi} H_{eff}$ by the Landau-Liftshitz-Gilbert (LLG) in which γ is the gyromagnetic ratio and H_{eff} is the effective magnetic field. From their simulation based on the LLG equation for a single-domain nano-magnet, they suggested the occurrence of large-angle, in-plane like precession of the free layer magnetization when large-amplitude microwave signals are observed (**Fig. 1-10**).
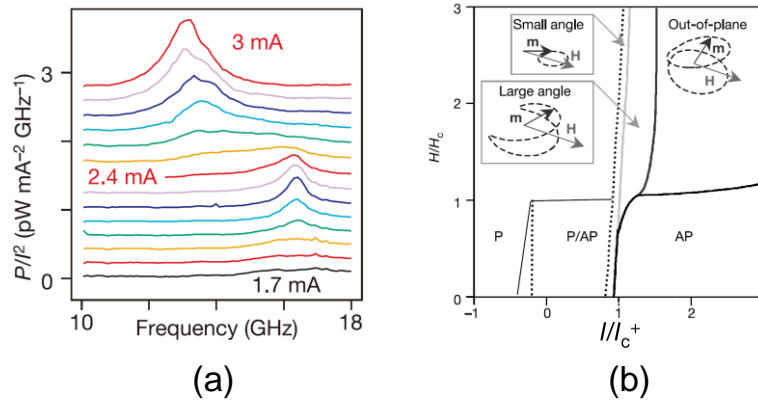

Fig. 1-10 (a) Transition from small-amplitude precession to large-amplitude precession with increasing current magnitude (b) Phase diagram of oscillation mode for current and external field. Courtesy of Kiselev *et al.*[20]

Practically, in order to utilize the microwave signals produced from the STO, the magnetic moment of the FM layer and the oscillation mode are critical factors that determine the signal amplitude as shown in **Fig. 1-10** (b). For example, obtaining the oscillation with a large current and large external magnetic field is needed to acquire the out-of-plane mode for the MAMR application[21] which was proposed by Zhu *et al* in 2008. Specifically, when the microwave signal generated from the STO matches the FM resonance frequency of the recording media, its magnetization starts to resonate and the media coercivity decreases, then it becomes easy to switch the recording bit for information-writing process.

1.6 Co-based full Heusler alloy

1.6.1 Half-metallic ferromagnets

A new class of materials, the so-called half-metals, was discovered by de Groot and his collaborators in 1983.[22] They conducted band structure calculations for the Mn-based Heusler alloy NiMnSb with the $C1_b$ structure. Strikingly, they found that for the majority-spin band some density of states appears crossing the Fermi level while for the minority-spin band, no density of states was found at the Fermi level (**Fig. 1-11**). This suggests that electrons with only one spin direction can go through NiMnSb, making it potentially a perfect spin filter or spin polarizer. Such materials with one spin band being metallic and the other being semiconducting are thereafter called *half-metals*. Up to now, the following materials have been predicted to be half-metals: (1) half or full Heusler alloys (2) Perovskite or double Perovskite oxides (3) some oxides materials such as CrO_2, Fe_3O_4, $Co_{1-x}Fe_xS_2$ *et al.* (actually only CrO_2 has been widely accepted as a real half-metal).

For the materials mentioned above, the half-metallicity of CrO_2, $Co_{1-x}Fe_xS_2$, $La_{0.7}Sr_{0.3}MnO_3$ (Perovskite oxide) and Co_2MnSi (full Heusler alloy) has been experimentally investigated at low temperature. However, the Curie temperature for oxide half-metals is rather low (e.g. 370 K for $La_{0.7}Sr_{0.3}MnO_3$ and 398 K for CrO_2), their magnetic properties and therefore bulk spin polarization drastically deteriorate at room temperature. Nonetheless, half and full Heusler alloys have comparatively high Curie temperature (e.g. 730 K for NiMnSb and 980 K for Co_2MnSi), therefore from a practical point of view they attract more attentions due to their potential presence of half-metallicity even at room temperature. Particularly, the full Heusler alloys with a $L2_1$ ordered structure do not possess vacant sites which the half Heusler alloys usually have.

Practically, the half-metal (especially the full Heusler alloys) is expected to be an ideal spin polarizer to realize a large giant or tunneling magnetoresistance, a low current density for the current induced magnetization switching.
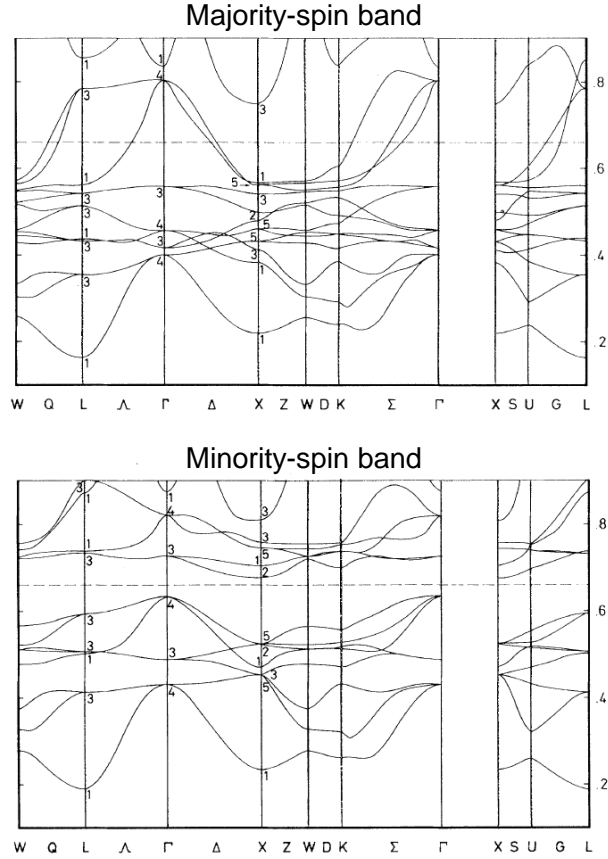
Fig. 1-11 Majority and minority band structure calculation for half Heusler alloy NiMnSb. Courtesy of de Groot *et al.*[22]

1.6.2 Crystal structure of the full Heusler alloy

Back in 1903, a ferromagnetic Cu_2MnAl alloy despite its nonmagnetic elemental constituents was reported by Friedrich Heusler from Germany. The alloy which was later named Heusler alloy has a $L2_1$ ordered structure with a general X_2YZ composition, in which the X and Y are transition metals and Z is a main group element. The $L2_1$ structure is consisted of four fcc sublattices as shown in **Fig. 1-12**. For the four sets of atomic elements, they have the equivalent atomic positions of X1 (0 0 0), X2 (1/2 1/2 1/2), Y (1/4 1/4 1/4), Z (3/4 3/4 3/4). The structure factors are as following,

$L2_1$ structure (h, k, l odd) $\qquad\qquad\qquad\qquad\qquad F_{L2_1} = |4(f_X - f_Y)|$
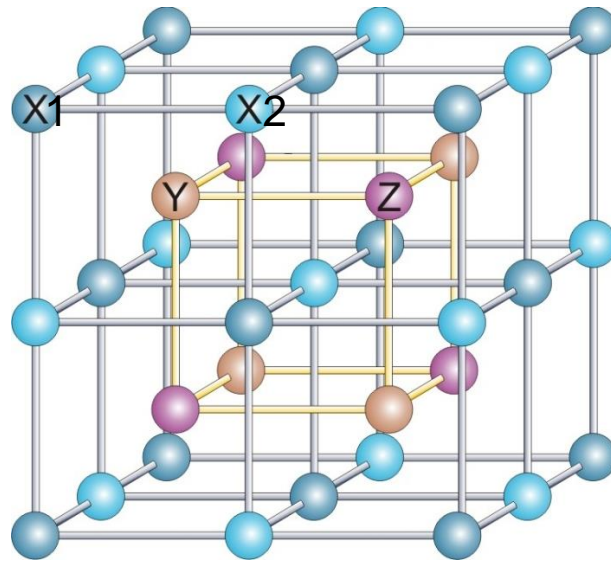
B2 structure (h, k, l even and $h + k + l = 4n + 2$) $\qquad F_{B2} = |4(2f_X - f_Y - f_Z)|$

Fundamental (h, k, l even and $h + k + l = 4n$) $\qquad F_{funda} = |4(2f_X + f_Y + f_Z)|$

18

L2$_1$ structure, Group # 225
Fm$\bar{3}$m, cF16

Fig. 1-12 Crystal structure of L2$_1$ full Heusler alloy.

in which f is the atomic scattering factor and n being an integer. The L2$_1$ diffraction disappears by mixing elements Y and Z, and the B2 diffraction disappears by mixing all the elements.

1.6.3 Thermodynamics

Full Heusler alloys generally have order-disorder transformations above the Curie temperature but below the melting temperature. For instance, Webster[23] studied the chemical ordering of the Co$_2$MnAl Heusler alloy using a high temperature x-ray diffractometer. **Fig. 1-13** shows the 111 L2$_1$ and 200 B2 diffraction intensity of the Co$_2$MnAl alloy as a function of temperature. The L2$_1$ peak disappears at around 1000 K, indicating the L2$_1$-B2 transformation. On the other hand, the B2-A2 transformation appears at 1250 K. A more recent report is shown in **Fig. 1-14**, Varaprasad *et al.*[24] studied the order-disorder transformation for the Co$_2$Fe(Ga$_x$Ge$_{1-x}$) full Heusler alloys with x=0, 0.5 and 1 using differential thermal analysis (DTA). For all the Heusler alloys the Curie temperature appears between 1000 K and 1100 K. For the alloys of Co$_2$Fe(Ga$_{0.5}$Ge$_{0.5}$) and Co$_2$FeGa, the L2$_1$-B2 transformation is observed above the Curie temperature. For Co$_2$FeGe alloy, the L2$_1$-B2 disordering process is not observed even up to its melting temperature. These results suggest that the Co-Fe-Ga-Ge Heusler alloy system is robust against thermal annealing.
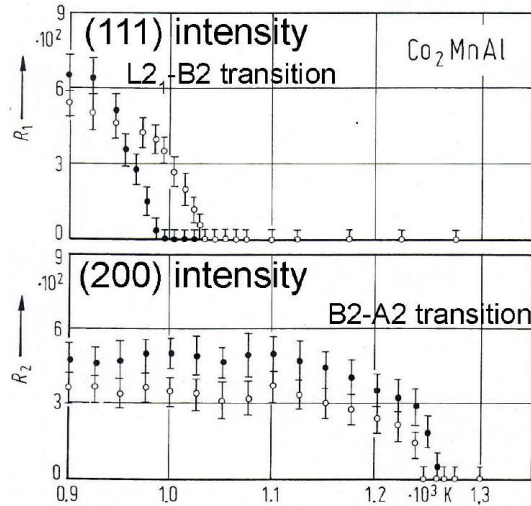
Fig. 1-13 Temperature dependence of (111) $L2_1$ and (200) B2 diffraction intensity for Cu_2MnAl. Courtesy of Webster.

The as-deposited thin films fabricated by techniques such as magnetron sputtering usually exhibit disordered A2 or partially B2 structure, therefore thermal annealing is critical to achieve better chemical ordering in Heusler thin films. For the Co_2Mn-based Heusler alloys, they have low $L2_1$ ordering temperature (e.g. ~350°C for Co_2MnSi[25]) but Mn is prone to diffuse easily upon annealing. For the Co_2Fe-based Heusler alloys, they have very high Curie temperature which suggests desirable endurance against thermal annealing, but the requirement of high temperature annealing to acquire $L2_1$ ordering may cause problems for practical application.
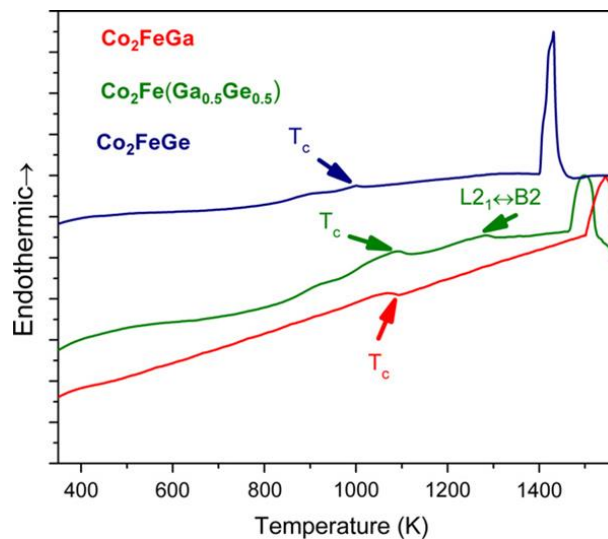

Fig. 1-14 DTA curves of $Co_2Fe(Ga_xGe_{1-x})$ (x=0, 0.5 and 1) bulk alloys. Courtesy of Varaprasad *et al.*[24]

1.6.4 Electronic properties

Picozzi *et al.*[26] have carried out *ab initio* study for the structural, electronic and magnetic properties of Co_2MnX (X = Si, Ge, Sn). They found out that the as the X atomic number decreases, there is an increase of the energy gap and spin gap. As a result, the Co_2MnSi and Co_2MnGe turn out to be half-metals, while Co_2MnSn is nearly half-metallic because some density of states was found to cross the Fermi level (**Fig. 1-15**).
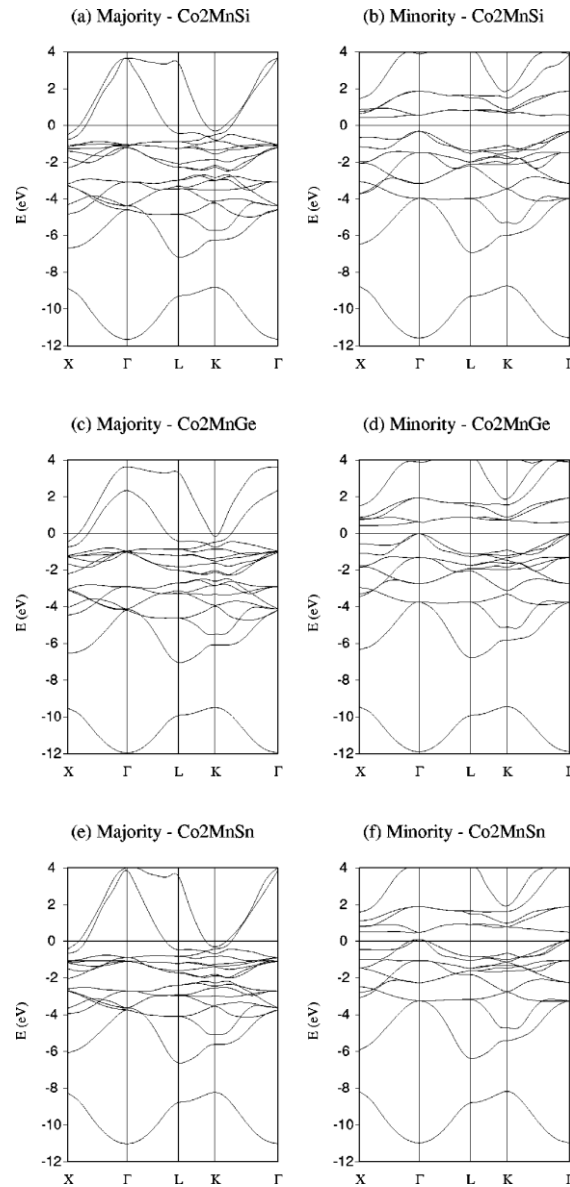

Fig. 1-15 Majority and minority band structure for Co_2MnX (X = Si, Ge, Sn). From Ref. [26]

As for the total spin magnetic moments (M_t) in the full Heusler alloy Co_2MnZ (may apply to other Heusler compounds), Galanakis et al.[27] have found a simple relation (**Fig. 1-16** (a)) of

$$M_t = Z_t - 24 \qquad (1.18)$$

where Z_t represents the total number of valence electrons in the Heusler alloy. The origin of (1.18) is the well-known Slater-Paulin behavior, in which the occupancy of the spin-down bands does not change while the extra or missing electrons contribute to the spin-up states only. The 24 in (1.18) refers to 12 minority occupied states per unit cell: one with s character, three with p character and eight with d character. Note that for the eight occupied minority d states, it is composed of double-degenerated e_g, the triple-degenerated t_{2g} and triple-degenerated t_{1u} orbitals.
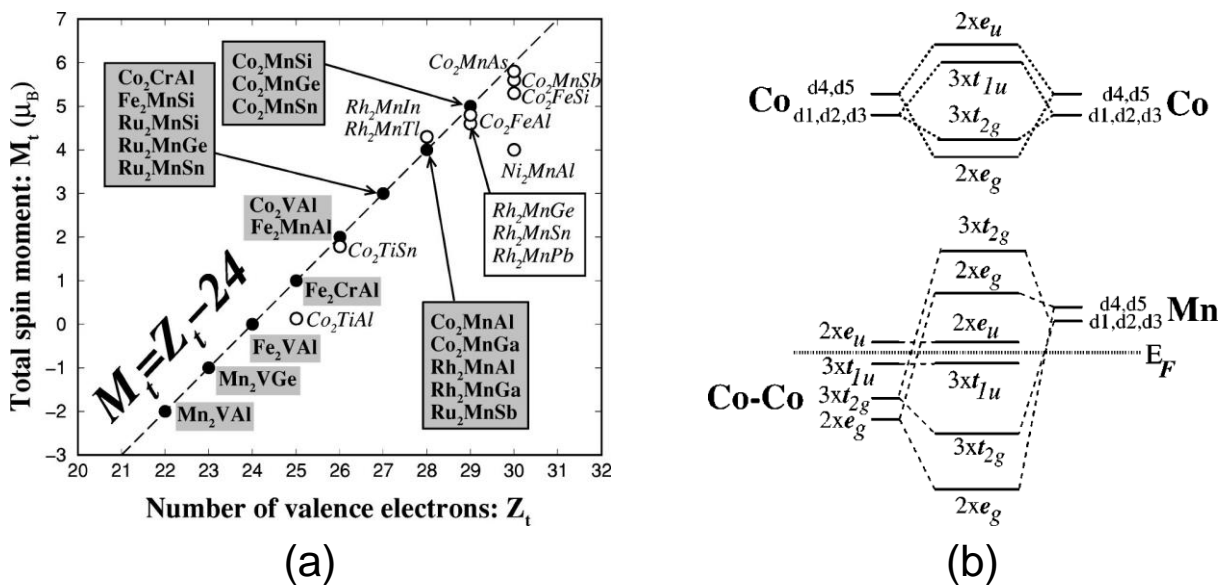

Fig. 1-16 (a) Full Heusler alloys that follow the Slate-Pauling rule. (b) Possible hybridizations between the two different Co atoms and between Co and Mn. From Ref. [27]

1.7 Purpose of study and thesis outline

As described in this chapter, the attainment of large CPP-GMR output is of paramount importance towards the potential realization of ultrahigh density magnetic recording (specifically, HDD read sensors) and microwave oscillators. Large bulk and interfacial spin-dependent scattering are key factors. Up to now, highly spin polarized Heusler alloys have been utilized to provide large bulk spin polarization, but a proper way to make the most of it is still lacking. Moreover, the investigation on new spacer materials is in demand because potential CPP-GMR output increase is expected by proper interfacial material engineering. From a practical point of view, the study on polycrystalline CPP-GMR devices is also necessary due to the limitation of current HDD read sensor fabrication. Proper choice of crystallographic orientation in FM and NM materials may affect the thermal stability of the polycrystalline CPP-GMR stack against interlayer atomic diffusion and multilayer delamination. Multilayer engineering of the CPP-GMR stack is in need to attain compatibility with the current fabrication process. Last but not least, the investigation of high-resistive spacer materials is strongly required to solve the problem of spin transfer torque induced magnetization instability, so that the critical current density of the read head sensor would be enhanced to achieve higher CPP-(G)MR output.

In short, the purpose of study of the thesis is as follows:

(1) To obtain large CPP-GMR output using full Heusler alloy and new spacer materials.

(2) To investigate the crystal orientation dependence of MR output in polycrystalline CPP-GMR devices and establish fabrication process for <001> textured polycrystalline devices.

(3) To obtain large voltage output in CPP-MR devices with high-resistive spacer material and investigate its transport mechanism as well as spin transfer torque suppression in CPP-MR devices.

The thesis will describe our CPP-GMR work in seven chapters.

Chapter 1 introduces the general background centered with spintronics (GMR) and the issues that motivate the work in the thesis.

Chapter 2 provides experimental procedures including sample preparation and devices fabrication.

Chapter 3 describes the work on fully epitaxial pseudo spin-valves using $Co_2Fe(Ge_{0.5}Ga_{0.5})$ (short as CFGG) Heusler alloy and novel AgZn spacer, in which large magnetoresistance output has been obtained.

Chapter 4 describes the preparation of <001> textured polycrystalline CPP-GMR devices with CFGG Heusler alloy and a Ag spacer layer using MgO or Mg-Ti-O buffer layer for industrial compatibility.

Chapter 5 describes the work of CPP-GMR pseudo spin-valves using ferromagnetic (FM) Heusler layer CFGG and nonmagnetic Heusler spacer Cu_2CrAl (CCA).

Chapter 6 describes the work of CPP-MR pseudo spin valves using CFGG as Heusler electrode and Mg-Ti-O as spacer material. Remarkable output voltage has been obtained and advantage has been shown for such CPP-MR junctions to replace the all-metallic CPP-GMR. Also the transport mechanism has been experimentally investigated in detail.

Chapter 7 provides summary and future perspectives on the CPP-MR work.

Chapter 2   Experimental procedures

2.1 Choice of the full Heusler alloy

In 2011, Takahashi *et al.*[28] reported a new full Heusler alloy system $Co_2Fe(Ga_xGe_{1-x})$. They experimentally demonstrated that the alloy shows maximum bulk spin polarization of nearly 70% at x=0.5 using the point contact Andreev reflection (PCAR) method (**Fig. 2-1**). The spin polarization value they obtained was one of the largest among all the Co-based full Heusler alloys. By
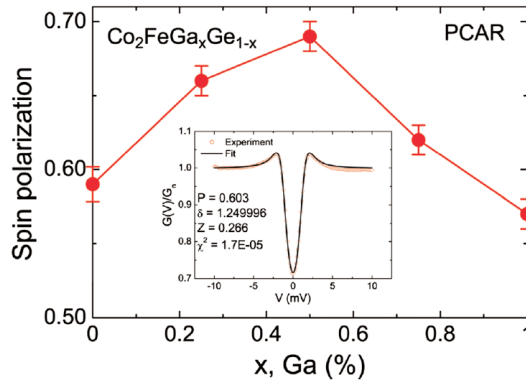

Fig. 2-1 Dependence of spin polarization of $Co_2Fe(Ga_xGe_{1-x})$ on x (Ga) content. From Ref. [28]
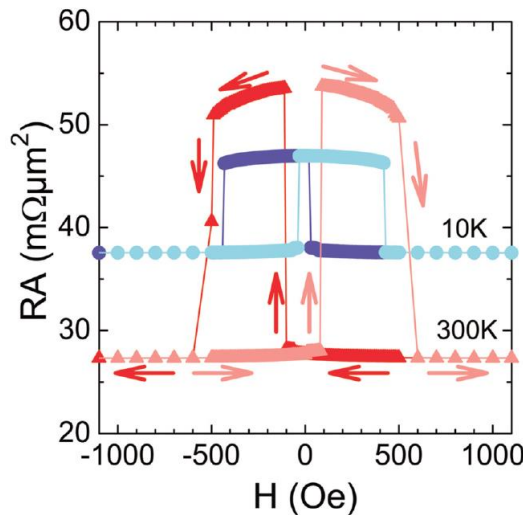
Fig. 2-2 MR curves of CFGG/Ag/CFGG PSV at 10 K and 300 K. Ref. [28]

incorporating such Heusler alloy with the optimized composition, namely $Co_2Fe(Ga_{0.5}Ge_{0.5})$, into a CPP-GMR device along with a Ag spacer layer, they obtained room-temperature MR and ΔRA of 41.7% and 9.5 $m\Omega\ \mu m^2$ (**Fig. 2-2**), respectively. By means of TEM observation they found that the $Co_2Fe(Ga_{0.5}Ge_{0.5})$ layer annealed at 500°C shows a B2 ordering. Their result indicated a potential

advantage of $Co_2Fe(Ga_{0.5}Ge_{0.5})$ that highly spin polarized current may be obtained from its thin film composed of even imperfect crystals.

Fortunately, such potential advantage was later supported. Varaprasad *et al.* [24] performed *ab initio* density of states (DOS) calculations for Co_2FeGe, $Co_2Fe(Ga_{0.5}Ge_{0.5})$ and Co_2FeGa alloys with the $L2_1$ and B2 structures (shown in **Fig. 2-3**). The DOS of $Co_2Fe(Ga_{0.5}Ge_{0.5})$ demonstrates no minority electronic states at E_F with both the $L2_1$ and B2 ordering, suggesting that the alloy is half-metallic for both orderings. Additionally, due to the fact that E_F of B2 ordered $Co_2Fe(Ga_{0.5}Ge_{0.5})$ is at the center of the band gap, the alloy may be able to reduce some minority DOS even with the occurrence of site-disorder at finite temperature. With large spin polarization as well as high thermal stability (as indicated in **1.6.3**), the $Co_2Fe(Ga_{0.5}Ge_{0.5})$ has been identified as a promising material for the fabrication of CPP-GMR.

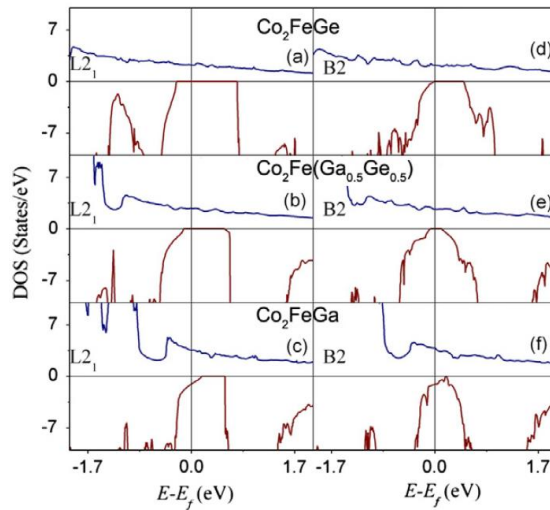**Fig. 2-3** Spin-resolved DOS of Co_2FeGe, $Co_2Fe(Ga_{0.5}Ge_{0.5})$ and Co_2FeGa alloys with the $L2_1$ and B2 structures. From Ref. [24]

2.2 Thin film deposition

All the thin films were deposited by a magnetron sputtering machine (Eiko Engineering Co., Ltd) with a base pressure better than 5×10^{-8} Pascal (Pa). The sputtering system equips ten 3-inchs targets with one cathode and dc/rf power supplies. The target-distance is fixed at 100 mm. The sputtering gas is high-purity Ar with working pressure ranging from 2.5-11.5 mTorr. The sputtering conditions for different targets are summarized in **Table 2-1**.

Material	Power	Gas flow mode/pressure	Sputtering rate
Ta	DC10	Pressure mode/3.0 mTorr	0.36 Å/s
Ru	DC20	Pressure mode/7.0 mTorr	0.66 Å/s
Ag	RF30	Pressure mode/5.0 mTorr	1.04 Å/s
Ag	RF30	Open mode, 18 sccm/1.5 mTorr	1.07 Å/s
CoFe	DC10	Pressure mode/3.0 mTorr	0.32 Å/s
Cr	DC10	Pressure mode/8.0 mTorr	0.55 Å/s
Cr	RF30	Open mode, 30 sccm/2.4 mTorr	0.20 Å/s
MgO	RF100	Pressure mode/5.0 mTorr	0.17 Å/s
$Co_2Mn(Ga_{0.25}Ge_{0.75})$	DC10	Pressure mode/8.0 mTorr	0.59 Å/s
$Co_2Fe(Ga_{0.5}Ge_{0.5})$	DC10	Position mode/6.0 mTorr	0.42 Å/s

Table 2-1 Sputtering condition used throughout the thesis.

The (001)MgO single crystalline substrates (Furuuchi Chemical Corp.) and thermally oxidized Si substrates (Si/SiO$_2$) were used in this study for thin film characterization and CPP-GMR device fabrication. The cleaning procedure of the substrates is given as follows,

1. Cut the substrate with a diamond pen.
2. Ultrasonically clean (UC) the substrates with acetone for 10 min.
3. UC the substrates again with fresh acetone for 10 min.
4. UC the substrates with deionized water for 5 min.
5. UC the substrates with isopropanol (IPA) for 10 min
(6). For MgO substrates, thermal flush them at 600°C for 30 min.

2.3 Microfabrication

The microfabrication of CPP-GMR devices is generally a combination of photo-/electron beam lithography and Ar ion etching. The photolithography was used for the patterning of the bottom electrode, SiO$_2$ isolation pad and top electrode. The electron beam lithography was for the build-up of the CPP-GMR pillar. The microfabrication work flow was shown in **Fig. 2-4** schematically.

2.3.1 Photolithography and electron beam (EB) lithography

➢ Photolithography

Resist: ma-N1407 negative resist   Promotor of adhesion: Hexamethyldisilazane (HDMS)

Process:

    (1) Spin coating of HMDS at 3500 rpm for 45 sec

    (2) Baking at 90°C for 2 min

    (3) Spin coating of ma-N1407 at 3500 rpm for 45 sec

    (4) Baking at 90°C for 1.5 min

    (5) Exposure for 90 sec

    (6) Development with ma-D533 for 80 sec

    (7) Ar ion milling or sputtering

➢ EB lithography

Resist: ma-N2403 negative resist   Promotor of adhesion: HDMS

Process:

    (1) Spin coating of HMDS at 3500 rpm for 45 sec

    (2) Baking at 90°C for 3 min

    (3) Spin coating of ma-N2403 at 3500 rpm for 45 sec

    (4) Baking at 90°C for 2 min

    (5) Spin coating of E-spacer at 3500 rpm for 45 sec, no post baking

    (6) Electron beam exposure

    (7) Development with ma-D532 for 80 sec

    (8) Ar ion milling

In the photolithography process, imperfect alignment for the SiO$_2$ isolation pad and top electrode would increase the chance of leak current. It is better to perform the lithography as perfect as possible. Meanwhile, the fabrication of the CPP-GMR pillar is the most critical process.

Carefully examining the focus and contrast as well as stigmatism would be indispensable in the EB lithography process.

2.3.2 General work flow

The complete microfabrication process is shown below in **Fig. 2-4**. Normally the microfabrication for a single device takes about 10 hours.
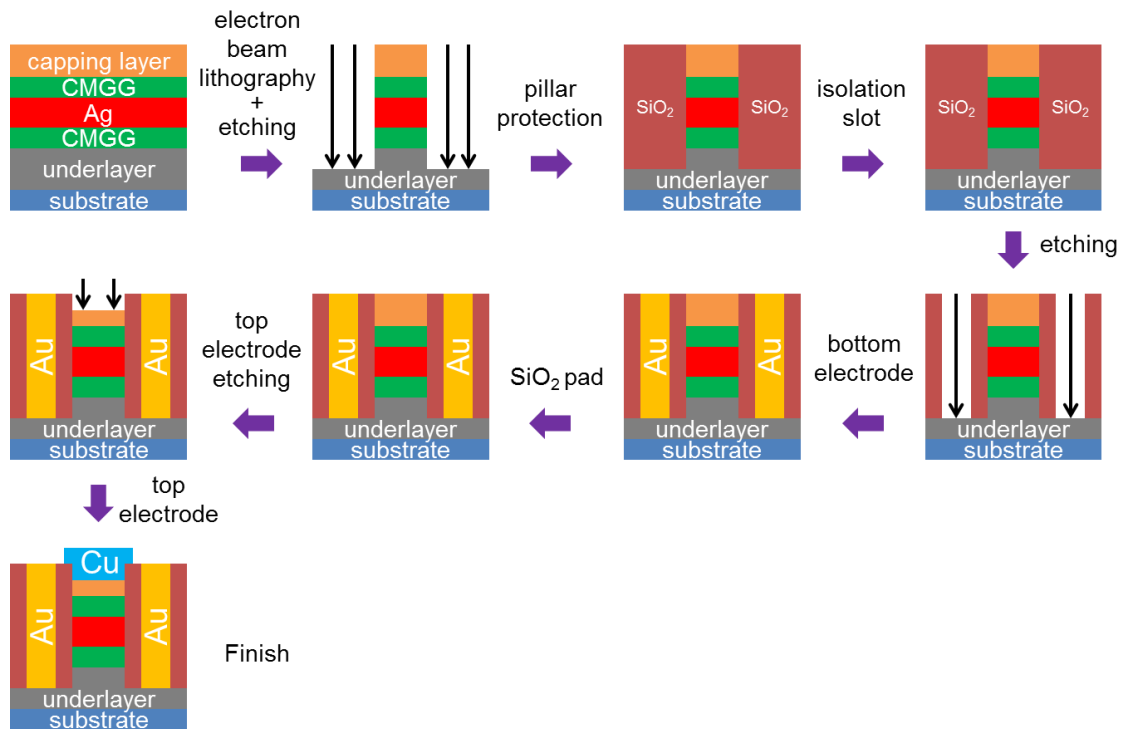

Fig. 2-4 Overall microfabrication work flow.

2.4   Thin film characterization

X-ray diffraction

The crystal structure of thin films was examined by a 4-axis diffractometer (Rigaku Corp.). The scanning modes used in this study were $\theta - 2\theta$ and φ scans.

Transmission electron microscopy

A transmission electron microscopy (FEI Titan 80-200 with aberration correction) was used for microstructure characterization of thin films as well as microfabricated CPP-GMR devices. The cross-sectional specimens were made using the following procedure.

(1) Cut the substrate into strips with a size of 1mm×1mm×5mm.

(2) Paste two strips face to face with film planes attached using epoxy glue.

(3) Manually polish the strip with emery papers down to ~30 μm.

(4) Fix the specimen onto molybdenum mesh (~3 mm diameter).

(5) Finely polish the specimen using Gatan Precision Ion Polishing System (PIPS) with liquid N_2 cold stage.

Note that the liquid N_2 cold stage is necessary to prevent contaminations of the Ag underlayer that is always required for the CPP-GMR multilayer.

Vibrating sample magnetometer

The magnetic properties of the thin film were characterized by a vibrating sample magnetometer (VSM) (Lakeshore Cryotronics, Inc.).

Atomic force microscopy

The morphology of the thin film surface was examined by atomic force microscopy.

2.5   Magnetoresistance measurement

The CPP-GMR property was measured using a traditional dc 4-probe system with a constant current source ranging from 0.1 mA-7 mA. The low temperature measurement was performed using a physical property measurement system (PPMS).

Chapter 3　Large MR output in pseudo spin-valves with Co₂Fe(Ga₀.₅Ge₀.₅) Heusler alloy and Ag-based alloy spacer

3.1　Introduction

In recent years, the CPP-GMR output in all-metallic pseudo spin valves (PSVs) has been substantially enhanced using highly spin-polarized Co-based Heusler alloys such as $Co_2Fe(Ga_{0.5}Ge_{0.5})$ (CFGG)[28,29] or $Co_2(Fe_{0.4}Mn_{0.6})Si$ (CFMS)[30–32] with a Ag spacer layer. The MR ratios have reached above 40% with the resistance-change area product (ΔRA) of 9-12 mΩ μm². However, a room temperature (RT) ΔRA of at least 15 mΩ μm² is required for using CPP-GMR as sensors for areal density over 2 Tbit/in². Therefore, further increase of the CPP-GMR output is strongly required.

According to the Valet and Fert's model of CPP-GMR,[11] ΔRA is composed of bulk and interfacial components. While the bulk component is determined solely by the spin polarization of FM layers, the interfacial component originates from the spin-dependent scattering at the FM/NM interface, which is considered to depend on both crystal and band structures. By selecting a proper combination of FM/NM materials, the interfacial spin-dependent scattering may be enhanced, which will lead to the enhancement of ΔRA. With this expectation, several spacer materials have been investigated. Nikolaev *et al.*[33] used a Heusler alloy Rh_2CuSn with the $L2_1$ structure based on theoretically predicted favorable band matching. However, low MR output was observed in their system due to the occurrence of Co-Mn disorder in their Heusler alloy layer. Hase *et al.*[34] demonstrated the feasibility of utilizing a B2-ordered NiAl intermetallic compound, although the ΔRA of less than 5 mΩ μm² was reported possibly due to the short spin diffusion length of the NiAl spacer.
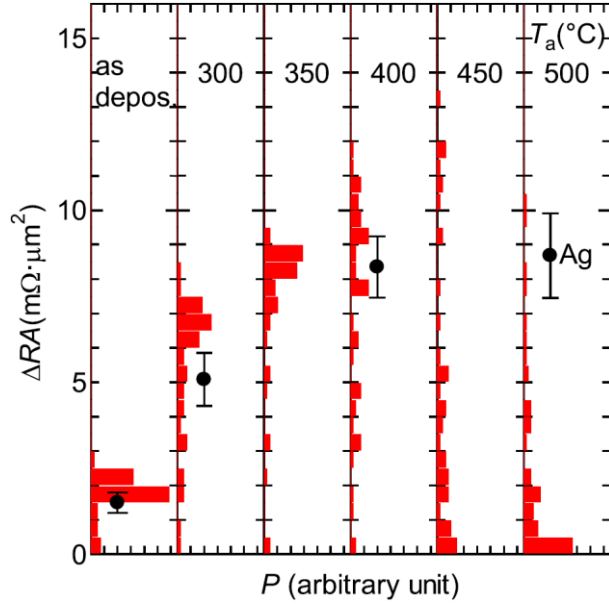
Fig. 3-1 Distribution of ΔRA for CPP-GMR devices using CuZn spacer layer with different annealing temperature (T_{an}). The PSVs with Ag spacer is shown as comparison. From Ref. [35]

Very recently, Furubayashi *et al.*[35] reported CPP-GMR devices using a bcc-based spacer material CuZn (**Fig. 3-1**). At relatively low annealing temperature (T_{an}) of 350°C, the CPP pseudo spin-valves (PSVs) exhibit a comparatively large ΔRA of 8 mΩ μm^2, which is higher than the CPP-PSV with Ag with the same annealing condition. However, with the CuZn spacer, the ΔRA degrades when T_{an} increases above 400°C due to the deterioration of the multilayer structure, where Ag diffuses into the spacer layer region and Cu and Zn segregate at the CFGG/Ag interfaces (**Fig. 3-2**). The low device thermal stability makes it difficult for CFGG to achieve the $L2_1$ order, which is a necessary condition for high spin polarization, β, in full-Heusler alloys. In this chapter, we show an enhancement of the CPP-GMR output observed from a PSV device using CFGG Heusler alloy combined with Ag-based alloy spacers.
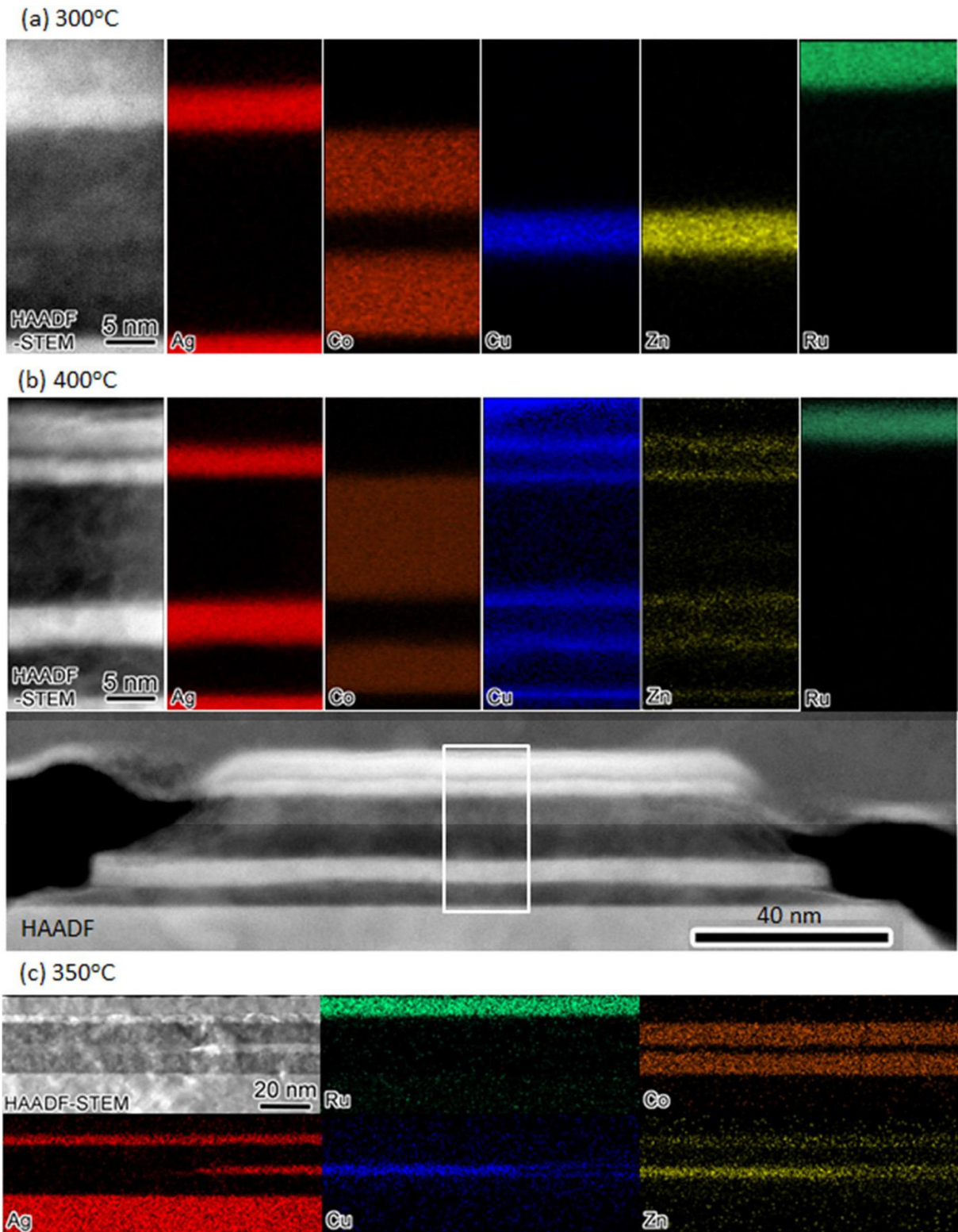
Fig. 3-2 TEM images and elemental mappings of PSVs with CuZn spacer with different T_{an}. From Ref. [35]

34

3.2 Choice of spacer material

In this study we have chosen two Ag-based spacer material systems, namely, the Ag-Mg and Ag-Zn systems. The phase diagram of the two systems is shown in **Fig. 3-3**. For the case of Ag-Mg, a room temperature $L1_2$ phase with the atomic ratio of Ag:Mg=3:1 can be one potential spacer candidate because of its 4-fold fcc-like crystal structure which is very similar to Ag, and its small lattice misfit (less than 2%) with the Heusler layer assuming a potential rotation epitaxy relationship. According to the phase diagram (**Fig. 3-3** (a)), the Ag_3Mg alloy can be stable up to ~392°C if its composition is properly tuned. This is a desirable feature because for epitaxial PSV with Heusler layer it has to be annealed to acquire improved chemical ordering.
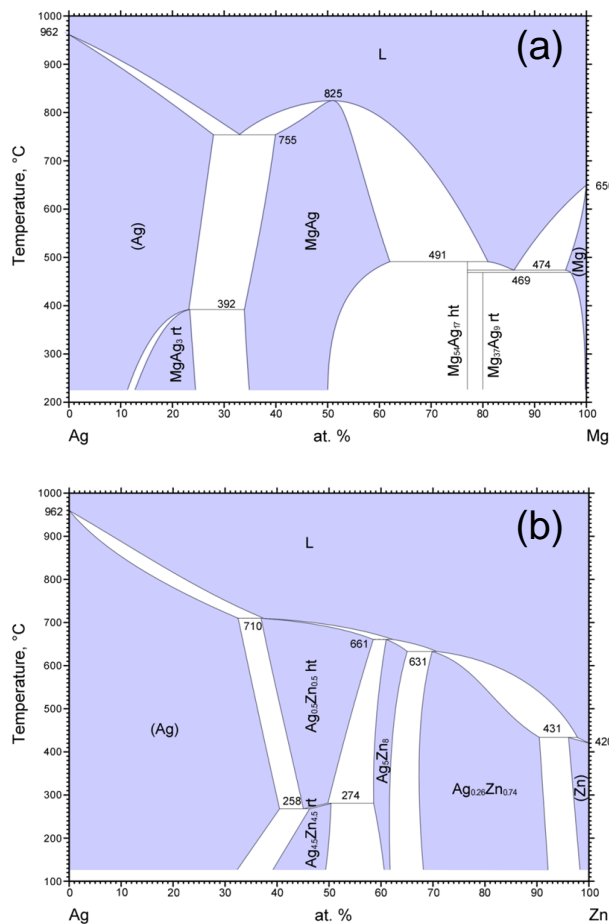

Fig. 3-3 Phase diagrams of the Ag-Mg system and Ag-Zn system. By ASM phase diagram.

For the case of Ag-Zn system, a possible spacer candidate would be the high temperature metastable phase[36] with the composition of Ag:Zn=1:1, which has a bcc-based crystal structure and a moderate lattice misfit of ~7% with the Heusler alloy layer (**Fig. 3-3** (b)).
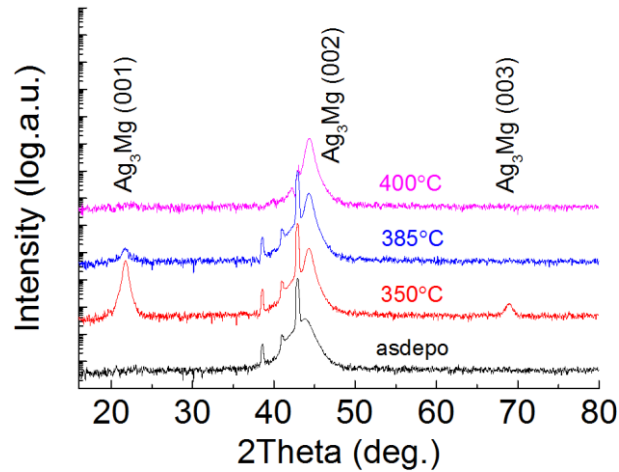
Fig. 3-4 $\theta - 2\theta$ scan of film stack MgO//Ag$_3$Mg(30)/Ru(2), thickness in nm.

Fig. 3-4 shows the result of $\theta - 2\theta$ scan of film stack MgO//Ag$_3$Mg(30)/Ru(2) (thickness in nm) for the structural characterization of single layer Ag$_3$Mg. As a result, the as-deposited film shows disordered fcc phase as indicated by the only fundamental peak of Ag$_3$Mg (002). When anneal the stack at 350°C the superlattice peaks of Ag$_3$Mg (001) and Ag$_3$Mg (003) appears suggesting the appearance of L1$_2$ ordering. Further increasing the annealing temperature leads to the reduction of the superlattice peak intensity suggesting that the L1$_2$ ordering deteriorates. As for the AgZn single layer (not shown), a B2 ordering superlattice peak of AgZn (001) was observed only for the as-deposited film.

As for the characterization of the full CPP-GMR multilayer stack, **Fig. 3-5** shows the $\theta - 2\theta$ scan of film stack MgO//Cr(10)/Ag(100)/CFGG(10)/spacer(5)/CFGG(10)/Ag(5)/Ru(8), in which the spacer is (a) Ag$_3$Mg and (b) AgZn. The appearance of Cr (002), Ag (002), CFGG (004) suggests desirable epitaxial growth of the multilayer with both spacer layers. The CFGG (002) peak observed for both stacks suggests B2 ordering of the Heusler layer (note that L2$_1$ ordering is possible for annealing temperatures higher than 500°C). For the Ag$_3$Mg, no superlattice peak is observed for all samples, but this may be due to the insufficient diffraction intensity coming from the thin spacer layer. For the case of AgZn spacer, however, a broad AgZn (001) peak is observed for the as-deposited film, suggesting a weak B2 ordering with potentially tilted crystals.
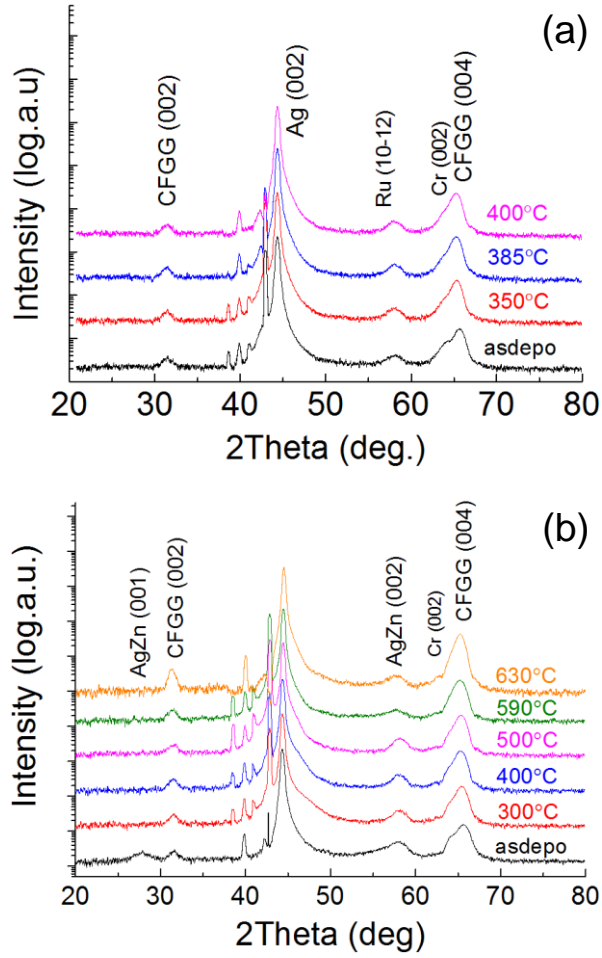
Fig. 3-5 $\theta - 2\theta$ scan of the CPP-GMR multilayer stacks of MgO//Cr(10)/Ag(100)/CFGG(10)/spacer(5)/CFGG(10)/Ag(5)/Ru(8) (thickness in nm), in which the spacer is (a) Ag$_3$Mg and (b) AgZn.

3.3 Magneto-transport properties

3.3.1 PSVs with AgZn spacer layer

Based on the result of the ordering characterization in section **3.2**, we fabricated PSVs with CPP-GMR multilayer thin film stack annealed at different temperature. The device structure is as follows: MgO//Cr(10)/Ag(100)/CFGG(10)/spacer(5)/CFGG(10)/Ag(5)/Ru(8) (thickness in nm), the spacer is Ag$_3$Mg and AgZn. For the case of AgZn spacer layer, **Fig. 3-6** shows the raw *R-H* curves of CPP-GMR devices using CFGG Heusler alloy layer and AgZn spacer layer with different annealing temperature. The directly measured MR ratio shows a monotonic increase from 350°C to 630°C.
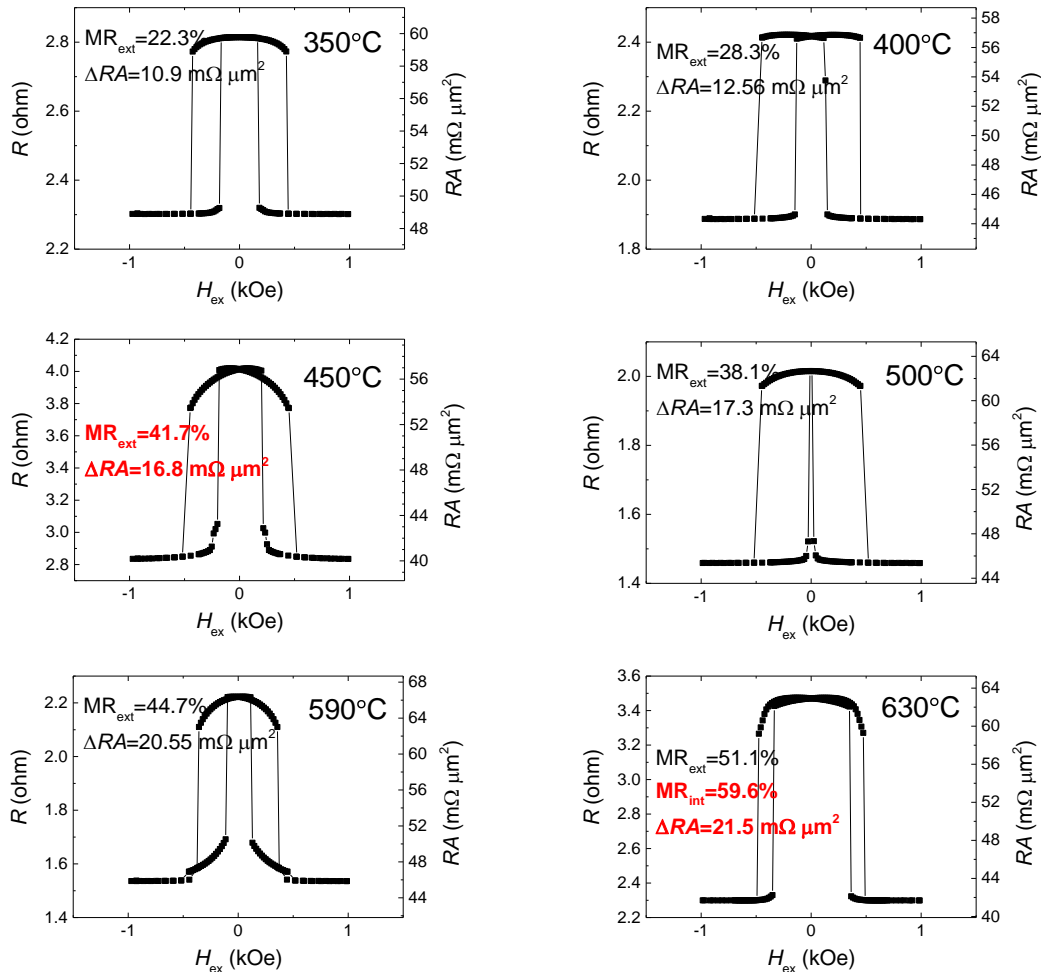

Fig. 3-6 Raw *R-H* curves of CPP-GMR devices using CFGG Heusler alloy layer and AgZn spacer layer with different annealing temperature.
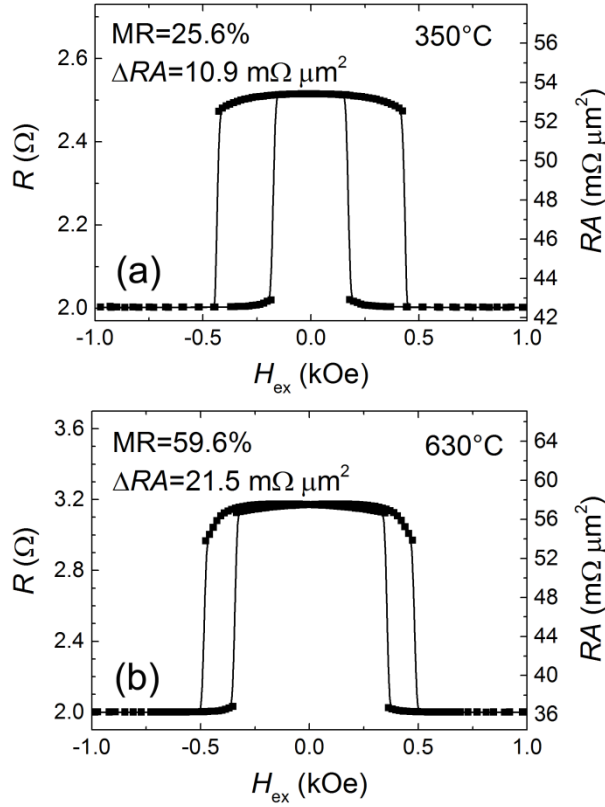
Fig. 3-7 Typical MR curves of CPP-PSVs micro-fabricated from the film stack of MgO//Cr(10)/Ag(100)/CFGG(10)/AgZn(5)/CFGG(10)/Ag(5)/Ru(8) with (a) T_{an} = 350°C and (b) T_{an} = 630°C (the parasitic resistance of 0.3 Ω has been subtracted).

However, the raw MR data do not reflect the intrinsic property of the CPP-GMR devices. After subtracting the parasitic resistance R_{para} of 0.3 Ω coming from the Cr/Ag underlayer, we obtain the intrinsic MR ratio and resistance-area product for the parallel magnetization state R_pA. **Fig. 3-7** shows the typical MR curves of CPP-PSV junctions measured at RT for (a) T_{an} = 350°C and (b) T_{an} = 630°C. The device annealed at 350°C shows a MR ratio of 25.6% (the raw MR ratio without subtracting R_{lead}: MR_{raw} = 22.3%) and ΔRA of 10.9 mΩ μm^2 with the R_pA = 42.6 mΩ μm^2. The MR ratio of the device annealed at T_{an} = 630°C is further enhanced to 59.6% (MR_{raw} = 51.1%) with ΔRA of 21.5 mΩ μm^2 and slightly decreased R_pA of 36.1 mΩ μm^2. Note that although the MR ratios are more or less the same as that of the CPP-PSV using a Ag spacer,[29,30] the value of ΔRA is 80% larger than that obtained from PSVs with the Ag spacer. The T_{an} dependence of ΔRA and MR ratios is shown in **Fig. 3-8**. For comparison, the previously reported values for the Ag spacer are also included in the figure. The ΔRA of the devices using the AgZn spacer increases monotonically with annealing temperature up to 630°C as shown in **Fig. 3-8** (a). In the whole temperature range, ΔRA of the PSVs with the AgZn spacer is larger than that of PSVs using the Ag spacer. In **Fig. 3-8** (b), The MR ratio shows a similar tendency as ΔRA with increasing T_{an}, while R_pA experiences a slight

decrease as T_{an} increases, which mainly arises from the decrease of the resistivity of CFGG. Room-temperature measurement shows that the resistivity of CFGG drops from ~110 µΩ cm to ~60 µΩ cm when annealing temperature increases from 350ºC to 630ºC, thus the RA drop coming from CFGG resistivity alone would be $\Delta\rho^* t_F = 50\times20\times10^{-2} = 10$ mΩ µm^2, which is close to the $R_p A$ drop observed in this study. The resistivity of Heusler alloys have a tendency to decrease when annealed at high temperatures due to the increase in the degree of chemical order, which is different from conventional 3d ferromagnetic (FM) metals or binary alloys like CoFe.
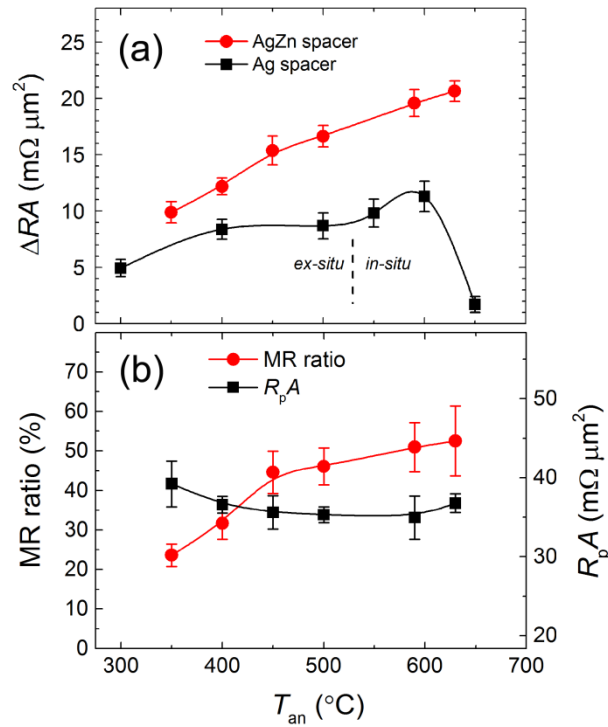

Fig. 3-8 (a) Annealing temperature dependence of ΔRA for a AgZn spacer (circles) and a Ag spacer (squares). (b) Annealing temperature dependence of intrinsic MR ratios (circles) and intrinsic $R_p A$ (squares) for a AgZn spacer.
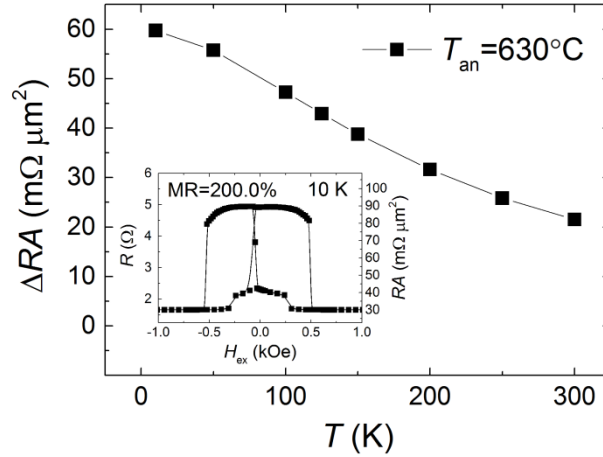
Fig. 3-9 Temperature dependence of ΔRA for CPP-PSV (T_{an} = 630°C) shown in **Fig. 3-7** (b). Inset is the MR curve at 10 K.

In addition, low temperature measurement was carried out for the particular device annealed at 630°C that shows remarkably large MR ratio of 60%. **Fig. 3-9** exhibits the temperature dependence of ΔRA for the CPP-GMR device annealed at 630°C with temperature ranging from 10-300 K. As a result, ΔRA increases as the measurement temperature decreases, which is common feature for Heusler-alloy-based CPP-GMR. The device annealed at 630°C shows ΔRA of 59.8 mΩ μm^2 with a large MR ratio of 200.0% (MR$_{raw}$ = 185.4%) at 10 K. The increasing ΔRA with decreasing measuring temperature is in general attributed to the enhancement of both bulk spin polarization β of CFGG and the interfacial spin asymmetry γ at CFGG/Ag interface as reported for the CFGG/Ag/CFGG PSV.[29]

41

3.3.2 PSVs with Ag$_3$Mg spacer layer

Fig. 3-10 shows the *R-H* curves of CPP-GMR devices using CFGG Heusler alloy layer and Ag$_3$Mg spacer layer with different annealing temperature. As a result, the ΔRA shows higher value than PSVs with Ag spacer for same annealing temperature, and the device annealed at 385°C shows maximum MR ratio of 20% as well as ΔRA of 11 mΩ μm^2. The reason for the increase of MR output when using Ag$_3$Mg instead of Ag spacer is a possible increase in the interfacial resistance, as indicated by an enhancement of device *RA*. On the other hand, although there is a drastic decrease in the L1$_2$ ordering for the Ag$_3$Mg thin film layer as the annealing temperature increases from 350°C to 385°C as shown in section **3.2**, the ΔRA still increases slightly, which is probably owing to an increase in the chemical ordering of CFGG that enhances its bulk spin polarization. As the annealing temperature further rises up to 400°C, the ΔRA starts to decrease. One possible reason is the decrease in the effective spin-dependent interfacial scattering induced by drastic chemical disordering in the Ag$_3$Mg layer.
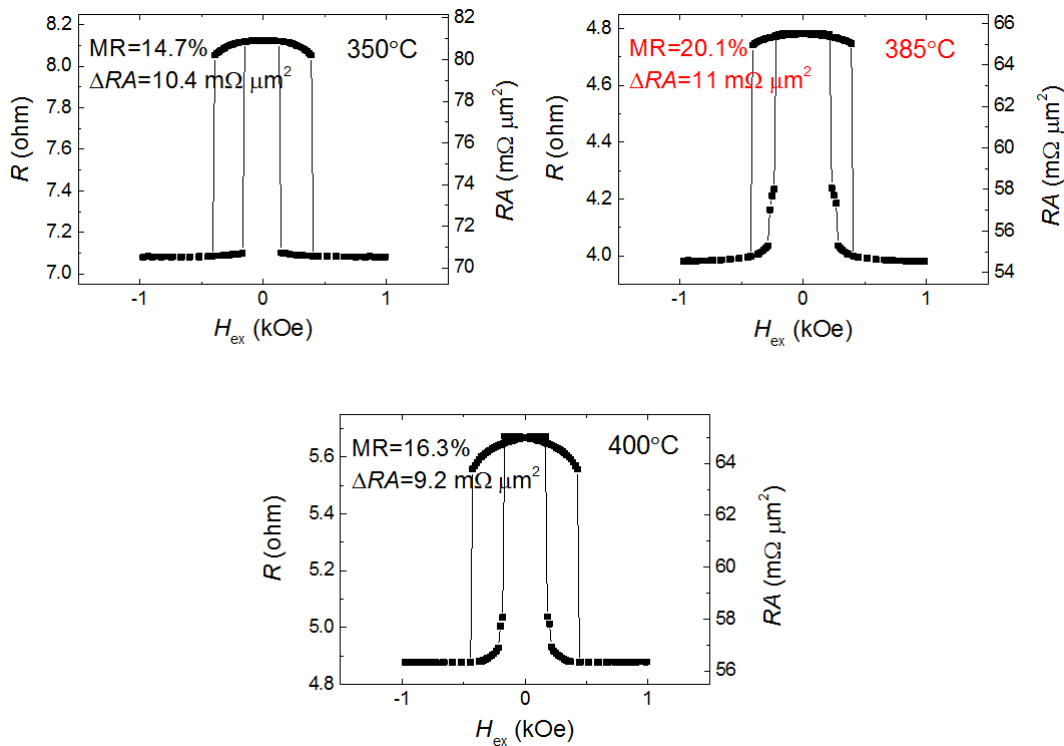

Fig. 3-10 *R-H* curves of CPP-GMR devices using CFGG Heusler alloy layer and Ag$_3$Mg spacer layer with different annealing temperature.

3.3.3 Ag-based alloy spacer vs. Ag spacer for PSVs

As a summary, the room temperature ΔRA of PSVs with Ag-based alloy spacer and Ag metal spacer has been summarized in **Fig. 3-11**. The Ag-based alloy spacer seems to exhibit higher ΔRA for the whole temperature range. For the low T_{an} region where no structural change of the multilayer is expected to happen, the reason of such ΔRA discrepancy may come from an interfacial effect, e.g. a potential improvement of the band matching at the FM/NM interface that causes the increased interfacial spin-dependent scattering asymmetry γ, or a potential degeneration of the band matching that causes an increase of the interfacial resistance $R_{F/N}A$. For the high T_{an} region, however, one must take into account of the possible nanoscale structural change, especially for these two alloy spacers containing high vapor pressure elements of Mg and Zn.
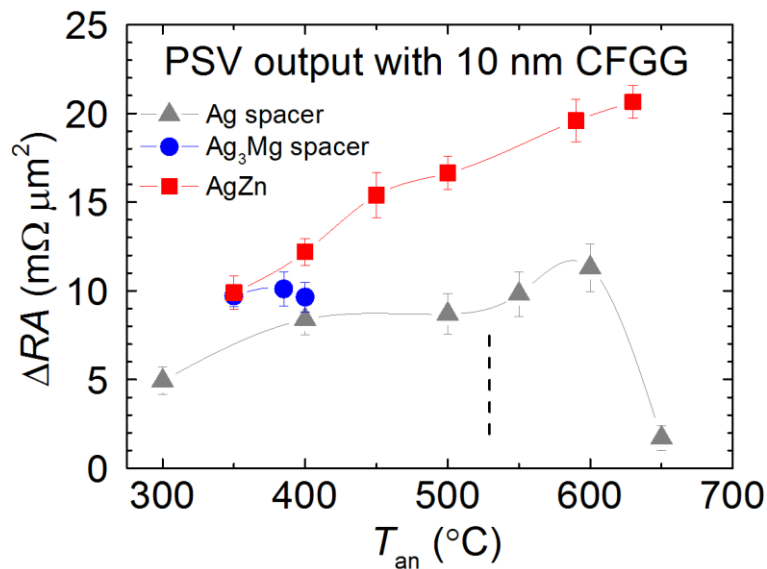

Fig. 3-11 Summary of the ΔRA of PSVs with Ag-based alloy spacer and Ag metal spacer.

3.4 Structural characterization

In order to clarify the reason for the large MR output for CPP-PSVs with the AgZn spacer, the microstructure of the multilayer film stack was characterized by TEM. **Fig. 3-12** shows the HAADF-STEM images and EDS elemental maps of Co, Fe, Ag, Zn and Ru obtained from micro-fabricated CPP-PSV pillars for $T_{an} = 350°C$ and $630°C$. Well-defined multilayer structure suggests the formation of continuous CFGG and spacer layers with flat interfaces in the device annealed at $350°C$. From the EDS analysis, the atomic content of the AgZn layer is estimated to be $Ag:Zn \approx 1:0.3$. Note that it was close to be 1:1 in the as-deposited state. At $630°C$, most of the Zn diffuses away from the spacer layer. Despite the substantial Zn diffusion, the two CFGG layers remain intact. Note that the CFGG composition after annealing at $630°C$ becomes $Co_{48.0}Fe_{26.2}Ga_{11.8}Ge_{14}$, with Ga slightly diffused out compared to the original film. In the spacer region, the Zn atomic concentration is less than 1%. **Fig. 3-13** shows the NBED patterns taken from the top CFGG, spacer and bottom CFGG layers with beam direction of $g = [110]_{CFGG}$ for the as-deposited CPP-PSV film and the films annealed at $350°C$ and $630°C$. NBED patterns of the spacer layer were also taken from the direction with $z = [100]_{CFGG}$ to identify the structure in the annealed samples. In the as-deposited sample, both bottom and top CFGG layers have the B2-ordered structure as the (002) superlattice spots indicate. The structure of the AgZn spacer layer is identified as a B2 phase (CsCl type, $a = 0.3088$ nm)[36] with the orientation relationship (OR) described as $(001)[110]_{CFGG}//(001)[110]_{AgZn}$. Although the CFGG layers keep the B2-ordered structure after annealing at $350°C$, their structures change to $L2_1$ structure as evidenced by the (111) diffraction spots after annealing at $630°C$. The structure of the spacer layer cannot be uniquely determined from the $[110]_{CFGG}$ zone axis alone. However, the NBED patterns taken from the $[100]_{CFGG}$ zone show that the spacer layer in the samples annealed $350°C$ and $630°C$ has the fcc structure (Cu type, $a = 0.4086$ nm). The OR between the CFGG and the fcc spacer layer changes to $(001)[110]_{CFGG}//(001)[100]_{fcc\ AgZn}$. The fcc phase formation in the sample annealed at $350°C$ is reasonable since the Zn is depleted from the initially $Ag_{50}Zn_{50}$ layer. At $630°C$, since most of Zn diffuses out from the spacer region, the remaining Ag layer shows the fcc structure, as evidenced from the NBED patterns taken along the $[110]_{CFGG}$ and $[100]_{CFGG}$ zone axes.
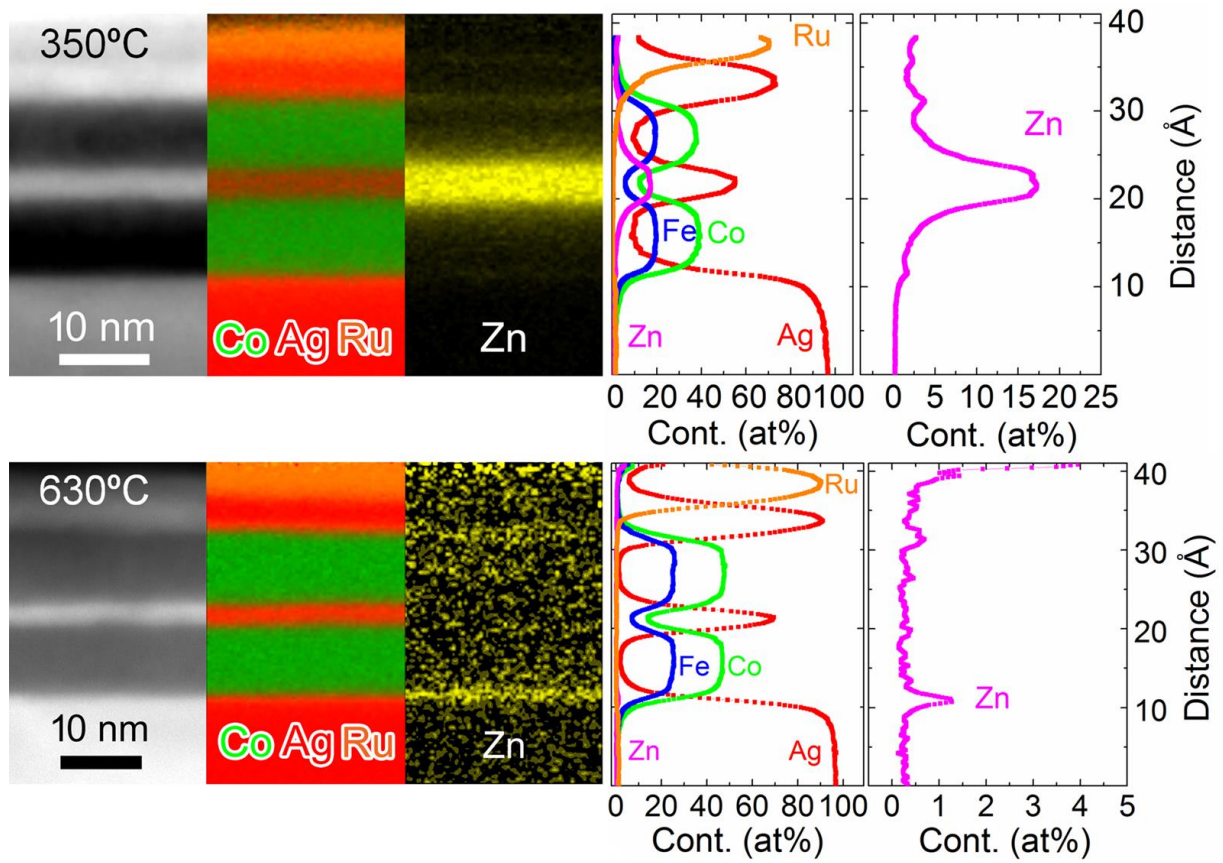
Fig. 3-12 HAADF-STEM images and EDS mappings for the thin film structure of MgO//Cr(10)/Ag(100)/CFGG(10)/AgZn(5)/CFGG(10)/Ag(5)/Ru(8) annealed at 350°C and 630°C.
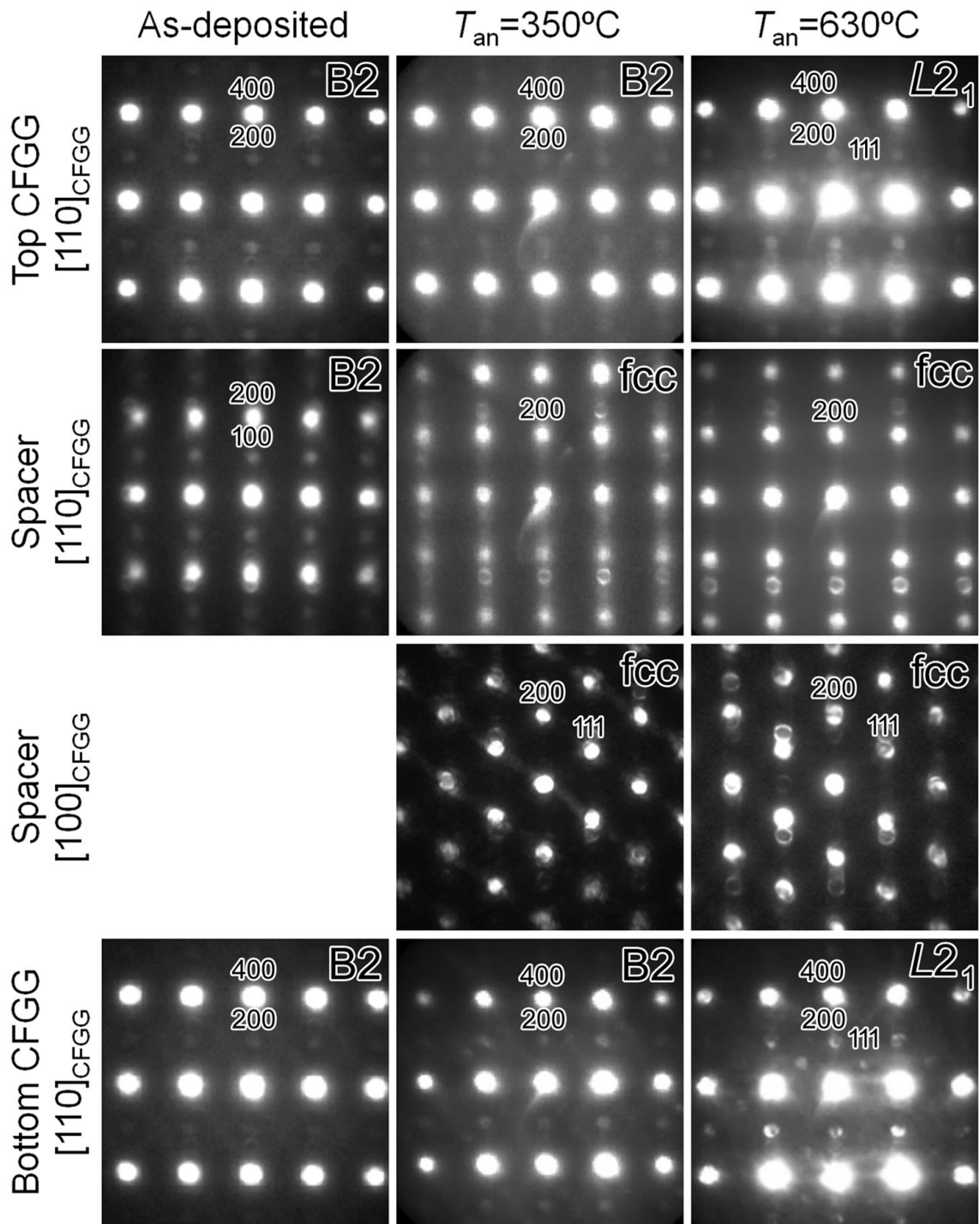
Fig. 3-13 Nano-beam diffraction patterns (NBDPs) for the as-deposited film and the films annealed at 350°C and 630°C with beam direction of $z=$ [110]$_{CFGG}$. The NBDPs of spacer layer with $z =$ [100]$_{CFGG}$ is also shown to identify the spacer structure.

46

3.5 Discussion

As noted in section **3.4**, with high T_{an} = 630°C, the Zn completely diffuses out of the spacer region, leaving the spacer layer primarily composed of Ag only. One may argue that the ΔRA then should be the same (or at least close) to the PSV with Ag spacer as shown in Li's paper[29]. However, in this study the structural change has been proved to exert a considerable impact on the MR performance. **Fig. 3-14** shows the XRD profiles of the $2\theta - \varphi$ scans for the film stack of MgO//Cr(10)/Ag(100)/CFGG(10)/spacer(5)/CFGG(10)/Ag(5)/Ru(8) films *in-situ* annealed at 630°C, where spacer = Ag or AgZn. The measurement conditions were set for collecting the reflections from the CFGG {111} planes. The non-linear background signal is due to the 2-dimensional detector set up during our XRD measurement, which does not influence the results obtained. The film stack with the AgZn spacer shows stronger (111) diffraction peak compared to that with the Ag spacer. This suggests that the diffusion of Zn contributes to the increase of the degree of the $L2_1$ order in CFGG, which probably results in an enhancement of spin polarization in the CFGG layers and accounts for the larger ΔRA at 630°C. The integral intensity ratio I_{111} / I_{444}, which is proportional to the square of the degree of $L2_1$ order, was also calculated for both films. The I_{111} / I_{444} ratio for the film stack with the AgZn layer turns out to be 28% higher than that with the Ag spacer, which confirms the enhancement of the degree of $L2_1$ order for the films with the AgZn spacer.

We then confirmed such degree of $L2_1$ order enhancement in the same multilayer system with varying CFGG thickness. **Fig. 3-15** shows the XRD profiles with same diffraction mode for the film stack of MgO//Cr(10)/Ag(100)/CFGG(t_F)/spacer(5)/CFGG(t_F)/Ag(5)/Ru(8) with T_{an} = 630°C, where spacer = Ag or AgZn and t_F = 7, 10, 13, 15 nm. For all the CFGG thickness, there is an enhancement of diffraction intensity for CFGG (111) peak when replacing the Ag spacer with AgZn spacer. Note that here we assume for all the films the Zn completely diffuses out of the multilayer stack.
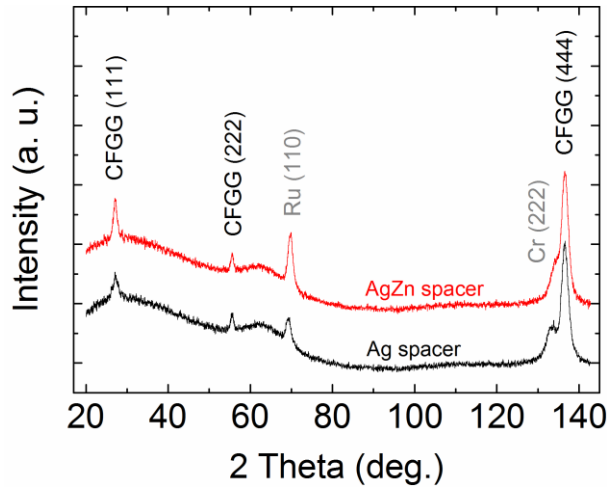
Fig. 3-14 $2\theta - \varphi$ scan x-ray profiles of MgO//Cr(10)/Ag(100)/CFGG(10)/spacer(5)/CFGG(10)/Ag(5)/Ru(8) films annealed at 630°C, where spacer = Ag or AgZn. The measurement conditions were set for collecting the reflections from the CFGG {111} planes.
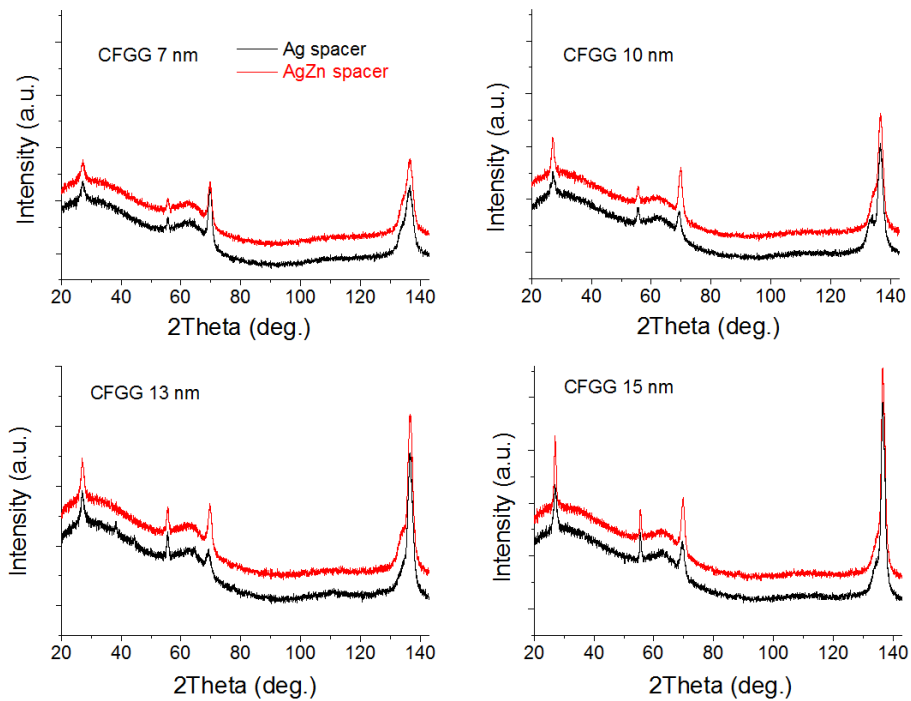

Fig. 3-15 $2\theta - \varphi$ scan x-ray profiles of MgO//Cr(10)/Ag(100)/CFGG(t_F)/spacer(5)/CFGG(t_F)/Ag(5)/Ru(8) films annealed at 630°C, where spacer = Ag or AgZn, t_F =7, 10, 13, 15 nm. The measurement conditions were set for collecting the reflections from the CFGG {111} planes.

At lower annealing temperatures, e.g. 350°C, Zn still remains in the AgZn spacer layer; nevertheless the ΔRA of 10.9 mΩ μm^2 for the PSV with the AgZn spacer layer is higher than that with Ag spacer. This suggests that Zn addition has additional role in enhancing ΔRA even by annealing at a relatively low temperature. In **Fig. 3-8** (b), the R_pA for the AgZn spacer at 350ºC is

around 36-42 mΩ μm^2, which is larger than the value of 20-25 mΩ μm^2 for the Ag spacer. This suggests that the interfacial resistance ($R_{F/N}A$) increases when we use AgZn spacer instead of Ag spacer, which is considered to be due to the segregation of Zn at Ag/CFGG interfaces as shown in **Fig. 3-12**. According to the Valet-Fert model,[11] the increase in $R_{F/N}$ leads to the increase in ΔRA. Recently, Narisawa et al.[37] reported large MR output for the CPP-GMR devices using $Co_2Fe_{0.4}Mn_{0.6}Si$ Heusler alloy combined with $L1_2$ ordered Ag-Mg alloy for the spacer. The value of R_pA using the Ag-Mg spacer was reported to be even higher (50 mΩ μm^2), which also suggests that an increase of $R_{F/N}$ is another possible reason for the enhancement of ΔRA at low annealing temperature.

As for the potential application of CPP-GMR devices as a read sensor in ultrahigh areal density HDDs, the combination of MR ratio and RA values obtained from the CFGG/AgZn/CFGG PSVs already fulfills the requirement for the recording density of 2 Tbit/in^2 calculated by Takagishi et al.[14] However, one should note that a stringent narrow reader gap is required for ultrahigh density magnetic recording, e.g. less than 20 nm for 2 Tbit/in^2.[14] Also, the readers must be grown on permalloy shield with different stacking structure which does not allow for annealing temperature higher than 350ºC. In this work, the epitaxial CFGG/AgZn/CFGG CPP-PSV has shown the ΔRA value of 10.9 mΩ μm^2 for the annealing temperature of 350°C, which is higher than that was reported by Diao et al.[38] from polycrystalline CPP spin valves that was annealed at 350°C. This indicates the usage of AgZn spacer is advantageous to reduce the annealing temperature for getting sufficient ΔRA value. However, the large MR output of ΔRA of 21.5 mΩ μm^2 is obtained only by annealing the device at a very high temperature of 630°C. Such a high annealing temperature cannot be applied to any polycrystalline device as the layered structure of polycrystalline devices is not so tolerable against thermal annealing. One possible solution is to make a single-crystalline device using a wafer-bonding technology,[39] which will remove the T_{an} limit of 350°C primarily due to the thermal tolerance of permalloy shield and the instability of the polycrystalline layered structure. Nevertheless, the demonstration of the large MR ratio of 59.6% and ΔRA of 21.5 mΩ μm^2 at room temperature by utilizing the Zn diffusion is very encouraging for the development of MR sensors with low RA.

3.6 Summary of the chapter

In conclusion, we fabricated fully epitaxial CPP-PSV devices using CFGG Heusler alloy as FM layers and AgZn alloy as a spacer. Large MR ratio of 59.6% (ΔRA = 21.5 mΩ μm^2) was obtained at 300 K for the CPP-PSV annealed at 630°C using 10 nm CFGG layer and 5 nm AgZn spacer layer. At 10 K, the MR ratio increases to 200.0% (ΔRA = 59.8 mΩ μm^2). HAADF-STEM images and EDS mappings revealed that Zn has almost completely diffused out from the CPP-PSV device after annealing at T_{an} = 630°C, thereby enhancing $L2_1$ ordering in CFGG. The high degree of $L2_1$ order of CFGG is considered to result in high spin polarization of CFGG. The method for enhancing $L2_1$ ordering and high spin polarization of Heusler alloy by utilizing the diffusion of Zn would be useful not only for CPP-GMR but also for other spintronic applications. The PSV shows relatively large ΔRA of 10.9 mΩ μm^2 with the MR ratio of 25.6% for the low annealing temperature of 350°C, which is a practically useful feature for read sensor applications.

Chapter 4　　Preparation of <001> textured polycrystalline CPP-GMR pseudo spin-valves with MgO and Mg-Ti-O buffer layers

4.1　Introduction

In recent years, large MR output of the CPP-GMR devices using Heusler alloys as FM layers has already been demonstrated using fully epitaxial pseudo spin valves (PSVs) grown on (001) MgO single crystalline substrates. From a practical standpoint, however, the industry would consider only polycrystalline thin films for actual devices fabrication. Recently, Carey *et al.*[40] and Nakatani *et al.*[41] reported the resistance-change area product (ΔRA), of ~4 mΩ μm^2 in polycrystalline pseudo spin valves (PSVs) using Co-based Heusler alloys and a Ag spacer. Nakatani *et al*. pointed out that the MR output obtained in polycrystalline PSVs was somewhat lower than that obtained from the epitaxial PSVs grown on (001) MgO substrates. Du *et al.*[42] reported similar MR outputs for the Co$_2$Mn-based polycrystalline Heusler alloy. In these reports, the FM Heusler layers showed <011> texture for the B2-ordered or A2-disordered thin films while the Ag spacer layer exhibited <111> texture. Since {011} planes are the densely packed planes in the bcc structure, the B2-ordered CoFe or Heusler alloy layers show natural growth of the <011> texture. Using nanobeam electron diffraction, Nakatani *et al*. have shown that each Heusler alloy grain has an orientation relationship (OR) of [011](100)$_{Heusler}$//[111](1$\bar{1}$0)$_{Ag}$ with Ag grain. Owing to the difference in the in-plane crystallographic symmetries for the Heusler alloy and Ag, a certain amount of lattice mismatch exists at the Heusler/Ag interface for polycrystalline films despite the misfit compensation by the grain boundaries. Such undesirable lattice mismatch may cause poor band matching at the interface. Note that the OR between the Heusler layer and the Ag layer in the CPP-PSVs grown on (001) MgO substrates is different from those of the naturally grown polycrystalline PSVs; *i.e.*, the former has [001](100)$_{Heusler}$//[001](110)$_{Ag}$ interface with a lattice misfit smaller than 3% while the latter has [011](100)$_{Heusler}$//[111](1$\bar{1}$0)$_{Ag}$ interface with a lattice misfit larger than 7%. Hence, if the <001> textured polycrystalline multilayer is attained, the above-mentioned interfacial mismatch could be reduced following the rotation epitaxy-like relationship in epitaxial PSVs and higher MR output may be attained. Therefore, in this work, we fabricated <001> textured polycrystalline CPP-PSVs using the Co$_2$Fe(Ga$_{0.5}$Ge$_{0.5}$) (hereafter denoted as CFGG) Heusler layers and a Ag spacer layer.

4.2 <001> textured pseudo spin valves induced by MgO buffer layer

4.2.1 Thin film structural optimization and magnetic property

In 2008, Wang *et al*[43] reported large TMR in $Co_2Fe(Al_{0.5}Si_{0.5})$/MgO/$Co_2Fe(Al_{0.5}Si_{0.5})$ magnetic tunnel junctions (MTJs) prepared on thermally oxidized Si substrates. They used the MgO buffer layer to obtain highly [001]-oriented thin film growth. In this study, we deposited MgO/Cr/Ag tri-layer as buffer layer on Si/SiO_2 substrates for our CPP-GMR study. After the optimization of the substrate treatment and sputtering condition, we obtain a <001> textured buffer layer MgO(10)/Cr(20)/Ag(50) (thickness in nm) with relatively smooth surface as shown in **Fig. 4-1**. The reason to acquire smoothness of the buffer layer is to reduce physical defects like pinholes and to prevent the onset of orange peel coupling which may induce undesirable metastable magnetization states during the parallel $\Leftrightarrow$ antiparallel switching process. Note that although the <001> texture has been attained, some mis-oriented Ag grains exist indicated by the observation of Ag (111) diffraction peak.
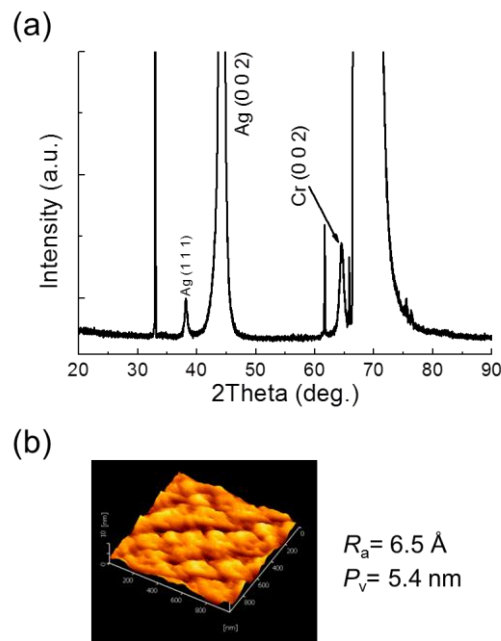

Fig. 4-1 (a) XRD profiles and (b) surface morphology for the optimized buffer layer MgO(10)/Cr(20)/Ag(50) deposited on Si/SiO_2 substrate.

Fig. 4-2 shows the *θ-2θ* XRD profiles for the multilayer stack of Si/SiO$_2$/MgO(10)/Cr(20)/Ag(50)/CFGG(10)/Ag(5)/Ru(4) as-deposited and *ex-situ* annealed at 400°C. All the Cr, Ag and CFGG layers show (002) diffraction peaks which indicate that the <001> fiber texture is induced by the deposition of the MgO buffer layer. The CFGG (002) superlattice peak suggests B2 order of the CFGG Heusler alloy layer. Though the relatively low CFGG (002) diffraction intensity may indicate a low degree of B2 order.
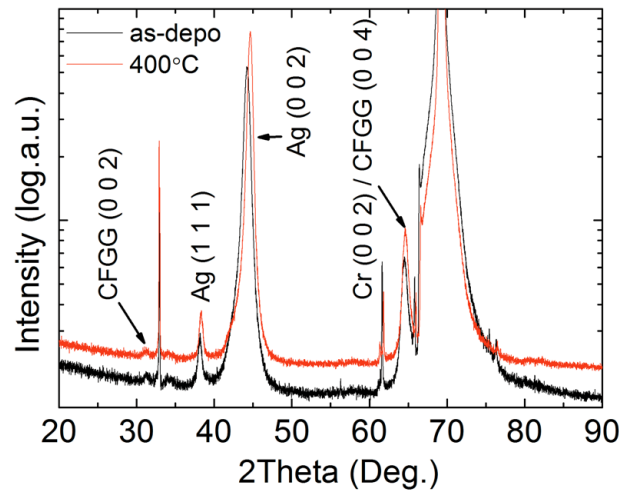

Fig. 4-2 XRD profile of thin film stack of Si/SiO$_2$//MgO(10)/Cr(20)/Ag(50)/CFGG(20)/Ag(5)/Ru(4) in the as-deposited state (black) and annealed at 400°C (red).

Fig. 4-3 exhibits the magnetic hysteresis loops of the Si/SiO$_2$/MgO(10)/Cr(20)/Ag(50)/CFGG(10)/Ag(5)/Ru(4) film stack annealed at different temperatures. All the films annealed below 400°C demonstrate soft magnetic properties while the film annealed at 500°C have relatively large coercivity and a lower magnetization. **Fig. 4-3** (b) summarizes the average saturation magnetization (M_s) and coercivity (H_c) of 20 nm CFGG film as a function of annealing temperature. The M_s reaches maximum at 400°C and decreases at higher temperature. On the other hand, there is an abrupt increase for H_c at 500°C. One possible explanation is the grain growth or recrystallization of polycrystalline CFGG/Ag layers induced by the high temperature annealing.[44] The decrease of M_s at 500°C suggests inter-diffusion of nonmagnetic elements across the CFGG/Ag interface. From **Fig. 4-3** (b), the optimal annealing temperature for CPP-GMR should be around 400°C, where the M_s is the highest while the H_c is relatively low.
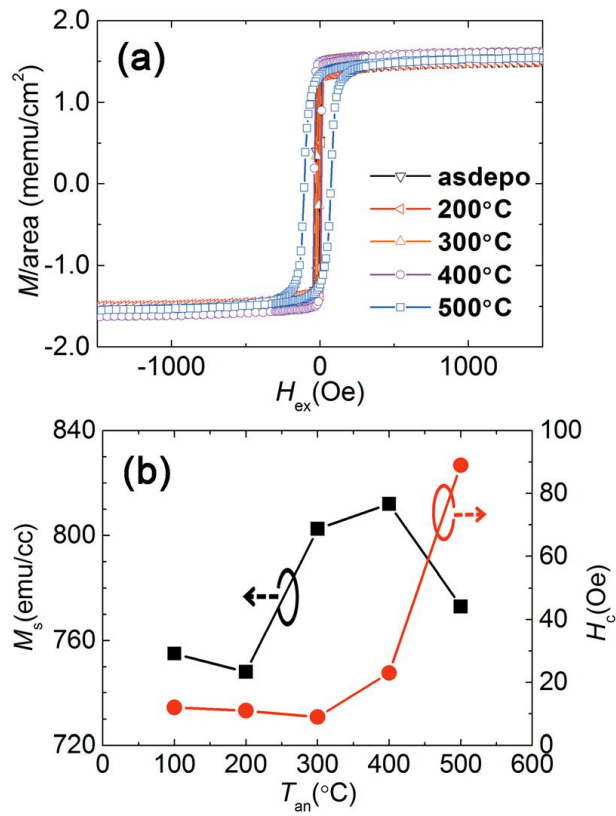
Fig. 4-3 (a) Magnetization curves of Si/SiO$_2$//MgO(10)/Cr(20)/Ag(50)/CFGG(20)/Ag(5)/Ru(4) annealed at different temperatures, (b) temperature dependence of average saturation magnetization (M_s) and coercivity (H_c).

4.2.2 Magneto-transport properties and microstructure

Fig. 4-4 (a) and (b) shows the typical MR curves of the PSVs *ex-situ* and *in-situ* annealed at 400°C with the film structure of Si/SiO$_2$//MgO(10)/Cr(20)/Ag(50)/CFGG(20)/Ag(5)/Ru(8). The MR ratio of the *ex-situ* annealed device is 16% with ΔRA reaching 4.6 mΩ μm^2, which is further enhanced to 5.8 mΩ μm^2 by *in-situ* annealing (the directly measured device resistance change (ΔR) and evaluated CPP-GMR pillar area (A) are 0.39 and 0.44 Ω, 0.0118 and 0.0131 μm^2 for *ex-situ* annealed (**Fig. 4-4** (a)) and *in-situ* annealed (**Fig. 4-4** (b)) PSV devices, respectively). This value is 30-40% larger than the maximum value reported by Carey *et al.*[40] and Nakatani *et al.*[41], and is the highest ΔRA output ever reported in polycrystalline PSVs or exchange-biased spin-valves. Note that the anti-parallel magnetization region of the curve in **Fig. 4-4** (b) shows step-like resistance behavior, which is possibly originated from the interlayer roughness of the sputter-deposited thin films as seen from the HAADF-STEM images of the *ex-situ* and *in-situ* annealed samples in **Fig. 4-5**. Better magnetization switching with stable parallel and antiparallel states is expected to appear if the roughness of the films can be reduced. The EDS elemental mapping of Ga and Ge in the *ex-situ* annealed sample (**Fig. 4-5** (a)) shows that there is obvious diffusion of atoms near the upper interface of the top CFGG layer into the Ag/Ru capping layer, while no apparent diffusion of Ga and Ge atoms occurs in the *in-situ* annealed sample as shown in **Fig. 4-5** (b). One possible reason for the Ga and Ge atoms migration in **Fig. 4-5** (a) is that the high interfacial energy at the Ag/Ru interface could be relieved by Ga and Ge accumulation near the incoherent Ag/Ru interface, similar to earlier reports by Li *et al.*[29] The prevention of atomic diffusion for the *in-situ* annealed film results in CFGG composition closer to the stoichiometric composition of Co$_2$Fe(Ga$_{0.5}$Ge$_{0.5}$), which may give rise to higher bulk spin polarization in the upper CFGG layer and account for the increased ΔRA in the *in-situ* annealed PSV compared to the *ex-situ* annealed PSV at 400°C. Although there is a possible effect of device-size uncertainty propagating to an RA- and ΔRA- value uncertainty, the ΔRA difference demonstrated in **Fig. 4-4** (a) and (b) for the *ex-situ* and *in-situ* annealed PSVs should derive mainly from the alteration of annealing procedure based on the discussion above.
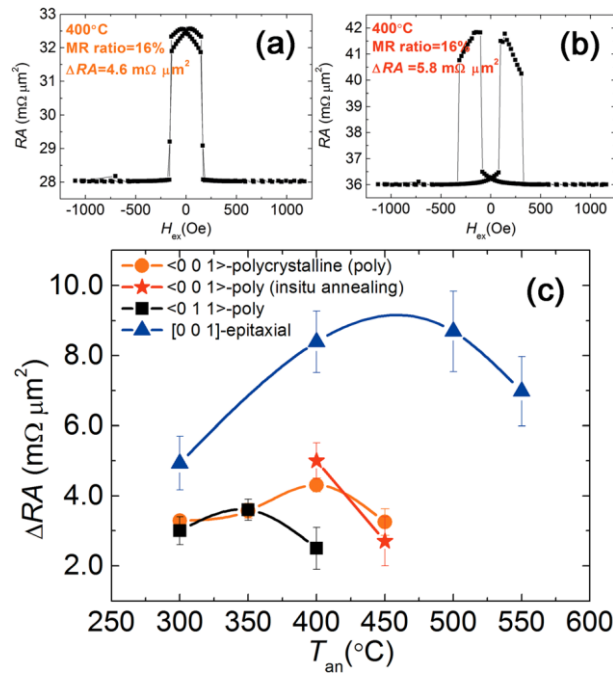
Fig. 4-4 MR curves for <001> textured PSVs (a) *ex-situ* annealed and (b) *in-situ* annealed at 400°C. (c) annealing temperature dependence of ΔRA for PSVs with <001> textured (circles and stars) and <011> textured (squares) CFGG. The epitaxial results (triangles) are taken from Ref. [29] and the <011> textured results (squares) are from Ref. [41].
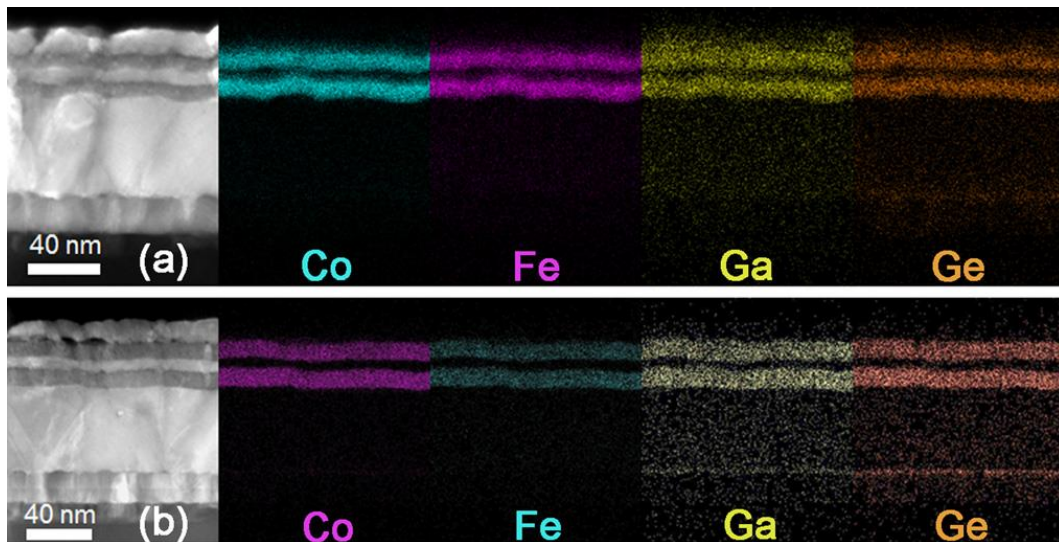

Fig. 4-5 HAADF-STEM and EDS images of (a) *ex-situ* annealed and (b) *in-situ* annealed thin films at 400°C.

4.2.3 Discussion

The MR outputs (ΔRA) for the <001> textured (circles and stars) and <011> textured[41] (squares) polycrystalline CFGG/Ag/CFGG PSVs are shown as a function of annealing temperature in **Fig. 4-4** (c). The results of epitaxial CFGG/Ag/CFGG PSVs (triangles) with the crystallographic orientation of [001] are also shown for comparison.[29] For the *ex-situ* annealed <011> and <001> textured PSVs (squares and circles in **Fig. 4-4** (c)), there is no noticeable difference in ΔRA up to T_{an}=350°C. While the ΔRA value of the <011> textured PSV decreases by annealing at T_{an}=400°C, the ΔRA of the <001> textured PSV shows the maximum value at the same temperature. This contrary ΔRA behavior in the temperature region of 350°C-400°C for these two textures indicates that the PSVs with <001> textured CFGG layer possess higher thermal stability than the PSVs with <011> textured CFGG layer. This can be explained from the smaller mismatch for the <001> textured films at the $[001](100)_{Heusler}//[001](110)_{Ag}$ interface compared to that at the $[011](100)_{Heusler}//[111](1\bar{1}0)_{Ag}$ interface.[41] The smaller lattice mismatch can lead to reduced interfacial energy at the CFGG/Ag interface that enables higher device thermal endurance against the delamination of the multilayer structure.[29,41,42]

This work presents direct experimental observation of the orientation dependence of MR output in CPP-GMR. As for the most probable reason for the orientation dependence of MR, we speculate that the interfacial spin asymmetry, γ, may differ depending on the crystallographic orientations at the CFGG/Ag interface. According to the Valet-Fert (V-F) model,[11] ΔRA can be estimated by $\Delta RA \sim 2\frac{\beta^2}{1-\beta^2}\rho_F t_F + 2\frac{\gamma^2}{1-\gamma^2}AR_{F/N}$, in which β, ρ_F and t_F are the bulk spin asymmetry, resistivity and thickness of the CFGG layer, and $AR_{F/N}$ is the interfacial resistance at the CFGG/Ag interface. Since β does not depend on the interfacial structure, the difference in ΔRA for these two textures may be explained by the orientation dependence of γ. However, the ΔRA (squares and circles in **Fig. 4-4** (c)) up to 350°C does not show much difference depending on the crystallographic textures. This is probably owing to the low β value of CFGG stemming from the low degree of B2 order. According to the annealing temperature dependence of the CFGG/Ag/CFGG [001] epitaxial PSV, high ΔRA value exceeding 8 mΩ μm^2 appears only in the sample annealed above 400°C.[5] Since the degree of L2$_1$ order is low for T_{an}<400°C, both β and γ would be low, which leads to no orientation dependence of γ or the band matching at the CFGG/Ag interface. In order to fully understand the origin of the orientation dependence of γ, the MR properties of CFGG[011]/Ag[111]/CFGG[011] epitaxial PSVs need to be investigated. In addition, theoretical work on the band matching for these two orientations will be intriguing.

Note that the ΔRA at optimal annealing temperature of 400°C for the <001> textured PSV is about 40% lower than that for the [001] epitaxial PSV, even though they have the same crystallographic orientation. There is no clear explanation for the discrepancy of ΔRA between the polycrystalline and epitaxial PSVs. One possible reason is the existence of grain boundaries in the polycrystalline films, which may cause a spin-independent electron scattering channel when electrons are traveling along them in polycrystalline PSVs.

Fig. 4-6 shows the low temperature magneto-transport result of the device demonstrated in **Fig. 4-4** (b). **Fig. 4-6** (a) shows that the MR ratio and ΔRA of the individual device increased from 12% and 5.9 $m\Omega\ \mu m^2$ at 300 K to 24% and 10.8 $m\Omega\ \mu m^2$ at 4.2 K, respectively. The ×1.8 increase in the ΔRA is mainly originated from an enhancement of the bulk spin polarization of CFGG by the suppression of phonons. Interestingly, for the epitaxial PSVs with the tri-layer of CFGG/Ag/CFGG annealed at the same temperature, the $\Delta RA_{4.2\ K}/\Delta RA_{300\ K}$ slightly increases to ~2.5. The possible explanations are 1) the CFGG chemical ordering for the polycrystalline film is slightly lower than that of the epitaxial films and 2) the physical defects in the polycrystalline films such as the grain boundaries act as spin-independent scattering source that decreases the bulk or interfacial scattering asymmetries at low temperature. The resistance-area product of the anti-parallel state ($R_{ap}A$), parallel state ($R_{p}A$) and ΔRA was also shown as a function of measuring temperature in **Fig. 4-6** (b). The nearly monotonic decrease (increase) in the ΔRA and $R_{p}A$ is similar to that of the epitaxial CFGG/Ag/CFGG PSVs.
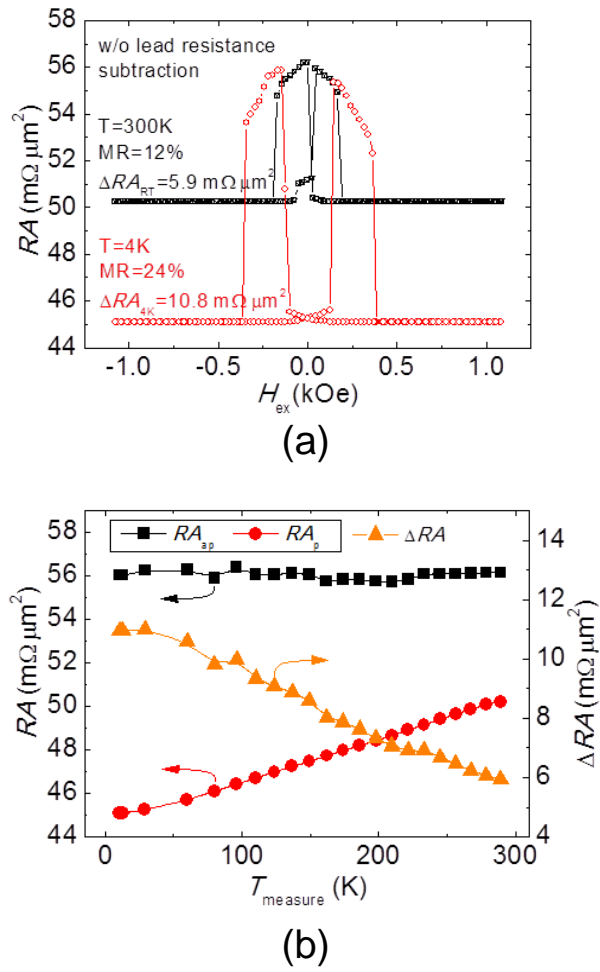
Fig. 4-6 (a) MR curves of the device in **Fig. 4-4** (b) measured at 4.2 K(red) and 300 K (black). (b) measuring temperature dependence of ΔRA and resistance-area product of the device in anti-parallel state ($R_{ap}A$), parallel state (R_pA).

4.2.4 Summary

In summary, polycrystalline PSV devices with multilayered <001> texture, which was induced by <001> textured MgO underlayer, were fabricated by using CFGG FM layers and a Ag spacer on thermally oxidized Si substrates. The optimally annealed <001> textured PSV exhibited ΔRA of ~6 mΩ μm^2 and MR ratio of 16%. This value is one of the highest MR output among polycrystalline CPP PSVs or SVs reported so far. The PSV with the <001> textured CFGG films outperform the one with the <011> texture, possibly because of the reduction in lattice mismatch or improved band matching at the CFGG/Ag interface. The RA value for the polycrystalline device was 36 mΩ μm^2, which is ~50% larger than the typical value reported for [001] epitaxial device, closer to the supposedly optimal value of approximately 100 mΩ μm^2. This work has also shown the possibility of orientation dependence of the interfacial spin scattering asymmetries in CPP-GMR.

4.3 <001> textured pseudo spin valves induced by Mg-Ti-O buffer layer

The result shown in **section 4.2** on <001> textured polycrystalline CPP-GMR using a MgO buffer layer explicitly showed the advantage of using <001> textured Heusler FM layer in PSV devices with a Ag spacer over that with <011> textured FM layer. However, the <001> textured devices grown on <001> textured MgO underlayer is not industrially viable because MgO, as an insulator, cannot be used for the fabrication of the actual CPP-GMR sensors that must be grown on conductive substrates. In addition, the demonstrated <001> textured polycrystalline devices had very rough interfaces because of the need of a thick Ag electrode on an insulating MgO underlayer. Thus, obtaining <001> textured CPP-GMR devices with conductive buffer layer becomes necessary. Varaprasad *et al*[45] reported strong <001> texture growth of conductive rock-salt-type $(Mg_{0.2}Ti_{0.8})O$ thin films on <001> textured Cr buffer layer, which suggests the possibility of using conductive $(Mg_{1-x}Ti_x)O$ to induce the <001> texture in CPP-GMR devices. In this work, we report the CPP-GMR devices with <001> textured $Co_2Fe(Ga_{0.5}Ge_{0.5})$ (CFGG) Heusler alloy layers grown on conductive $(Mg_{0.5}Ti_{0.5})O$ (MTO hereafter in this chapter, note that the composition of MTO in this chapter is different from that in Chapter 6) buffer layer. By depositing the MTO layer upon amorphous buffer layer such as NiTa (*a*-NiTa), we are able to obtain a <001> texture in the MTO nano-layer, consequently resulting in the <001> texture in Cr or CFGG layers deposited upon.

4.3.1 Optimization of the underlayer

In order to obtain a <001> texture, proper buffer layer is needed. **Fig. 4-7** shows the XRD profile for multilayer thin film stacks of 1) Si/SiO$_2$//*UL*/CFGG(20)/Ru(2), 2) Si/SiO$_2$//*UL*/Cr(10)/CFGG(20)/Ru(2), 3) Si/SiO$_2$//*UL*/Cr(10)/CoFe(2)/CFGG(20)/Ru(2) (*UL* = *a*-NiTa(10)/MTO(2)). Peaks marked with asterisks are coming from the Si/SiO$_2$ substrate. CFGG (002) diffraction peaks were detected for the films with Cr and Cr/CoFe insertion, while no observable (002) or even (004) diffraction signal was obtained for the film directly deposited on the *a*-NiTa/MTO buffer layers. This suggests that the CFGG layer grown on MTO is nano-crystalline or amorphous. Note that for all three sets of samples there is a weak and broad peak around 45°, which is probably coming from the mis-oriented CFGG grains, e.g. CFGG (220). The insertion of Cr or Cr/CoFe dramatically contributes to the formation of the <001> texture.

Owing to the fact that the <001> texture in this study is induced by the buffer layer, its thickness dependence of the texture was also examined. **Fig. 4-8** shows the XRD profile for the multilayer of NiTa(10)/MTO(t_U)/Cr(20) (t_U =1, 2, 5 nm) deposited on industrially available substrate of Si/SiO$_2$//Ta(5)/Cu(250)/Ta(30), which has smooth surface. Note that the reason we need the thick Cu underlayer is aiming to attain homogeneous current distributions in CPP-GMR pillars. For the MTO thickness of 2 and 5 nm. Cr (002) is observed indicating a <001> texture. When MTO thickness decreases to 1 nm, however, the Cr (002) disappears. One possible reason is that the first few MTO monolayers deposited on amorphous NiTa is nano-crystalline or amorphous. Therefore the thickness of the MTO is at least 2 nm (roughly) in order to induce a strong <001> texture. Consequently, in this work we use the buffer layer of *a*-NiTa(10)/MTO(2)/Cr(10)/CoFe(2) in the CPP-GMR studies, the insertion of CoFe nano-layer aims to prevent the Cr atoms from diffusing into the bottom CFGG layer, as proved in our earlier studies.
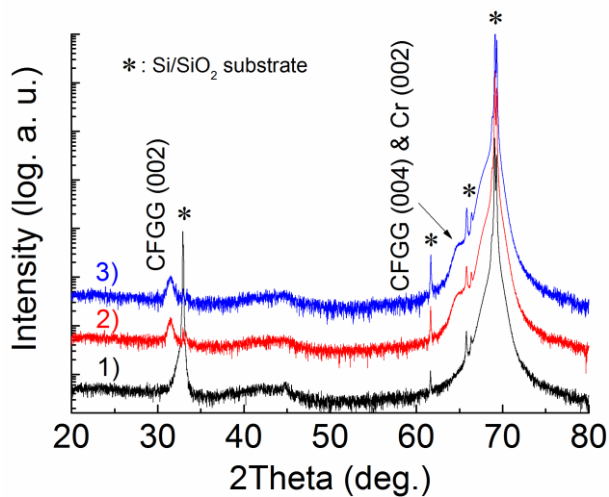
Fig. 4-7 XRD profile for as-deposited thin film stack of 1) Si/SiO$_2$//UL/CFGG(20)/Ru(2), 2) Si/SiO$_2$//UL/Cr(10)/CFGG(20)/Ru(2), and 3) Si/SiO$_2$//UL/Cr(10)/CoFe(2)/CFGG(20)/Ru(2), where UL= a-NiTa(10)/MTO(2).
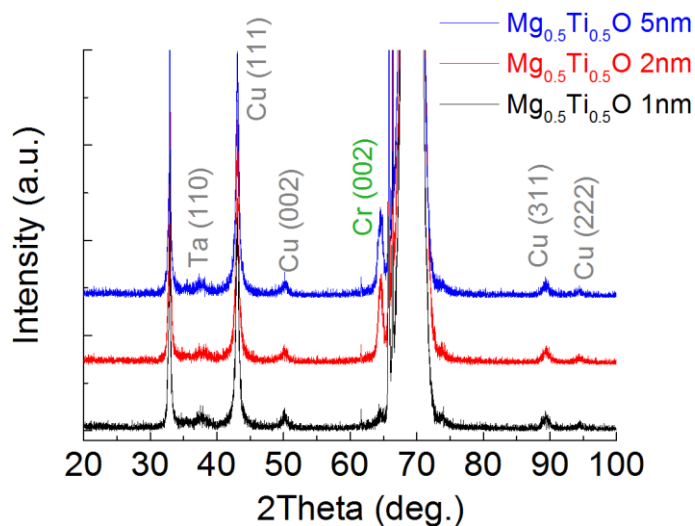

Fig. 4-8 XRD profile of as-deposited film Si/SiO$_2$//Ta(5)/Cu(250)/Ta(30)/NiTa(10)/MTO(t_U)/Cr(20), where t_U =1, 2, 5 nm.

4.3.2 Magneto-transport properties

Fig. 4-9 shows the annealing temperature (T_{an1}) dependence of ΔRA for CPP-GMR PSV devices of Si/a-SiO$_2$//Ta/Cu(250)/Ta//a-NiTa(10)/MTO(2)/Cr(10)/CoFe(2)/CFGG(5)/Ag(7)/CFGG(5)/T_{an1}/Ag(5)/Ru(8), where T_{an1} denotes the annealing at the stage inside the chamber after the top CFGG layer was deposited. The inset of **Fig. 4-9** shows the typical R-H curve for the device annealed at 375°C, with ΔRA of 4.9 mΩ μm^2. Note that the RA_{para} is 240.5 mΩ μm^2, which is 5 to 6 times higher than that of previously reported <001> textured CFGG/Ag/CFGG devices.[46] The relatively small MR ratio despite moderate ΔRA is due to the large background resistance coming from the high resistive NiTa and MTO (> 300 μΩ cm) layers. The optimal annealing temperature between 375°C and 400°C is consistent with our previous results on the PSVs with <001> textured CFGG/Ag/CFGG PSV, but this thermal stability against annealing is still better than those with the <011> textured PSVs.[46]

We also investigated the MR output by performing an additional post-annealing process for the bottom CFGG layer. **Fig. 4-10** shows the ΔRA as a function of annealing temperature (T_{an2}) for the PSVs with 2-annealing process with the stacking structure of Si/SiO$_2$//Ta/Cu(250)/Ta//a-NiTa(10)/MTO(2)/Cr(10)/CoFe(2)/CFGG(5)/T_{an2}/Ag(7)/CFGG(5)/T_{an1}/Ag(5)/Ru(8), where T_{an1}=375°C. The ΔRA reaches maxima of 5.8 mΩ μm^2 at T_{an2}=400°C. The inset shows the typical R-H curve for optimally annealed device. The slight increase in ΔRA compared to the maximum value in **Fig. 4-9** is possibly due to the increase in the degree of B2 order of the bottom CFGG layer. The drop of ΔRA at higher annealing temperature is probably attributed to the inter-diffusion between the bottom CFGG layer and the buffer layer of Cr.
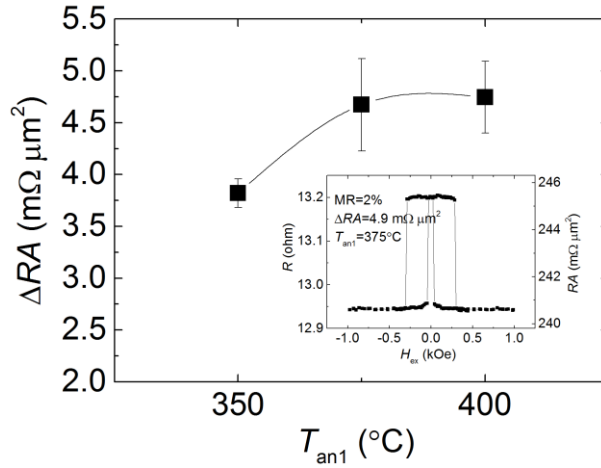
Fig. 4-9 Annealing temperature dependence of ΔRA for PSV devices of Si/SiO$_2$//Ta(10)/Cu(250)/Ta(30)//NiTa(10)/MTO(2)/Cr(10)/CoFe(2)/CFGG(5)/Ag(7)/CFGG(5)/T_{an1}/Ag(5)/Ru(8). Inset is the typical MR curve with T_{an1}=375ºC.
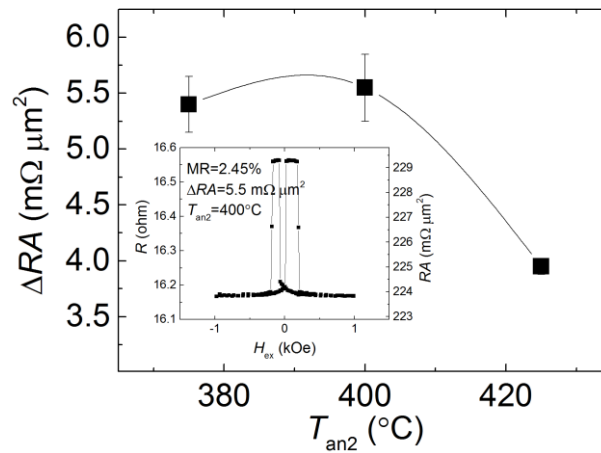

Fig. 4-10 ΔRA of PSVs as a function of T_{an2} with 2-annealing process with the stacking structure of Si/SiO$_2$//Ta(10)/Cu(250)/Ta(30)//NiTa(10)/MTO(2)/Cr(10)/CoFe(2)/CFGG(5)/T_{an2}/Ag(7)/CFGG(5)/T_{an1}/Ag(5)/Ru(8), where T_{an1}=375ºC. Inset is the MR curve with T_{an2}=400ºC.
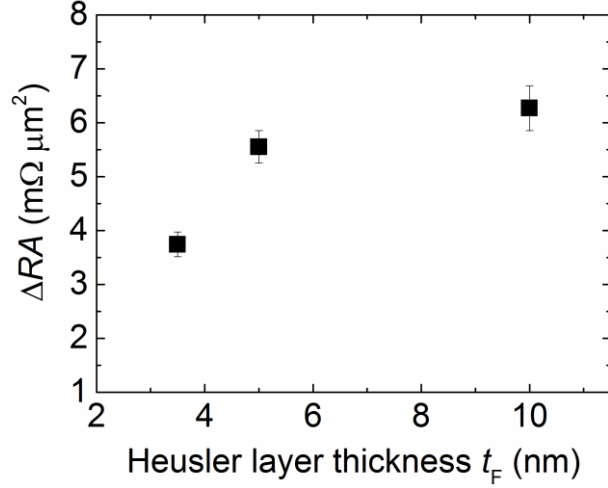
Fig. 4-11 ΔRA as a function of Heusler layer thickness for PSV devices of Si/SiO$_2$//Ta(10)/Cu(250)/Ta(30)//NiTa(10)/MTO(2)/Cr(10)/CoFe(2)/CFGG(t_F)/T_{an2}/Ag(7)/CFGG(t_F)/T_{an1}/Ag(5)/Ru(8), where T_{an1}=375°C and T_{an2}=400°C.

Fig. 4-11 shows ΔRA as a function of CFGG layer thickness for optimally annealed PSV devices of Si/SiO$_2$//Ta/Cu(250)/Ta//a-NiTa(10)/MTO(2)/Cr(10)/CoFe(2)/CFGG(t_F)/T_{an2}/Ag(7)/CFGG(t_F)/T_{an1}/Ag(5)/Ru(8), where T_{an1}=375°C and T_{an2}=400°C, respectively. The CPP-GMR device with 10 nm CFGG show the maximum ΔRA of 6.6 mΩ μm^2, which is more than 10% higher than that with 5 nm CFGG layer, and further reduction of the CFGG thickness to 3 nm results in substantial decrease of ΔRA. Similar ΔRA behavior was observed in the PSVs with <011> textured FM CFGG layers. Lower degree of B2 ordering in thinner CFGG layers could be the reason for such ΔRA reduction.[41]

4.3.3 Microstructure

Fig. 4-12 shows the HAADF-STEM image and EDS mapping for the CPP-GMR multilayer film stack of Si/SiO$_2$//Ta/Cu(250)/Ta//a-NiTa(10)/MTO(2)/Cr(10)/CoFe(2)/CFGG(5)/T_{an2}/Ag(7)/CFGG(5)/T_{an1}/Ag(5)/Ru(8), where T_{an1}=375ºC and T_{an2}=400ºC. Relatively flat interfaces are observed up to the top CFGG layer. AFM measurement confirmed the interfacial flatness, *i.e.*, the average roughness of the bottom CFGG layer is only 0.2 nm, which is much smaller than the roughness in MgO-based <001> textured CPP-GMR multilayer stacks (~0.6 nm). Since MgO underlayer is insulating, a thick (~50 nm) Ag electrode layer had to be deposited below the CFGG FM layer in our previous reported <001> textured devices,[46] and this thick Ag layer caused surface roughness during the growth. On the other hand, no thick Ag electrode layer was needed for the MTO underlayer, as it is electrically conductive. Little elemental diffusion was seen for Co, Fe, Ga and Ge, and continuous Ag spacer excludes the existence of pinholes that will exert undesirable exchange couplings for the two FM layers through the Ag spacer.
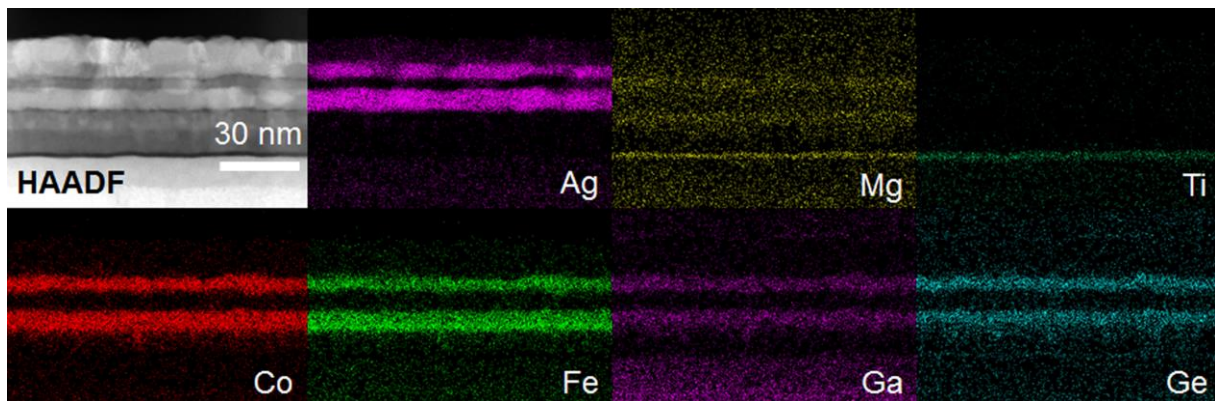

Fig. 4-12 HAADF-STEM image and EDS mappings of elements for the optimally annealed PSV multilayer of Si/SiO$_2$//Ta(10)/Cu(250)/Ta(30)//NiTa(10)/MTO(2)/Cr(10)/CoFe(2)/CFGG(5)/T_{an2}/Ag(7)/CFGG(5)/T_{an1}/Ag(5)/Ru(8), where T_{an1}=375ºC and T_{an2}=400ºC.

4.3.4 Summary

Fig. 4-13 shows the comparison of MR output for polycrystalline PSVs using 10 nm CFGG with <001> texture induced by MgO and MTO. For comparison, ΔRA of the epitaxial CFGG/Ag/CFGG PSV is shown. The merit of using MTO buffer layer in <001> textured PSVs is not only the favorable interfacial smoothness shown in Fig. 5, but also the slightly higher ΔRA value compared to the MgO-based <001> textured PSVs.[46] Such increase is probably owing to the enhanced chemical ordering for the bottom CFGG layer with the additional annealing. Moreover, such conductive MTO buffer layer could possibly be applied to the read head fabrication process with device resistance several orders of magnitudes smaller compared to that of MTJs.[14]

Despite the advantages mentioned above, there is a drawback for the polycrystalline CPP-GMR devices using such MTO buffer layer, *i.e.*, the background resistance is too high. Such high resistance originates from the high resistive *a*-NiTa layer and MTO layer. One possible way to tackle with this problem is to increase the Ti composition in the MTO buffer layer, so that the resistivity of MTO will decrease dramatically while maintaining the <001> texture. Moreover, buffer layers are known to dramatically influence the chemical ordering of the Heusler layers deposited upon, and different interfacial conditions affect the grain growth orientations as well as the dead layer thickness in Heusler layers.[47] Brinkman *et al.*[48] reported considerable improvement in the crystalline quality in Co_2MnGe Heusler thin films by using a non-crystalline buffer layer CoFeBTa, which substantially increases the chemical ordering of Co_2MnGe upon annealing. Such ordering enhancement is expected to effectively increase the CPP-GMR output.
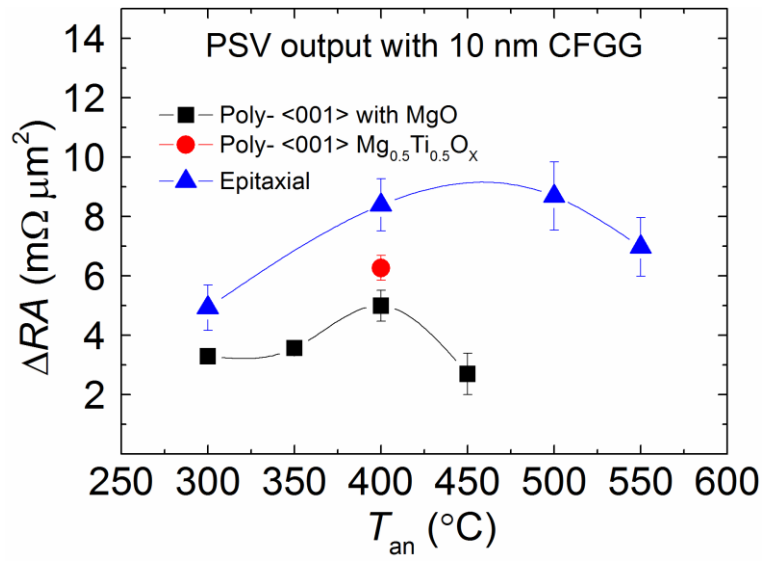
Fig. 4-13 Comparison of polycrystalline PSVs with <001> textured CFGG using MgO buffer (square) and MTO buffer (sphere), epitaxial result (triangle) is also shown for comparison.

4.4　Summary of the chapter

As a start, we fabricated polycrystalline PSV devices with MgO-induced multilayer <001> texture on thermally oxidized Si substrates using CFGG ferromagnetic layers and a Ag spacer. The optimally annealed <001> textured PSV exhibited ΔRA of ~ 6 mΩ μm^2 and MR ratio of 16%, which was one of the highest MR output among polycrystalline CPP PSVs or SVs reported. The PSV with the <001> textured CFGG films outperforms the one with the <011> texture, possibly because of the reduction in lattice mismatch at the CFGG/Ag interface. The work has also shown the possibility of orientation dependence of the interfacial spin scattering asymmetry γ in CPP-GMR. However, no clear orientation dependence of γ was observed for the region of $T_{an} < 350°C$, which we speculate is due to the low chemical ordering of CFGG layer.

Secondly, in consideration of practical limitations, MgO as an insulator cannot be used for the fabrication of actual CPP-GMR sensors which must be grown on conductive buffer layers. Therefore, we investigated the CPP-GMR properties and microstructure of PSV devices with <001> textured FM Heusler layer CFGG and conductive buffer layer MTO. By using the multilayer of *a*-NiTa(10)/MTO(2)/Cr(10)/CoFe(2) as the underlayer beneath CFGG we obtained observable B2 ordering of the Heusler electrode. PSVs with 10 nm CFGG and 2 nm MTO layers demonstrate average ΔRA of 6.4 mΩ μm^2 with Ag as the spacer layer. HAADF-STEM and EDS results revealed interfacial smoothness up to the top CFGG layer. Relatively large MR output and desirable interfacial smoothness make MTO a promising choice to fabricate <001> textured Heusler alloy based CPP-GMR devices.

Chapter 5   Epitaxial pseudo spin-valves with Co$_2$Fe(Ga$_{0.5}$Ge$_{0.5}$) Heusler alloy and Cu-Cr-Al alloy spacer

5.1 Introduction

In searching for novel spacer materials which are expected to have large interfacial scattering asymmetry at the FM/NM interface, one type of "all-Heusler" system has been proposed and experimentally investigated. Nikolaev *et al.*[33] reported the NM Heusler spacer Rh$_2$CuSn (RCS), which has 7% lattice mismatch with FM Heusler alloy Co$_2$MnGe that they used as an electrode. The MR ratio and ΔRA turned out to be 6.7% and 4 mΩ μm^2. Such moderate MR output is possibly resulted from the favorable band matching of majority spin channels for these two Heusler alloys. Moreover, Ko *et al.*[49] proposed a potential spacer material Cu$_2$CrAl (CCA), which has already been experimentally confirmed to crystallize in L2$_1$ structure for the bulk alloy. Using *ab initio* calculations, they found a good majority spin matching while very dissimilar minority density of states at the Co$_2$CrZ/CCA (Z=Al, Si) interface, which indicates large spin dependent scattering for these interfaces. Therefore, it might be worth trying to investigate the CPP-GMR properties using the combination of Co-based FM Heusler electrode and NM Heusler spacer CCA. In this work we chose a well-established, highly spin-polarized Heusler alloy Co$_2$Fe(Ga$_{0.5}$Ge$_{0.5}$)[24,29] as the thin film FM layer and CCA as the spacer layer for a CPP-GMR study.

5.2 Structural characterization

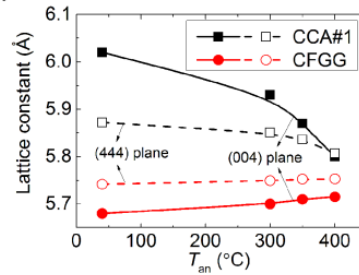**Fig. 5-1** (a) shows the θ-2θ XRD profile of MgO//Cr(10)/Ag(100)/CFGG(15)/CCA(20)/Ag(5)/Ru(8) film stacks as-deposited and annealed from 300°C to 400°C, where CCA has a Cr-lean and Al-slightly-rich composition of $Cu_2Cr_{0.72}Al_{1.05}$. CFGG (002) and (004) peaks are observed for all the films indicating the presence of B2 ordering. CCA (002) peak, however, appears only for the annealed thin films, which suggests that the as-deposited CCA film shows disordered A2 phase or even amorphous phase. **Fig. 5-1** (b) demonstrates the annealing temperature (T_{an}) dependence of integral ratio I_{002}/I_{004}, which is theoretically proportional to the square of the degree of B2 ordering, for the CCA (square) and CFGG (circle) layers, after the measured (002) and (004) peaks were processed by Lorentz fitting. For CCA films the B2 ordering experiences maximum values at approximately 350°C while the ordering of CFGG seems to increase rapidly after 350°C. Note that the 2θ position of CCA (002) and CCA (004) peaks in **Fig. 5-1** (a) shifts to higher angles when T_{an} increases. **Fig. 5-1** (c) shows the T_{an} dependence of out-of-plane (OP) lattice constant derived from CCA and CFGG (004) peak (solid line) and (444) peak (dash line). The OP lattice shrinks for CCA and expands for CFGG, indicating that both the CCA and CFGG layers may have tetragonal distortion in the as-deposited films. To further probe into the chemical ordering of CFGG and CCA, θ-2θ scan of CFGG {111} plane was performed as shown in **Fig. 5-2**. From **Fig. 5-2** (a) the CCA (111) peak suggesting $L2_1$ ordering appears at above 300°C, and epitaxial relationship is confirmed in **Fig. 5-2** (b) by performing the φ scan for the CCA layer. The XRD result suggested that although the as-deposited CCA Heusler film exhibits disordered A2 phase, it orders to $L2_1$ phase at T_{an} of 300°C. On the other hand, we have also conducted XRD measurement with the same film stack for stoichiometric CCA thin films. However, up to 400°C the CCA thin films with stoichiometric composition shows only disordered A2 phase (data not shown), which demonstrates that the chemical ordering of CCA alloy is strongly composition dependent. Therefore, in this study we have fixed the atomic composition of CCA to Cu:Cr:Al = 2:0.72:1.05 (otherwise noted), with Cr lean and Al slightly rich with regard to its stoichiometric composition for an easier attainment of the $L2_1$ ordering.
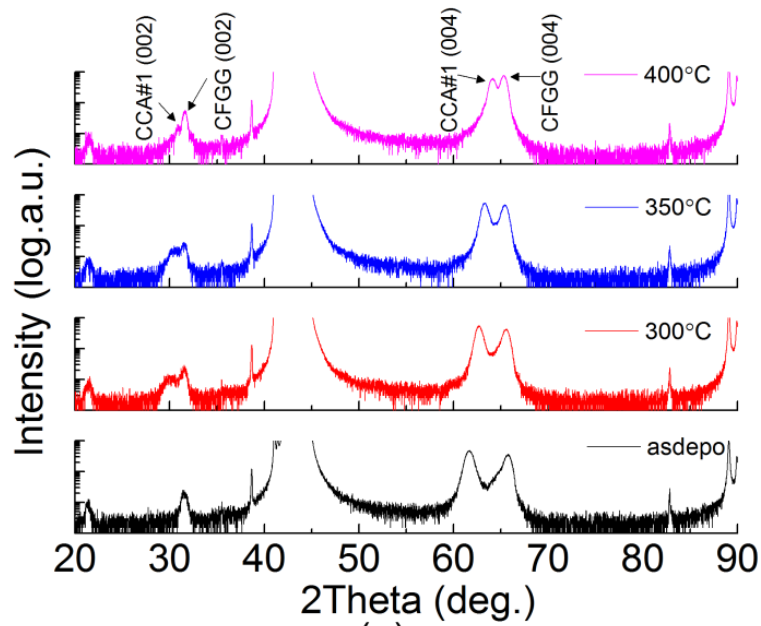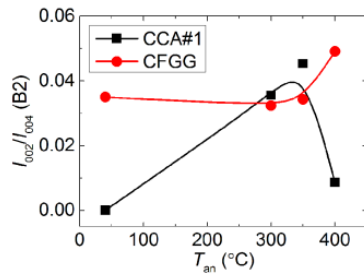
Fig. 5-1 (a) θ-2θ XRD result of MgO sub//Cr(10)/Ag(100)/CFGG(15)/CCA(20)/Ag(5)/Ru(8) film stacks as-deposited and annealed from 300°C to 400°C. (b) Integral intensity ratio of I_{002}/I_{004} and (c) lattice constant estimated from (004) and (444) peak for CFGG (circle) and CCA (square). Note that the CCA has an off-stoichiometric composition of $Cu_2Cr_{0.72}Al_{1.05}$.
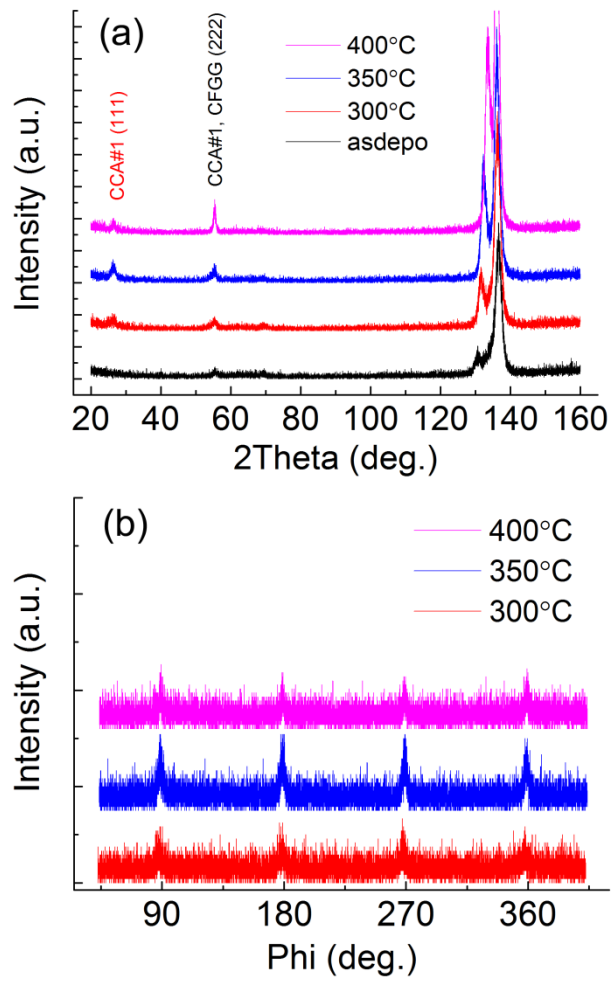
Fig. 5-2 (a) θ-2θ XRD result for the {111} planes of CCA and (b) φ scan for CCA (111) diffraction plane for the film structure of MgO//Cr(10)/Ag(100)/CFGG(15)/CCA(20)/Ag(5)/Ru(8).

5.3 Magneto-transport properties and microstructure

Fig. 5-3 shows the T_{an} dependence of CPP-GMR ratio for the film stack of MgO sub//Cr(10)/Ag(100)/CFGG(10)/CCA(5)/CFGG(10)/Ag(5)/Ru(8). At 300°C, PSV devices with 10 nm CFGG and 5 nm CCA show MR ratio of 5% and ΔRA of 2.4 mΩ μm^2 as shown in the inset of **Fig. 5-3**. Further increasing the annealing temperature attributes to the drop of MR output. **Fig. 5-4** shows the HAADF-STEM image and EDS mapping of the same film stack annealed at 350°C, where slight Al concentration inhomogeneity occurs as seen from the Al mapping. No apparent atomic inter-diffusion or interlayer delamination is observed in other elemental mappings at 350°C. Based on these results, the poor thermal tolerance of the CCA spacer severely limits the CPP-GMR output. For instance, although the chemical ordering of CCA is optimized at T_{an} of 350°C, the optimized T_{an} for the CPP-GMR multilayer is lower (e.g. less than 300°C), which suggests that the structural change induced by annealing such as the inhomogeneity of Al concentration is the possible reason for the MR drop as T_{an} goes above 300°C.
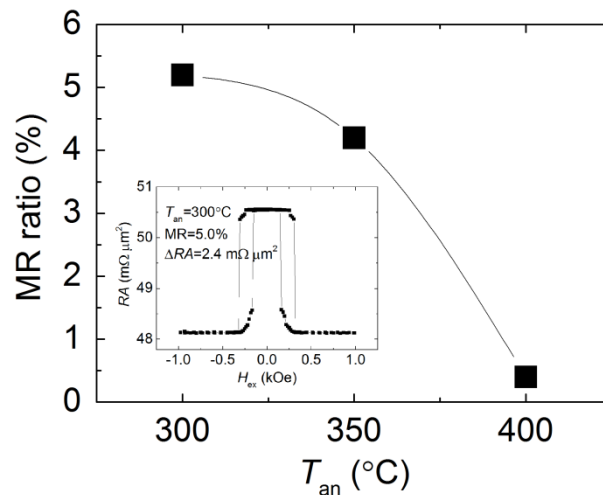

Fig. 5-3 MR ratio as a function of annealing temperature for CPP-GMR stacks of MgO//Cr(10)/Ag(100)/CFGG(10)/CCA(5)/CFGG(10)/Ag(5)/Ru(8). Inset is the MR loop at 300°C.
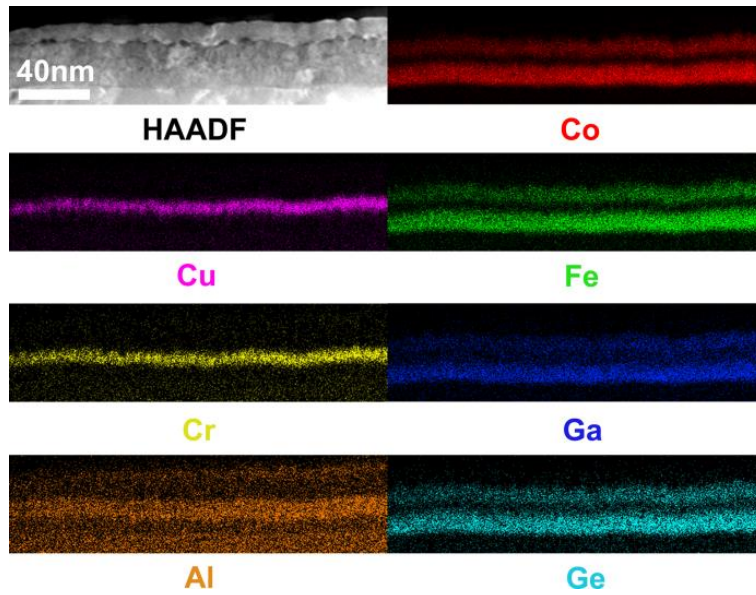
Fig. 5-4 HAADF-STEM image of MgO//Cr(10)/Ag(100)/CFGG(10)/CCA(5)/CFGG(10)/Ag(5)/Ru(8) annealed at 350°C and the elemental mapping of Cu, Cr, Al, Co, Fe, Ga, Ge.

In **Fig. 5-5**, the MR ratio is shown as a function of Cr concentration x (the composition of CCA is shown as Cu_2Cr_xAl) for CPP-GMR devices with the structure of MgO//Cr(10)/Ag(100)/CFGG(10)/Cu_2Cr_xAl(5)/CFGG(10)/Ag(5)/Ru(8) (x=0.72, 0.89 and 1) at optimal annealing temperature of 300°C. It turns out that the MR output dramatically decreases when the CCA composition goes from Cr lean to stoichiometric. Assuming that no phase separation occurs at 300°C, the reason of such MR drop cannot be explained by the structural change like inhomogeneous elemental distribution. Note that Cr is antiferromagnetic at room temperature, we speculate that there would be inevitable *s-d* scattering between the spin polarized current and the local Cr magnetic moment, which could cause spin flipping that decreases the spin polarization when the conduction electrons travel through the CCA spacer. Therefore, one possible explanation for the MR decrease is that as the Cr concentration increases, higher degree of *s-d* scattering between the conduction electrons and magnetic moment of isolated Cr atoms occurs, consequently spin flipping or relaxation enhances in the CCA layer and MR drops correspondingly.
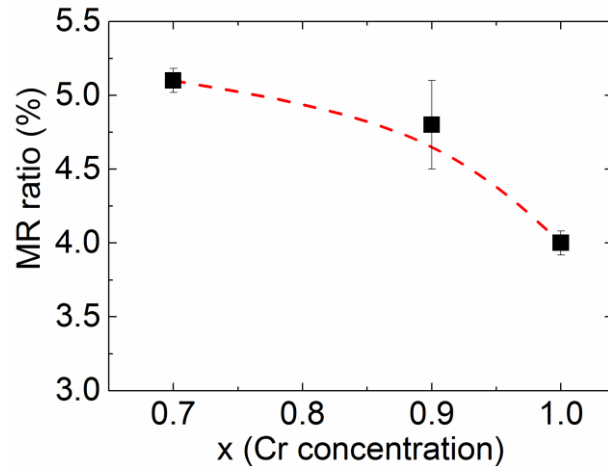
Fig. 5-5 MR ratio as a function of Cr concentration x for CPP-GMR devices of MgO//Cr(10)/Ag(100)/CFGG(10)/Cu$_2$Cr$_x$Al(5)/CFGG(10)/Ag(5)/Ru(8) annealed at 300°C, where x=0.72, 0.89 and 1.

5.4 Summary of the chapter

We reported CPP-GMR devices with the combination of FM Heusler layer CFGG and NM Heusler spacer Cu-Cr-Al (CCA). At 300°C, the CCA thin film with Cr-lean composition of $Cu_2Cr_{0.72}Al_{1.05}$ shows L2$_1$ ordering and the corresponding CPP-GMR device shows maximum MR output; further increasing the T_{an} to 350°C results in reduction of MR ratio due to possible phase separation of Al. We were to expected that the combination of highly spin polarized CFGG layer and L2$_1$ ordered CCA would lead to an increase in the spin dependent interfacial scattering asymmetry at the FM/NM interface. However, the poor thermal tolerance of the CCA spacer severely limits the CPP-GMR output. On the other hand, increasing the Cr concentration in $Cu_2Cr_{0.72}Al$ decreased CPP-GMR, which is possibly caused by the occurrence of higher degree of s-d scattering between the conduction electrons and magnetic moment of isolated Cr atoms. These results suggest that a spacer material containing magnetic element/magnetic moment may not be suitable for the enhancement of CPP-GMR output.

Chapter 6   Large voltage output in CPP-MR devices using

Co$_2$Fe(Ga$_{0.5}$Ge$_{0.5}$) Heusler alloy and Mg-Ti-O spacer

6.1 Introduction

The maximum attainable voltage output ΔV_{max} ($\Delta V_{max} = J_{Bias} \times RA \times MR$) in all-metallic CPP-GMR junctions is severely limited when the CPP current density J_{Bias} is beyond certain threshold values. The MR ratio gradually decreases with increasing J_{Bias} due to the enhanced spin transfer torque (STT) that destabilizes the antiparallel FM magnetizations configuration. One possible solution to tackle with this problem is the usage of high-resistive transparent oxide as the spacer material in the CPP-MR devices that suppresses the STT effect. Very recently, Nakatani *et al.*[50] reported a In-Zn-O spacer material for the CPP-MR studies with a Co$_2$Mn$_{0.6}$Fe$_{0.4}$Ge Heusler compound. By properly engineering the tri-layer spacer Ag/In-Zn-O/Zn, a large ΔV_{max} of 11.3 mV was obtained in the CPP-MR devices with a bias voltage (V_b) of 70 mV. In contrast, using a metallic AgSn spacer with the same Heusler alloy, a much smaller ΔV_{max} of 2.3 mV was obtained with a reduced V_b of 30 mV. A better STT endurance by using the In-Zn-O based spacer material is suggested not only from the enhanced ΔV_{max}, but also from a higher V_b that the CPP-MR device is able to sustain.

The physical mechanism of such MR property enhancement by using a tri-layer spacer is likely to be the occurrence of current-confined-path (CCP) effect,[51] in which the Ag or Zn may form a metallic nano-pillar path through the semiconducting In-Zn-O layer that carries the confined current, thus the spin dependent scattering could be more efficiently utilized in the CCP region. One schematic demonstration of the CCP-CPP-MR device is shown in **Fig. 6-1**. Through exploration of other high-resistive spacer material candidates, higher MR output may be obtained.

In this chapter, we describe our work on the CCP-CPP-MR devices with high-resistive Mg$_{0.2}$Ti$_{0.8}$O (short as MTO in this chapter) as the semiconducting material. Since the metallic layers sandwiching the high-resistive material are the key to obtain the CCP region, we use the Ag layer as the metallic sandwiching layer due to its low resistivity and weak spin-orbit coupling.
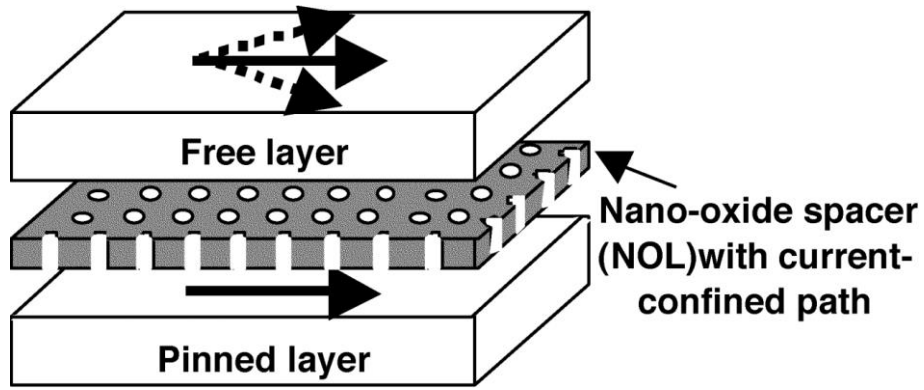
Fig. 6-1 Schematic demonstration of a CCP-CPP-MR device. Electrical current is confined inside the metallic region of the nano-oxide spacer. From Ref. [51]

6.2   Magneto-transport properties at room temperature

Fig. 6-2 (a) shows the MR ratio-R_PA plot of CPP-MR devices with stacking structure of Cr(10)/Ag(100)/CFGG(10)/Ag(t_{Ag})/MTO(2)/Ag(t_{Ag})/CFGG(10)/Ag(5)/Ru(8) (thickness in nm, t_{Ag} =0 or 1 nm) deposited on (001)MgO single-crystalline substrate. The top CFGG electrode was *in-situ* annealed inside the sputtering chamber at 550°C for 10 min (all the thin films hereafter are heat-treated the same way otherwise noted). Initially, a dc current of 0.1 mA was applied to the CPP-MR devices. As a result, the devices without Ag insertion show almost no MR ratio (< 1%), while for devices with 1 nm Ag insertion the MR ratio dramatically increases up to 10%. For devices with 1 nm Ag insertion, the resistance-area product of the parallel magnetization state (R_PA, note that A refers to the physical cross-section area of the device, while actual cross-sectional area through which the current flows is smaller) is between 120-160 mΩ μm^2, which is 4 to 5 times higher than the R_PA of CPP-GMR PSVs with Ag spacer layer (**Fig. 6-2** (b)). By gradually increasing the current amplitude from ($\pm$) 0.1 mA to 6 mA, the V_b dependence of device resistance was obtained. However, from the V_b dependence of the normalized device resistance (**Fig. 6-2** (c)), we observed a decrease in the R_PA when the applied V_b increases, specifically, from 0 mV to 40 mV. Generally, for CPP-GMR devices the R_PA usually increases with increasing applied V_b due to the enhancement of background thermal resistance due to increased Joule heating. The abnormal R_PA behavior here suggests that the underlying transport mechanism is electron tunneling rather than spin-dependent scattering which is the origin for the CPP-GMR devices. Note that a relatively good fabrication yield is observed for this MTO thickness of 2 nm. For most of the devices fabricated on one substrate, the MR ratio ranges from 6.7-10.0% with device resistance varying from 6-8 Ω. This is a favorable feature for practical sensor fabrication. The results above suggest that the insertion of the Ag nano-layer has positive effect on the MR property enhancement, therefore we focus on the 1 nm Ag inserted CPP-MR devices regarding the magneto-transport properties hereafter.
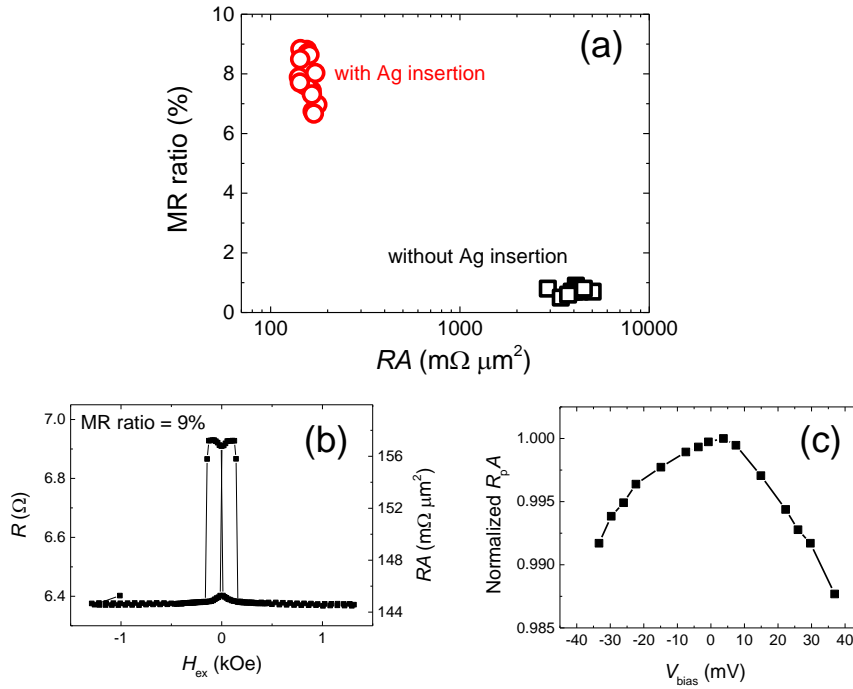
Fig. 6-2 (a) MR ratio- $R_P A$ plot of CPP-MR devices with stacking structure of Cr(10)/Ag(100)/CFGG(10)/Ag(t_{Ag})/MTO(2)/Ag(t_{Ag})/CFGG(10)/Ag(5)/Ru(8) (thickness in nm, t_{Ag} =0 or 1 nm) deposited on (001)MgO single-crystalline substrate. After the top CFGG was deposited, the multilayer stacks were annealed at 550ºC for 10 min. Typical R-H curve and V_b dependence of normalized $R_P A$ for the Ag-inserted devices are shown in (b) and (c).

Further, we investigated the MTO thickness (t_{MTO}) dependence of MR ratio and $R_P A$ as shown in **Fig. 6-3** (a) and (b) with small current amplitude (0.1 mA). When t_{MTO} increases from 2 nm to 2.2 nm, the average MR ratio increases, however, its data scattering increases as well; when t_{MTO} further increases from 2.2 to 2.4 nm, the average MR ratio decreases accompanied by a decrease in data scattering. As for the $R_P A$, large data scattering starts to appear when t_{MTO} is more than 2.1 nm. From these data, we conclude that the MR properties of such Ag/MTO/Ag spacer system are highly sensitive to the t_{MTO}. For the optimized t_{MTO} of 2.2 nm, the MR ratio-$R_P A$ plot is shown in **Fig. 6-3** (c), most of the MR data points are within the range of 150-300 mΩ μm^2, the best device shows a remarkable MR ratio of 45.7% with the $R_P A$ of 207 mΩ μm^2.
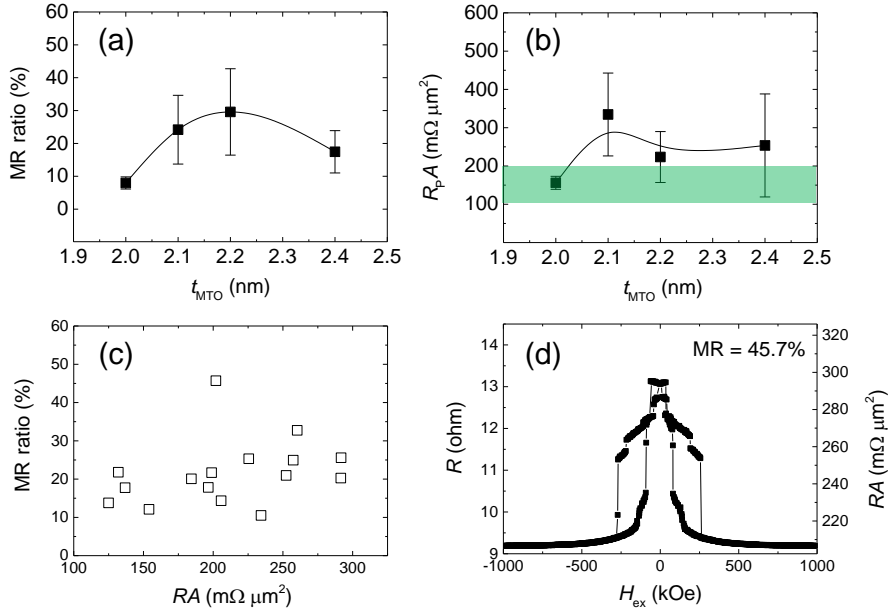
Fig. 6-3 (a) MR ratio and (b) R_PA as a function of MTO thickness. (c) MR ratio-R_PA plot for devices with optimized MTO thickness of 2.2 nm. (d) *R-H* curve of the best individual device. Note that dc current of 0.1 mA is applied for all the transport measurement here.

Fig. 6-4 shows the electrical current amplitude dependence of *R-H* curves of individual device with t_{MTO} = 2.2 nm showing one of the best MR properties. With increasing current amplitude, the MR ratio dramatically decreases from 41.8% down to 23.8% due to the occurrence of predominant spin transfer torque that destabilizes the antiparallel magnetizations. Specifically, at large current densities (e.g. $>10^7$ A/cm^2), the magnetization or magnetic domain of the CFGG layers changes its direction when the spin angular momentum of electrons is partially transferred to the magnetization or magnetic domain, thus their direction is likely to deviate from the CFGG easy axis to achieve a metastable magnetization state.
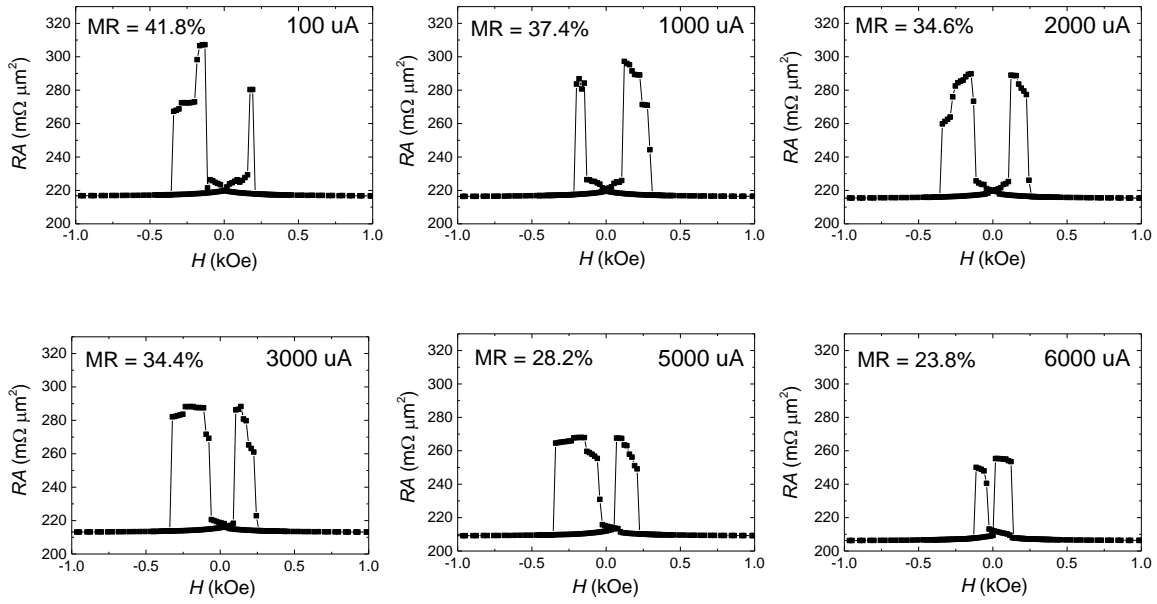
Fig. 6-4 Electrical current amplitude dependence of *R-H* curves of individual device that exhibits large MR ratio.

Finally, we plot the V_b dependence of device output voltage ΔV with t_{MTO} ranging from 2-2.4 nm as shown in **Fig. 6-5**. The ΔV_{max} increases when t_{MTO} increases from 2 to 2.2 nm and decrease from 2.2 nm to 2.4 nm. With t_{MTO} of 2.2 nm, a large ΔV_{max} of 16.2 mV was obtained under the bias voltage of 60-70 mV. Such large ΔV_{max} is more than 40% higher than the CPP-MR devices with In-Zn-O spacer material and is more than 3 times higher than the best ΔV_{max} value of all-metallic CPP-GMR devices. The current density estimated here is more than 3×10^7 A/cm^2 using the physical area of the device, thus the actual current density is even higher because the area *A* is overestimated due to the occurrence of CCP phenomenon. Note that such device shows same tendency for the V_b dependence of $R_P A$ as mentioned earlier, suggesting that the transport mechanism is again tunneling rather than spin-dependent scattering. The exceptionally large voltage output of CPP-MR devices with high resistive MTO spacer layer makes it promising as a potential spacer material candidate for future HDD read sensors.
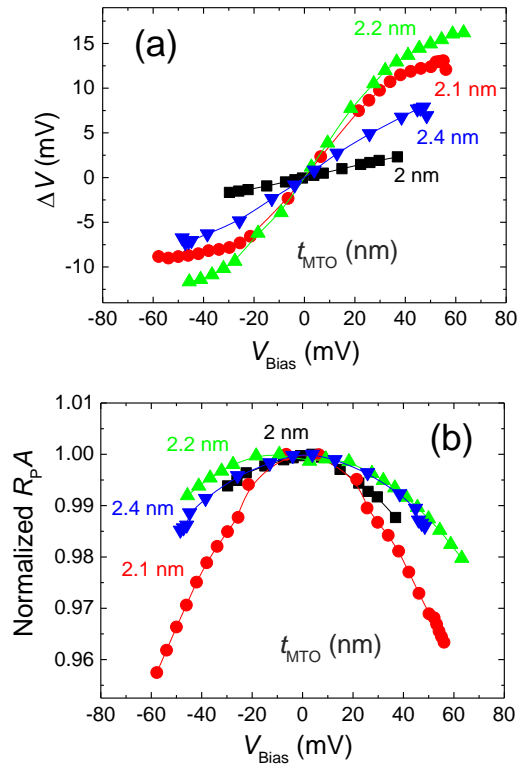
84

Fig. 6-5 Bias voltage dependence of (a) device output voltage ΔV and (b) $R_P A$.

6.3 Microstructure

Fig. 6-6 shows the HAADF-STEM images and EDS elemental mappings of micro-patterned CPP-MR devices with 2.2 nm MTO spacer layer with 1 nm Ag insertion. As for the MTO single layer, each element of Mg, Ti and O remains in the spacer region, with no drastic interlayer diffusion found. However, it is difficult to determine whether Mg, Ti or O is homogeneous or not, especially for the Mg atoms, whose atomic content is the lowest amongst Mg, Ti and O. On the other hand, the upper 1 nm Ag insertion layer completely disappears, while the lower Ag insertion layer remains where it was deposited. This suggests that the upper Ag insertion layer encountered interlayer diffusion during annealing. For the Ag elemental mapping super-imposed with HAADF-STEM image, the inter-diffusion is more pronouncedly observed.
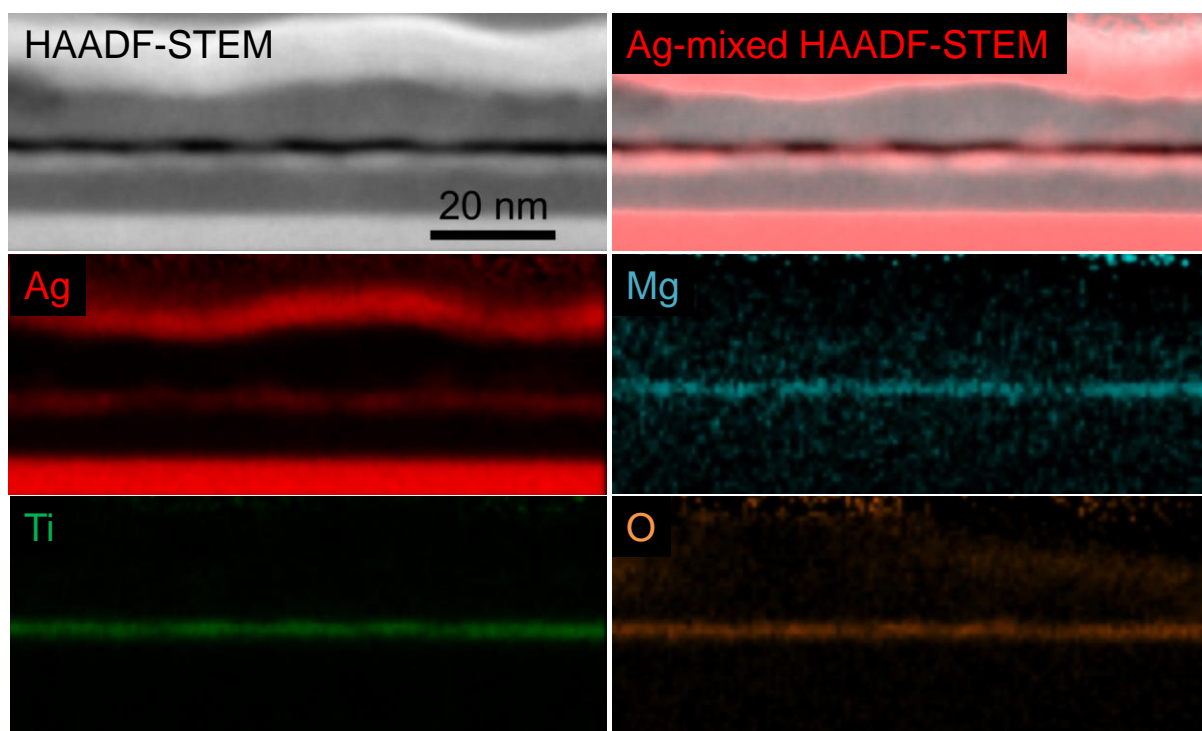
Fig. 6-6 HAADF-STEM images and EDS mapping of micro-patterned CPP-MR device with 2.2 nm MTO spacer layer with 1 nm Ag insertion.

Fig. 6-7 shows the high-resolution TEM images of two individual devices and their corresponding nano-beam diffraction patterns. It is apparent to see that for both cases, the bottom CFGG layer remains epitaxial, while the top CFGG layer shows random crystallographic orientation. The reason for the polycrystalline behavior of the upper CFGG is the amorphous MTO layer upon which it grows. Note that in the MTO region, some symmetric diffraction spots can be seen despite its amorphous nature.
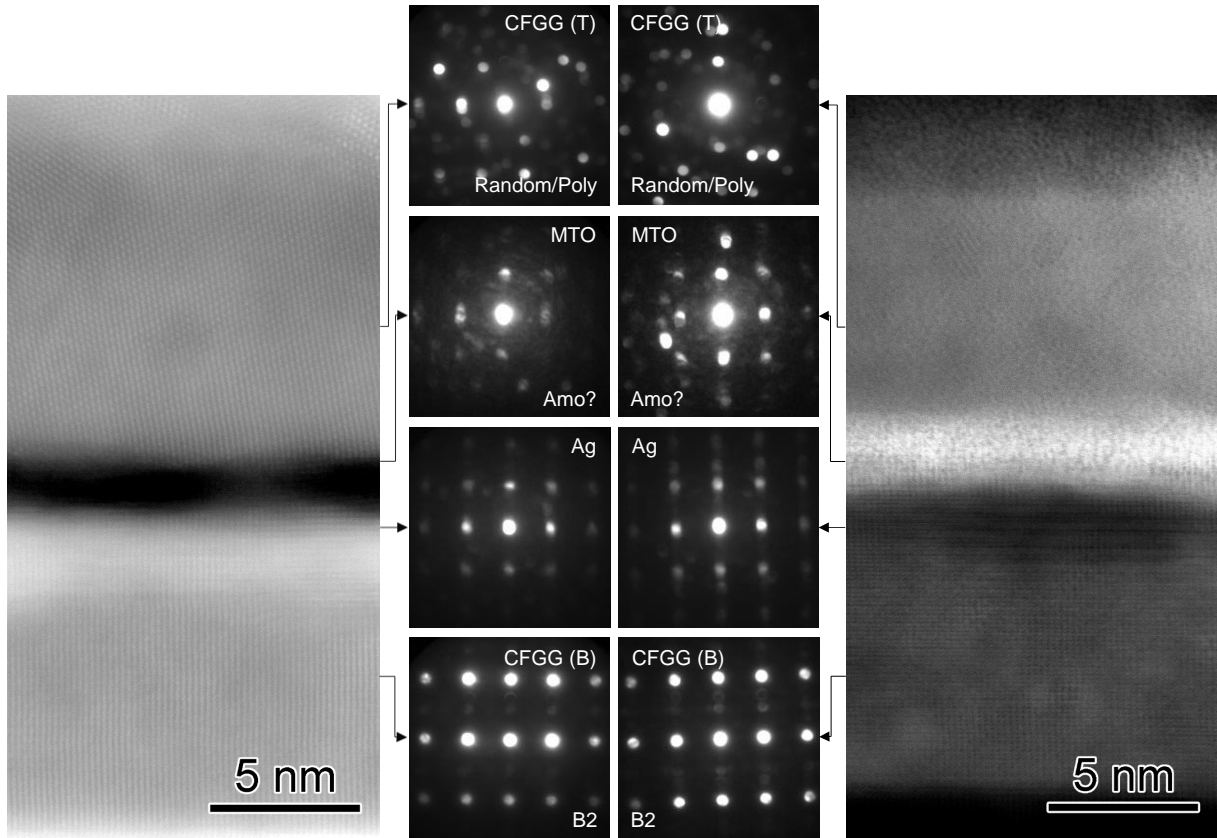
Fig. 6-7 High-resolution TEM of micro-patterned CPP-MR device with 2.2 nm MTO spacer layer with 1 nm Ag insertion.

Fig. 6-8 (a) shows the HAADF-STEM image of the device mentioned above, the black layer is the MTO layer, and the thin white layer beneath it is the Ag insertion layer. For the MTO layer, some blurred regions are observed. **Fig. 6-8** (b), (c) are the magnified high-resolution image and the Ag elemental mapping. From **Fig. 6-8** it is confirmed that some Ag atoms penetrate the MTO layer and remain in the spacer region, forming metallic conduction path, thus the CPP-MR devices mentioned above convincingly show the CCP characteristics, in which the current flows inhomogeneously through the Ag/MTO/Ag multilayer spacer.
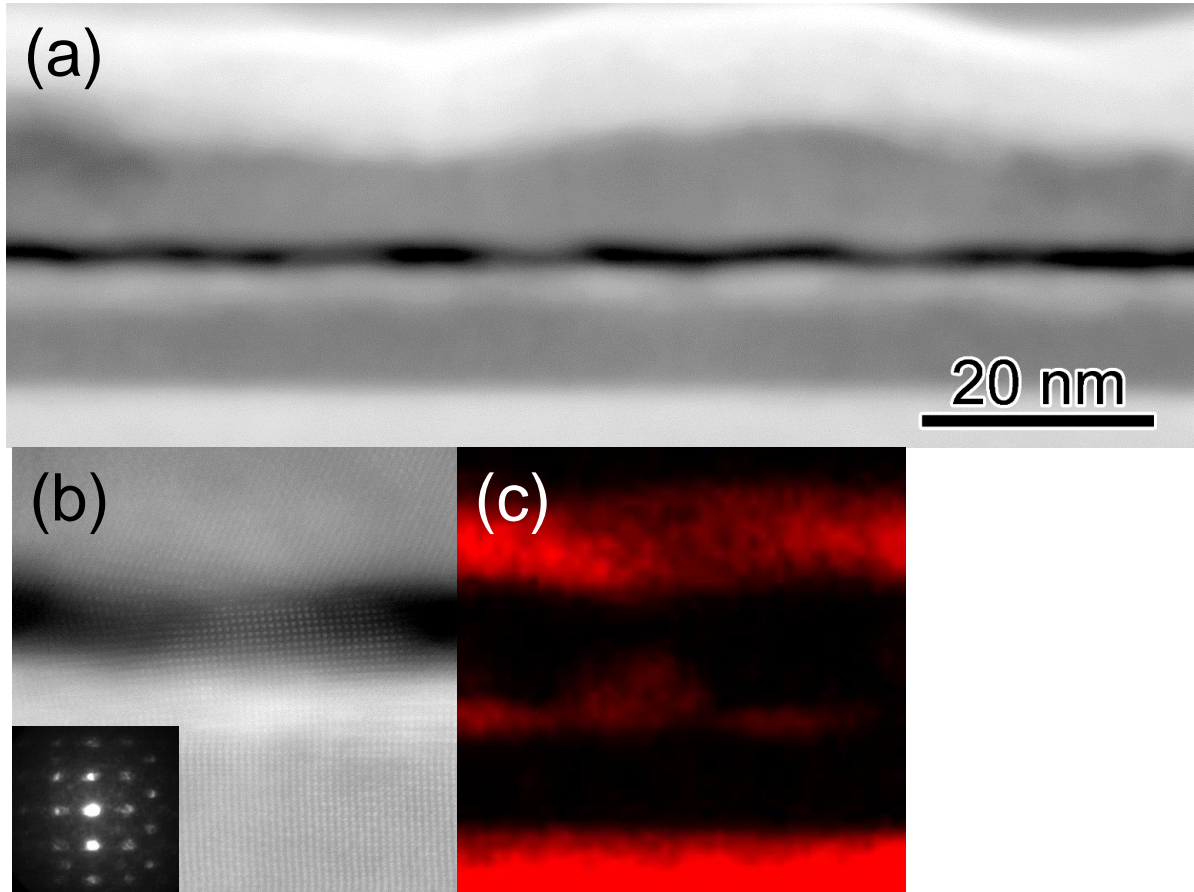
Fig. 6-8 (a) HAADF-STEM images, (b) high-resolution TEM images and (c) Ag mapping of micro-patterned CPP-MR device with 2.2 nm MTO spacer layer with 1 nm Ag insertion.

6.4 Discussion

6.4.1 Bias voltage dependence of output voltage and its temperature dependence

In **Section 6.2** we have shown that there is large data scattering for the MR ratio as well as the device R_PA when t_{MTO} is above 2 nm. Although the microstructure in **Section 6.3** has revealed the occurrence of CCP based microstructure, the transport mechanism of such devices is still unclear and the observed data scattering cannot be explained up to here. Therefore, in order to gain a better understanding of the transport mechanism, we have performed low-temperature measurement for devices with t_{MTO} of 2.4 nm. Specifically, devices with room-temperature R_PA of 174 mΩ μm^2 (8 Ω), 255 mΩ μm^2 (13 Ω), 450 mΩ μm^2 (22 Ω) were systematically measured. The main reason to choose such a thickness is that the largest R_PA scattering is observed for such a t_{MTO}.

For the device with R_PA of 174 mΩ μm^2, the temperature dependence of normalized R_PA is shown in **Fig. 6-9** (a). As a result, the normalized R_PA increases when T decreases from 300 K to 170 K, suggesting a semiconducting or tunneling behavior, while when T decreases further from 170 K to 10 K, the normalized R_PA decreases, suggesting a metallic or ohmic transport behavior. Such transport mechanisms agrees well with the V_b dependence of R_PA or normalized R_PA. At 10 K (**Fig. 6-9** (b)), the R_PA or normalized R_PA increases with increasing V_b; while at 300 K (**Fig. 6-9** (c)), the R_PA or normalized R_PA decreases with increasing V_b, proving that there is a change of major transport mechanism from tunneling to metallic transport when T decreases from 300 K to 10 K.

For the device with R_PA of 255 mΩ μm^2, the temperature dependence of normalized R_PA behaves similarly as shown in **Fig. 6-10**. Note that the downturn temperature decreases from 170 K to 120 K, suggesting that the tunneling transport becomes more prominent in this device compared to the device with R_PA of 174 mΩ μm^2.

As for the device with R_PA of 450 mΩ μm^2, the normalized R_PA increases monotonically when temperature decreases from 300 K to 10 K (**Fig. 6-11** (a)), suggesting tunneling transport behavior throughout the temperature range. The V_b dependence of R_PA agrees accordingly (**Fig. 6-11** (b) and (c)): the R_PA increases with increasing V_b at both 10 K and 300 K.

If we put together the data of devices with R_PA of 174, 255 and 450 mΩ μm^2, we obtain **Fig. 6-12**. **Fig. 6-12** (a) shows clearly an enhanced semiconducting or tunneling component in the magneto-transport when device resistance increases. At 10 K, it is worth to note that for devices with metallic-dominant transport (174, 255 mΩ μm^2), the normalized R_PA increase is somehow similar (**Fig. 6-12** (b)). This may be explained by a similarity in the overall Joule heating for these
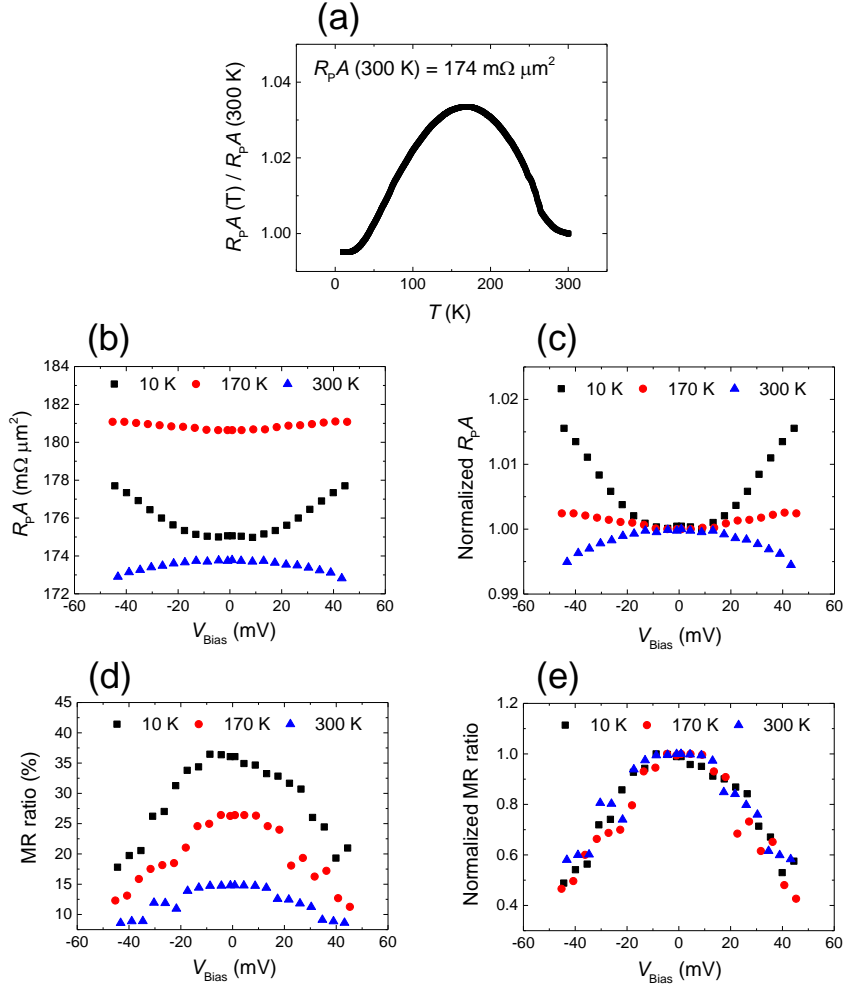
Fig. 6-9 (a) Temperature dependence of normalized R_PA for a 174 mΩ μm^2 device with MTO thickness of 2.4 nm. (b), (c), (d), (e) show the bias voltage dependence of R_PA, normalized R_PA, MR ratio and normalized MR ratio.

two devices. At 300 K, more rapid R_PA decrease is found when device resistance increases (**Fig. 6-12** (c)), suggesting also an increasing tunneling component in the magneto-transport.

In conclusion, the discussion above suggests that for lower resistance device (174, 255 mΩ μm^2), although the dominant transport mechanism is electron tunneling at room temperature, the tunneling transport becomes more prominent when the resistance increases, indicating that there is less Ag current-confined path (either CCP density or CCP area) existing in the devices. For higher R_PA device (450 mΩ μm^2), the transport mechanism stays tunneling independent of the measuring temperature, indicating that the Ag current-confined path is very low in density.
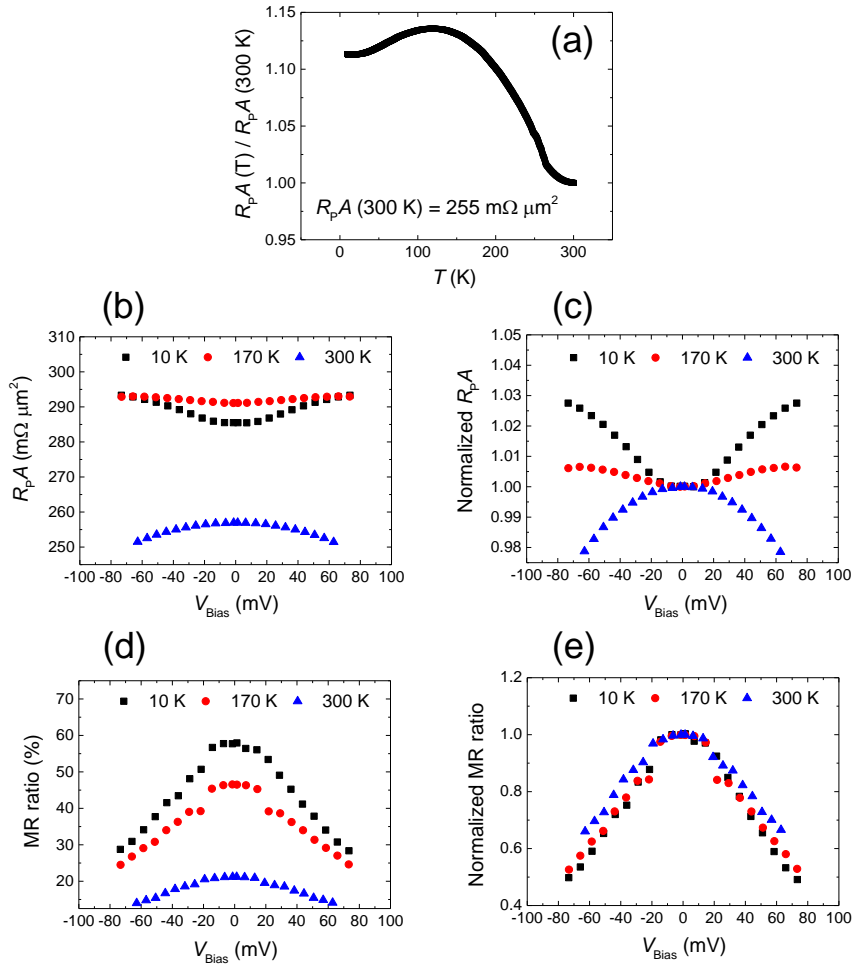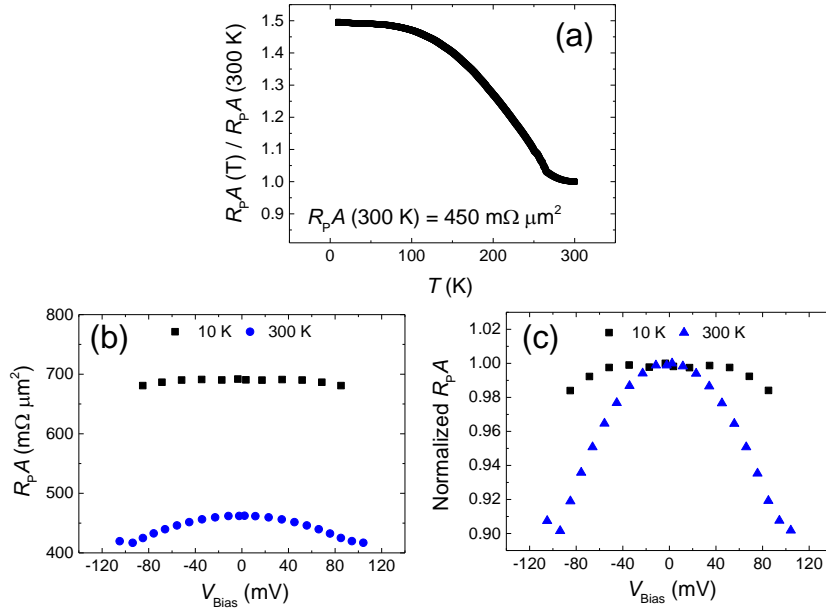
Fig. 6-10 (a) Temperature dependence of normalized R_PA for a 255 mΩ μm^2 device with MTO thickness of 2.4 nm. (b), (c), (d), (e) show the bias voltage dependence of R_PA, normalized R_PA, MR ratio and normalized MR ratio.

Fig. 6-11 (a) Temperature dependence of normalized R_PA for a 450 mΩ μm^2 device with MTO thickness of 2.4 nm. (b), (c) show the bias voltage dependence of R_PA and normalized R_PA.
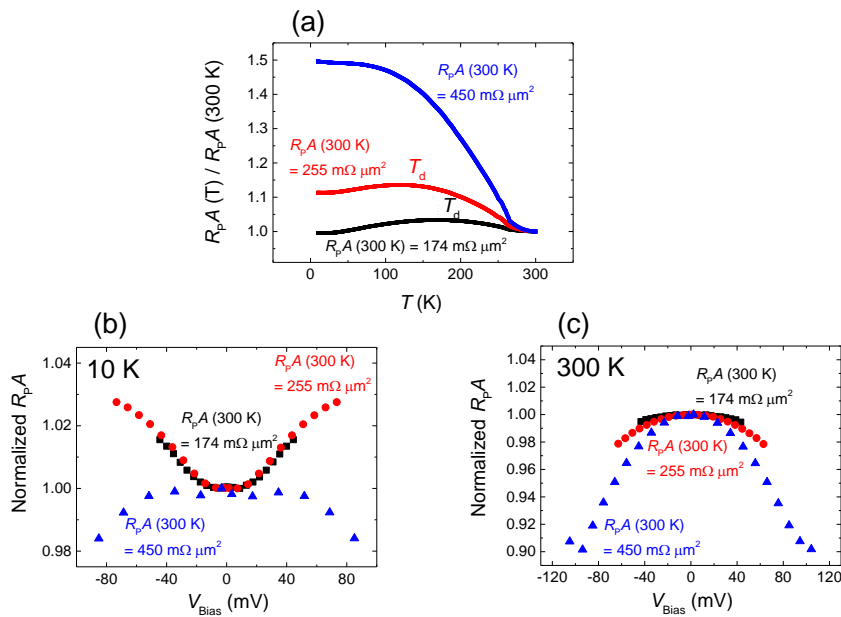

Fig. 6-12 (a) Temperature dependence of normalized R_PA for 174 mΩ μm^2, 255 mΩ μm^2 and 450 mΩ μm^2 devices with MTO thickness of 2.4 nm. (b) and (c) show the bias voltage dependence of normalized R_PA at 10 K and 300 K, respectively.

6.4.2 Temperature dependence of MR output

Fig. 6-13 shows the measuring temperature (T) dependence of (a) MR ratio, (b) normalized MR ratio, (c) ΔRA and (d) normalized ΔRA for devices with $R_P A$ (300 K) of 174 mΩ μm^2, 255 mΩ μm^2 and 450 mΩ μm^2 at MTO thickness of 2.4 nm. The applied current is fixed at 0.1 mA. As a result, the absolute MR values do not have much tendency when T varies. However, if we normalized the MR ratio with respect to the MR value at 300 K, we obtain a stronger temperature dependence of MR ratio when the $R_P A$ increases, *e.g.* the MR ratio decreases more rapidly when T increases from 10 K to 300 K; the tendency of normalized ΔRA turns out to be very similar. Based on the discussion in **6.4.1**, it is suggested that the increase of tunneling in the magneto-transport is accompanied by a stronger temperature dependence of MR output.

Moreover, **Fig. 6-14** shows the measuring temperature (T) dependence of (a) $R_P A$, (b) normalized $R_P A$, (c) $R_{AP} A$ and (d) normalized $R_{AP} A$ for devices mentioned above. It turns out that the increase of ΔRA when T decreases is mainly coming from an increase of $R_{AP} A$. Although the $R_P A$ also increases when T decreases from room temperature to certain temperature, the $R_{AP} A$ increases more rapidly. Overall, due to the co-existence of GMR and TMR effect in all the devices measured at room temperature, the magneto-transport is likely to be highly spin-dependent but difficult to separate easily. Next we will try to use a simplified model to describe this hybrid system.
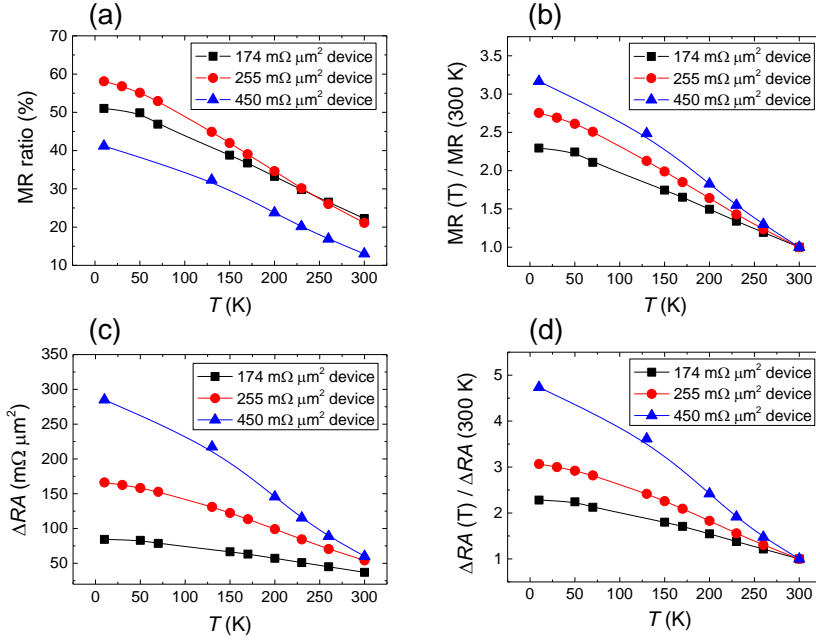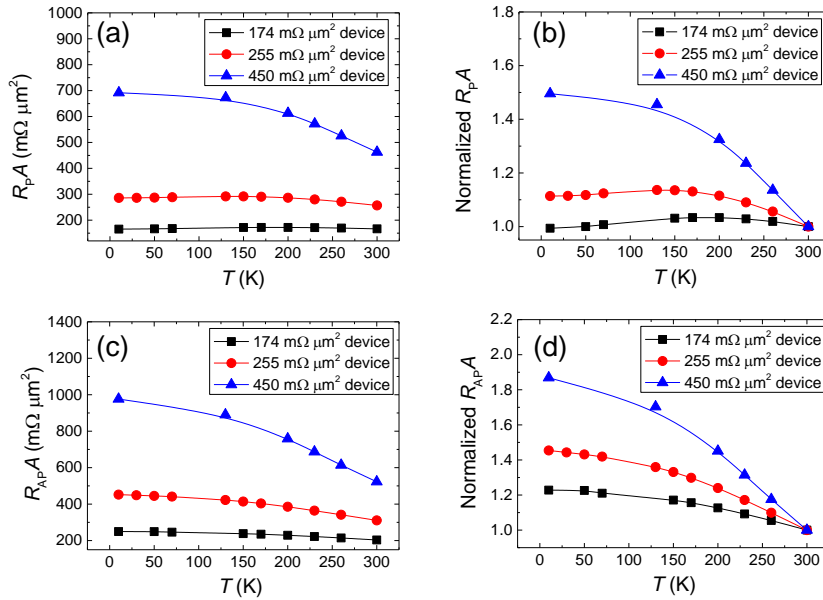
Fig. 6-13 Measuring temperature (T) dependence of (a) MR ratio, (b) normalized MR ratio, (c) ΔRA and (d) normalized ΔRA for devices with $R_P A$ (300 K) of 174 mΩ μm^2, 255 mΩ μm^2 and 450 mΩ μm^2 at MTO thickness of 2.4 nm. The applied current is fixed at 0.1 mA.

Fig. 6-14 Measuring temperature (T) dependence of (a) $R_P A$, (b) normalized $R_P A$, (c) $R_{AP} A$ and (d) normalized $R_{AP} A$ for devices with $R_P A$ (300 K) of 174 mΩ μm^2, 255 mΩ μm^2 and 450 mΩ μm^2 at MTO thickness of 2.4 nm. The applied current is fixed at 0.1 mA.

6.4.3 Model for magneto-transport

We propose a simplified model to explain the temperature dependence of the normalized R_P behavior. Generally, the R_P reflects the resistivity of the whole multilayer thin film stack. Due to the geometry of the current-confined path, the whole multilayer R_P (if we consider the bulk only) can be approximately expressed as:

$$R_P = R_{CFGG} + R_{Ag\_inser} + R_{Spacer} \tag{6.1}$$

R_{CFGG}, and R_{Ag_inser} are the resistance coming from the CFGG layer and Ag insertion layer, which decreases as measuring temperature T decrease due to their metallic nature. R_{Spacer} represents the resistance of the spacer which is basically a parallel connection of MTO spacer and current-confined path, therefore

$$R_{Spacer} = \frac{R_{MTO} \cdot R_{CCP}}{R_{MTO} + R_{CCP}} \tag{6.2}$$

in which the R_{MTO} and R_{CCP} are the overall resistance of the MTO and current-confined path. Specifically, if we assume that the current-confine path is homogeneous through the MTO spacer region.

$$R_{MTO} = \rho_{MTO} \frac{l}{A_{MTO}} \tag{6.3}$$

$$R_{CCP} = \rho_{CCP} \frac{l}{A_{CCP}} \tag{6.4}$$

Therefore,

$$R_{Spacer} = \frac{\frac{\rho_{CCP}}{A_{CCP}} \cdot l}{\frac{\rho_{CCP}}{\rho_{MTO}} \cdot \frac{A_{MTO}}{A_{CCP}} + 1} \tag{6.5}$$

or equally,

$$R_{Spacer} = \frac{\frac{\rho_{MTO}}{A_{MTO}} \cdot l}{\frac{\rho_{MTO}}{\rho_{CCP}} \cdot \frac{A_{CCP}}{A_{MTO}} + 1} \tag{6.6}$$

Generally, the resistance coming from the spacer determines the overall resistance behavior. At higher measuring temperature, $e.g.$ 300 K, due to the fact that all the devices show tunneling behavior, according to (6.6), $\frac{\rho_{MTO}}{\rho_{CCP}} \cdot \frac{A_{CCP}}{A_{MTO}}$ has to be much less than 1, indicating that $\rho_{MTO} \cdot A_{CCP}$ has to be much smaller than $\rho_{CCP} \cdot A_{MTO}$, which means ρ_{CCP} must be comparable to ρ_{MTO}. This might be explained by a possible diffusion of dilute Ag into the non-CCP MTO region. However, it is quite difficult to confirm quantitatively how much Ag is doped into the non-CCP MTO region. At low temperature, e.g. 10 K, with Ag resistivity further decreasing and MTO resistivity increasing, it

is probable that the CCP region is metallic because since part of the Ag atoms penetrate the MTO layer, the low-resistivity Ag will carry most of the current. Due to the fact that $\rho_{CCP} \ll \rho_{MTO}$, according to (6.5), $R_{Spacer} = \frac{\rho_{CCP}}{A_{CCP}} \cdot l$, therefore the device shows ohmic transport, *e.g.* **Fig. 6-9** and **Fig. 6-10**. However, if in the device the current-confined path density is so small that it is even negligible, *e.g.* $A_{CCP} \ll A_{MTO}$, then $\frac{\rho_{MTO}}{\rho_{CCP}} \cdot \frac{A_{CCP}}{A_{MTO}} \ll 1$, $R_{Spacer} = \frac{\rho_{MTO}}{A_{MTO}} \cdot l$, then even at low temperature the device shows tunneling behavior (**Fig. 6-11**).
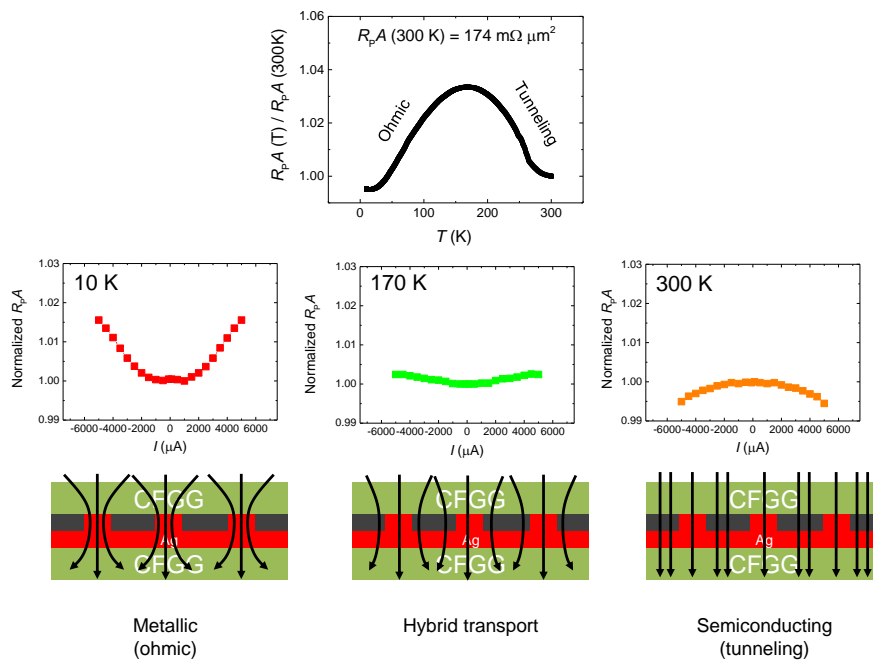
Fig. 6-15 A simplified model explaining the electrical transport of device with $R_P A$ of 174 mΩ μm^2 at different measuring temperatures.

6.5 Summary of the chapter

We have investigated the magneto-transport properties of the CPP-MR devices with $Co_2Fe(Ga_{0.5}Ge_{0.5})$ (CFGG) Heusler alloy and high resistive $Mg_{0.2}Ti_{0.8}O$ (MTO) spacer layer. For all the measured devices at room temperature, the device resistance decreases as the bias voltage (V_b) increases, suggesting that the underlying transport mechanism is tunneling rather than spin-dependent scattering. With 10 nm CFGG and 2.2 nm MTO, the devices show MR ratio ranging from 15% to 46% with a RA ranging from 150 mΩ μm^2 to 250 mΩ μm^2 with a current amplitude of 0.1 mA. For the best device, a large ΔV_{max} of 16.2 mV was obtained as a large V_b of 60 mV, which is > 40% larger than the CPP-MR device with In-Zn-O spacer and more than 3 times higher than the best ΔV_{max} value of all-metallic CPP-GMR devices reported so far. The reason to obtain such remarkable MR properties is due to the utilization of current-confined path in the high resistive spacer region, which enables the competing transport mechanism of ohmic and semiconducting (tunneling). The current CPP-MR result with the MTO spacer shows explicitly an advantage in view of output voltage compared to the all-metallic CPP-GMR devices, suggesting that high resistive materials hold potential to replace the MgO barrier used in current read sensors for future HDD magnetic recording.

Chapter 7   Summary of the thesis

This doctoral thesis has described the utilization of highly spin polarized Heusler alloy $Co_2Fe(Ga_{0.5}Ge_{0.5})$ and various spacer materials for CPP-MR devices which hold potential to be used for future ultrahigh density HDD read sensors. The objective of the thesis is 1) to obtain large MR output in the CPP-GMR sensors, 2) to investigate the crystal orientation dependence of MR output in CPP-GMR sensor, 3) to obtain large voltage output in CPP-MR devices with high resistive spacer layer and study the spin torque suppression in those CPP-MR sensors. The result summary is as follows:

1) Fully epitaxial CPP-PSV devices using CFGG Heusler alloy as FM layers and AgZn alloy as a spacer have been prepared. Large MR ratio of 59.6% (ΔRA = 21.5 mΩ μm^2) was obtained at 300 K for the CPP-PSV annealed at 630°C using 10 nm CFGG layer and 5 nm AgZn spacer layer. At 10 K, the MR ratio increases to 200.0% (ΔRA = 59.8 mΩ μm^2). HAADF-STEM images and EDS mappings revealed that Zn has almost completely diffused out from the CPP-PSV device after annealing at T_{an} = 630°C, thereby enhancing $L2_1$ ordering in CFGG. The high degree of $L2_1$ order of CFGG is considered to result in high spin polarization of CFGG. The method for enhancing $L2_1$ ordering and high spin polarization of Heusler alloy by utilizing the diffusion of Zn would be useful not only for CPP-GMR but also for other spintronic applications. The PSV shows relatively large ΔRA of 10.9 mΩ μm^2 with the MR ratio of 25.6% for the low annealing temperature of 350°C, which is a practically useful feature for read sensor applications.

2) Polycrystalline PSV devices with MgO-induced multilayer <001> texture on thermally oxidized Si substrates using CFGG ferromagnetic layers and a Ag spacer were fabricated. The optimally annealed <001> textured PSV exhibited ΔRA of ~ 6 mΩ μm^2 and MR ratio of 16%, which was one of the highest MR output among polycrystalline CPP PSVs or SVs reported. The PSV with the <001> textured CFGG films outperforms the one with the <011> texture, possibly because of the reduction in lattice mismatch at the CFGG/Ag interface. The work has also shown the possibility of orientation dependence of the interfacial spin scattering asymmetry γ in CPP-GMR. However, no clear orientation dependence of γ was observed for the region of T_{an} < 350°C, which we speculate is due to the low chemical ordering of CFGG layer.

On the other hand, in consideration of practical limitations, MgO as an insulator cannot be used for the fabrication of actual CPP-GMR sensors which must be grown on conductive buffer layers. Therefore, we investigated the CPP-GMR properties and microstructure of PSV devices with

<001> textured FM Heusler layer CFGG and conductive buffer layer MTO. By using the multilayer of a-NiTa(10)/MTO(2)/Cr(10)/CoFe(2) as the underlayer beneath CFGG we obtained observable B2 ordering of the Heusler electrode. PSVs with 10 nm CFGG and 2 nm MTO layers demonstrate average ΔRA of 6.4 mΩ μm^2 with Ag as the spacer layer. HAADF-STEM and EDS results revealed interfacial smoothness up to the top CFGG layer. Relatively large MR output and desirable interfacial smoothness make MTO a promising choice to fabricate <001> textured Heusler alloy based CPP-GMR devices.

3) CPP-GMR devices with the combination of FM Heusler layer CFGG and NM Heusler spacer Cu-Cr-Al (CCA) were investigated. At 300°C, the CCA thin film with Cr-lean composition of $Cu_2Cr_{0.72}Al_{1.05}$ shows L2$_1$ ordering and the corresponding CPP-GMR device shows maximum MR output; further increasing the T_{an} to 350°C results in reduction of MR ratio due to possible phase separation of Al. We were to expected that the combination of highly spin polarized CFGG layer and L2$_1$ ordered CCA would lead to an increase in the spin dependent interfacial scattering asymmetry at the FM/NM interface. However, the poor thermal tolerance of the CCA spacer severely limits the CPP-GMR output. On the other hand, increasing the Cr concentration in $Cu_2Cr_{0.72}Al$ decreased CPP-GMR, which is possibly caused by the occurrence of higher degree of s-d scattering between the conduction electrons and magnetic moment of isolated Cr atoms. These results suggest that a spacer material containing magnetic element/magnetic moment may not be suitable for the enhancement of CPP-GMR output.

4) The magneto-transport properties of the CPP-MR devices with $Co_2Fe(Ga_{0.5}Ge_{0.5})$ (CFGG) Heusler alloy and high resistive $Mg_{0.2}Ti_{0.8}O$ (MTO) spacer layer have been investigated. For all the measured devices at room temperature, the device resistance decreases as the bias voltage (V_b) increases, suggesting that the underlying transport mechanism is tunneling rather than spin-dependent scattering. With 10 nm CFGG and 2.2 nm MTO, the devices show MR ratio ranging from 15% to 46% with a RA ranging from 150 mΩ μm^2 to 250 mΩ μm^2 with a current amplitude of 0.1 mA. For the best device, a large ΔV_{max} of 16.2 mV was obtained as a large V_b of 60 mV, which is > 40% larger than the CPP-MR device with In-Zn-O spacer and more than 3 times higher than the best ΔV_{max} value of all-metallic CPP-GMR devices reported so far. The reason to obtain such remarkable MR properties is due to the utilization of current-confined path in the high resistive spacer region, which enables the competing transport mechanism of ohmic and semiconducting (tunneling). The current CPP-MR result with the MTO spacer shows explicitly an advantage in view of output voltage compared to the all-metallic CPP-GMR devices, suggesting that high

resistive materials hold potential to replace the MgO barrier used in current read sensors for future HDD magnetic recording.

Publications

- **<u>Ye Du</u>**, T. Furubayashi, T. T. Sasaki, Y. Sakuraba, Y. K. Takahashi, and K. Hono
Large magnetoresistance in current-perpendicular-to-plane pseudo spin-valves using $Co_2Fe(Ga_{0.5}Ge_{0.5})$ Heusler alloy and AgZn spacer
Appl. Phys. Lett. 107, 112405 (2015)

- **<u>Ye Du</u>**, B. S. D. Ch. S. Varaprasad, Y. K. Takahashi, T. Furubayashi, and K. Hono
<001> textured polycrystalline current-perpendicular-to-plane pseudo spin-valves using $Co_2Fe(Ga_{0.5}Ge_{0.5})$ Heusler alloy
Appl. Phys. Lett. 103, 202401 (2013)

- **<u>Ye Du</u>**, T. M. Nakatani, Y. K. Takahashi, N. Hase, T. Furubayashi, and K. Hono
Polycrystalline current-perpendicular-to-plane giant magnetoresistance pseudo spin-valves using $Co_2Mn(Ga_{0.25}Ge_{0.75})$ Heusler alloy
J. Appl. Phys. 114, 053910 (2013)

- **<u>Ye Du</u>**, T. Furubayashi, Y. K. Takahashi, Y. Sakuraba, and K. Hono
Polycrystalline CPP-GMR pseudo spin valves using <001> textured $Co_2Fe(Ga_{0.5}Ge_{0.5})$ layer grown on a conductive $(Mg_{0.5}Ti_{0.5})O$ buffer layer
IEEE Trans. Magn. 51, 4401204 (2015)

- T. M. Nakatani, **<u>Ye Du</u>**, Y. K. Takahashi, T. Furubayashi, and K. Hono
Structure and magnetoresistive properties of current-perpendicular-to-plane pseudo-spin valves using polycrystalline Co_2Fe-based Heusler alloy films
Acta Mater. 61, 3695 (2013)

- T. Furubayashi, **<u>Ye Du</u>**, and K. Hono
Comment on "Current perpendicular to film plane type giant magnetoresistance effect using a Ag-Mg spacer and $Co_2Fe_{0.4}Mn_{0.6}Si$ Heusler alloy electrodes" [Appl. Phys. Express 8, 063008 (2015)]
Appl. Phys. Express 8, 119101 (2015)

International presentations

- **Ye Du**, T. Furubayashi, T. Sasaki, Y. Sakuraba, Y. K. Takahashi, and K. Hono
CPP-GMR devices using $Co_2Fe(Ga_{0.5}Ge_{0.5})$ full Heusler alloy and a AgZn alloy spacer
CG-15 (oral), 13th Joint MMM-Intermag Conference, Jan. 11-15, 2016, San Diego, USA

- **Ye Du**, T. Furubayashi, Y. K. Takahashi, Y. Sakuraba and K. Hono
Polycrystalline CPP-GMR devices using <001> textured $Co_2Fe(Ga_{0.5}Ge_{0.5})$ Heusler alloy layer and conductive $Mg_{0.5}Ti_{0.5}O_x$ buffer layer
FF-11 (oral), IEEE International Magnetics Conference, May 11-15, 2015, Beijing, CHINA

- **Ye Du**, B. Varaprasad, T. Furubayashi, Y. K. Takahashi, Y. Sakuraba and K. Hono
<001> textured polycrystalline current-perpendicular-to-plane pseudo spin-valves using full Heusler alloy $Co_2Fe(Ga_{0.5}Ge_{0.5})$
AP-14 (poster), 58th Annual Conference on Magnetism and Magnetic Materials, Nov. 4-8, 2013, Denver, USA

- **Ye Du**, T. M. Nakatani, N. Hase, Y. K. Takahashi, T. Furubayashi, K. Hono
Microstructure and magneto-transport properties of CPP-GMR pseudo spin-valves with polycrystalline Heusler alloy $Co_2Mn(Ga_{0.25}Ge_{0.75})$
FB-05 (oral), 12th Joint MMM-Intermag Conference, Jan. 14-18, 2013, Chicago, USA

Acknowledgement

References

[1] M.N. Baibich, J.M. Broto, A. Fert, F. Nguyen Van Dau, and F. Petroff, Phys. Rev. Lett. **61**, 2472 (1988).

[2] G. Binasch, P. Grünberg, F. Saurenbach, and W. Zinn, Phys. Rev. B **39**, 4828 (1989).

[3] S.A. Wolf, Science **294**, 1488 (2001).

[4] C. Chappert, A. Fert, and F. Nguyen Van Dau, Nat. Mater. **6**, 813 (2007).

[5] B. Dieny, V.S. Speriosu, S.S. Parkin, B.A. Gurney, D.R. Wilhoit, and D. Mauri, Phys. Rev. B **43**, 1297 (1991).

[6] M. Takagishi, K. Koi, M. Yoshikawa, T. Funayama, H. Iwasaki, and M. Sahashi, IEEE Trans. Magn. **38**, 2277 (2002).

[7] S.S.P. Parkin, R. Bhadra, and K.P. Roche, Phys. Rev. Lett. **66**, 2152 (1991).

[8] J.Q. Xiao, J.S. Jiang, and C.L. Chien, Phys. Rev. Lett. **68**, 3749 (1992).

[9] W.P. Pratt Jr, S.-F. Lee, J.M. Slaughter, R. Loloee, P.A. Schroeder, and J. Bass, Phys. Rev. Lett. **66**, 3060 (1991).

[10] M. Gijs, S. Lenczowski, and J. Giesbers, Phys. Rev. Lett. **70**, 3343 (1993).

[11] T. Valet and A. Fert, Phys. Rev. B **48**, 7099 (1993).

[12] N. Mott, Adv. Phys. **13**, 325 (1964).

[13] S.S.P. Parkin, Phys. Rev. Lett. **71**, 1641 (1993).

[14] M. Takagishi, K. Yamada, H. Iwasaki, H.N. Fuke, and S. Hashimoto, IEEE Trans. Magn. **46**, 2086 (2010).

[15] D.D. Djayaprawira, K. Tsunekawa, M. Nagai, H. Maehara, S. Yamagata, N. Watanabe, S. Yuasa, Y. Suzuki, and K. Ando, Appl. Phys. Lett. **86**, 92502 (2005).

[16] H. Maehara, K. Nishimura, Y. Nagamine, K. Tsunekawa, T. Seki, H. Kubota, A. Fukushima, K. Yakushiji, K. Ando, and S. Yuasa, Appl. Phys. Express **4**, 33002 (2011).

[17] T. Kitada, K. Nakamura, Y. Tanaka, S. Furukawa, and T. Hatano, 59th MMM Conf. **DE-02**, (2014).

[18] J.R. Childress, M.J. Carey, S. Maat, N. Smith, R.E. Fontana, D. Druist, K. Carey, J.A. Katine, N. Robertson, T.D. Boone, M. Alex, J. Moore, and C.H. Tsang, IEEE Trans. Magn. **44**, 90 (2008).

[19] J.-G. Zhu, N. Kim, Y. Zhou, Y. Zheng, J. Chang, K. Ju, X. Zhu, and R.M. White, IEEE Trans. Magn. **40**, 2323 (2004).

[20] S. Kiselev, J. Sankey, I. Krivorotov, N. Emley, R. Schoelkopf, R. Buhrman, and D. Ralph, Nature **425**, 380 (2003).

[21] J.-G. Zhu, X. Zhu, and Y. Tang, IEEE Trans. Magn. **44**, 125 (2008).

[22] R.A. De Groot, F.M. Mueller, P.G. Van Engen, and K.H.J. Buschow, Phys. Rev. Lett. **50**, 2024 (1983).

[23] P. Webster, J. Phys. Chem. Solids **32**, 1221 (1971).

[24] B.S.D.C.S. Varaprasad, A. Srinivasan, Y.K. Takahashi, M. Hayashi, A. Rajanikanth, and K. Hono, Acta Mater. **60**, 6257 (2012).

[25] H. Kijima, T. Ishikawa, T. Marukame, H. Koyama, K. Matsuda, T. Uemura, and M. Yamamoto, IEEE Trans. Magn. **42**, 2688 (2006).

[26] S. Picozzi, A. Continenza, and A.J. Freeman, Phys. Rev. B **66**, (2002).

[27] I. Galanakis, P.H. Dederichs, and N. Papanikolaou, Phys. Rev. B **66**, (2002).

[28] Y.K. Takahashi, A. Srinivasan, B. Varaprasad, A. Rajanikanth, N. Hase, T.M. Nakatani, S. Kasai, T. Furubayashi, and K. Hono, Appl. Phys. Lett. **98**, 152501 (2011).

[29] S. Li, Y.K. Takahashi, T. Furubayashi, and K. Hono, Appl. Phys. Lett. **103**, 42405 (2013).

[30] Y. Sakuraba, M. Ueda, Y. Miura, K. Sato, S. Bosu, K. Saito, M. Shirai, T.J. Konno, and K. Takanashi, Appl. Phys. Lett. **101**, 252408 (2012).

[31] J. Sato, M. Oogane, H. Naganuma, and Y. Ando, Appl. Phys. Express **4**, 113005 (2011).

[32] B. Balke, G.H. Fecher, H.C. Kandpal, C. Felser, K. Kobayashi, E. Ikenaga, J.-J. Kim, and S. Ueda, Phys. Rev. B **74**, (2006).

[33] K. Nikolaev, P. Kolbo, T. Pokhil, X. Peng, Y. Chen, T. Ambrose, and O. Mryasov, Appl. Phys. Lett. **94**, 222501 (2009).

[34] N. Hase, T.M. Nakatani, S. Kasai, Y.K. Takahashi, T. Furubayashi, and K. Hono, J. Magn. Magn. Mater. **324**, 440 (2012).

[35] T. Furubayashi, Y.K. Takahashi, T.T. Sasaki, and K. Hono, J. Appl. Phys. **118**, 163901 (2015).

[36] T. Minemura, H. Andoh, and Y. Maeda, J. Appl. Phys. **63**, 4632 (1988).

[37] H. Narisawa, T. Kubota, and K. Takanashi, Appl. Phys. Express **8**, 63008 (2015).

[38] Z. Diao, M. Chapline, Y. Zheng, C. Kaiser, A. Ghosh Roy, C.J. Chien, C. Shang, Y. Ding, C. Yang, D. Mauri, Q. Leng, M. Pakala, M. Oogane, and Y. Ando, J. Magn. Magn. Mater. **356**, 73 (2014).

[39] H. Takagi, K. Kikuchi, R. Maeda, T.R. Chung, and T. Suga, Appl. Phys. Lett. **68**, 2222 (1996).

[40] M.J. Carey, S. Maat, S. Chandrashekariaih, J.A. Katine, W. Chen, B. York, and J.R. Childress, J. Appl. Phys. **109**, 93912 (2011).

[41] T.M. Nakatani, Y. Du, Y.K. Takahashi, T. Furubayashi, and K. Hono, Acta Mater. **61**, 3695 (2013).

[42] Y. Du, T.M. Nakatani, Y.K. Takahashi, N. Hase, T. Furubayashi, and K. Hono, J. Appl. Phys. **114**, 53910 (2013).

[43] W. Wang, H. Sukegawa, R. Shan, and K. Inomata, Appl. Phys. Lett. **93**, 182504 (2008).

[44] H.S. Goripati, T. Furubayashi, Y.K. Takahashi, and K. Hono, J. Appl. Phys. **113**, 43901 (2013).

[45] B.S.D.C.S. Varaprasad, Y.K. Takahashi, A. Ajan, and K. Hono, J. Appl. Phys. **113**, 203907 (2013).

[46] Y. Du, B.S.D.C.S. Varaprasad, Y.K. Takahashi, T. Furubayashi, and K. Hono, Appl. Phys. Lett. **103**, 202401 (2013).

[47] J. Chen, S. Li, T. Furubayashi, Y.K. Takahashi, and K. Hono, J. Appl. Phys. **115**, 233905 (2014).

[48] E.A. Brinkman, M.J. Carey, J.R. Childress, Y.-S. Choi, and B.R. York, US8611053 B2 (17 December 2013).

[49] V. Ko, G. Han, J. Qiu, and Y.P. Feng, Appl. Phys. Lett. **95**, 202502 (2009).

[50] T. Nakatani, G. Mihajlović, J.C. Read, Y. Choi, and J.R. Childress, Appl. Phys. Express **8**, 93003 (2015).

[51] H. Fukuzawa, H. Yuasa, S. Hashimoto, K. Koi, H. Iwasaki, M. Takagishi, Y. Tanaka, and M. Sahashi, IEEE Trans. Magn. **40**, 2236 (2004).